INVESTIGATION INTO ALL-SOLID-STATE, PULSED VIBRONIC LASERS AND THEIR PUMP SOURCES.

Garry R. Morrison

A Thesis Submitted for the Degree of PhD
at the
University of St Andrews

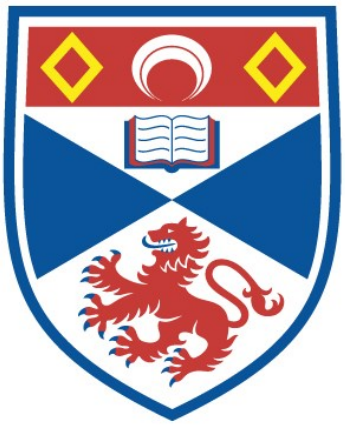

1996

Investigation into all-solid-state, pulsed vibronic lasers and their pump sources

Garry R Morrison

J.F. Allen Physics Research Laboratories,
School of Physics and Astronomy,
University of St. Andrews,
Fife, Scotland

A thesis submitted to the University of St. Andrews in application for the degree of Doctor of Philosophy

April 1996

$T_{\sim}$ C18

I, Garry Morrison, Hereby certify that this thesis, which is approximately 46000 words in length, has been written by me, that it is the record of work carried out by me and that it has not been submitted in any previous application for a higher degree.

date 23 MAY 1996 signature of candidate

I was admitted as a research student in February 1993 and as a candidate for the degree of Ph.D. in April 1996; the higher study for which this is a record was carried out in the University of St. Andrews between 1993 and 1996.

date 23 MAY 1996 signature of candidate

I hereby certify that the candidate has fulfilled the conditions of the Resolution and Regulations appropriate for the degree of Ph.D. in the University of St. Andrews and that the candidate is qualified to submit this thesis application for that degree.

date 23 May 1996 signature of supervisor

In submitting this thesis to the University of St. Andrews I understand that I am giving permission for it to be made available in accordance with the regulations of the University Library for the time being in force, subject to any copyright vested in the work not being affected thereby. I also understand that the title and abstract will be published, and that a copy of the work may be made and supplied to any bona fide library or research worker.

date 23 MAY 1996 signature of candidate

Abstract

This thesis is concerned with the design and construction of an all-solid-state, tuneable, pulsed Cr:LiSAF laser and its evolution into an all-solid-state, single-frequency, pulsed Ti:sapphire laser. The initial investigation into the pulsed operation of the vibronic medium Cr:LiSAF led to the development of a novel 1.3μm Nd:YLF pump laser.

The development of this diode-pumped, Q-switched, 1.3μm Nd:YLF laser is described in detail. This included a comparison of the stimulated emission cross-sections of the 1.321μm and 1.313μm lines, which were shown to be equally strong. The frequency-doubling of the 1.321μm laser in LBO and KTP is compared and the performance of LBO is shown to be superior in this situation. The resulting 660.5nm laser was used as the pump source for a gain-switched Cr:LiSAF laser.

The operation of a tuneable, gain-switched Cr:LiSAF laser with line-narrowing is described in detail. Specifically, the factors limiting its suitability as a diode-pumped, tuneable, single-frequency, pulsed laser medium are addressed. This was achieved, in part, by the construction of an equivalent gain-switched Ti:sapphire laser which was pumped by a frequency-doubled 1μm Nd:YLF laser.

The performance of the two gain-switched vibronic lasers is compared when line-narrowed by interferometric means. Ti:sapphire was established as the superior option in this regard and it was developed further, culminating in an all-solid-state, high repetition rate, gain-switched, single-frequency laser. Single-frequency operation was achieved by the technique of injection-seeding the Ti:sapphire resonator with a single-frequency diode laser. The development of this laser, specifically in its high repetition rate form, is considered to be of great interest and potential.

CONTENTS

CHAPTER 1

INTRODUCTION

In recent years a resurgence of interest into solid-state laser media has been prompted by the rapid development of suitable laser diode pump sources, which offer a vast improvement over traditional flashlamp pump sources. More detailed discussions of these developments than sketched out here can be found in the numerous review articles[1,2,3,4].

Laser diode pumping improves system efficiency, lifetime and reliability, as well as reducing cooling requirements and overall size. These improvements result from the inherent reliability and longevity of the laser diodes with respect to their flashlamp counterparts. Also their narrow emission bandwidths overlap well with the absorption regions of many solid-state laser media. This, together with the ease with which the diode output can be manipulated and coupled into solid-state media, means that heat deposition in the rod is greatly reduced thereby increasing overall conversion efficiency and limiting the cooling compared to that required by flashlamp pumped systems. Cooling of the solid-state medium is necessary in flashlamp pumped systems to minimise undesirable thermally induced effects like thermal lensing and induced birefringence. Furthermore, the frequency stability of these laser diode sources and the reduction of thermal effects result in less noise which makes for more stable output with narrower linewidths. The laser diodes themselves are the most efficient way of converting electrical energy into optical energy (≤50%).

Even though laser diodes represent a huge improvement over flashlamps as pumping sources for solid-state lasers, they cannot compete with the solid-state laser itself. The advantages offered by solid-state lasers far outweigh the drop in overall efficiency with respect to direct use of the laser diodes. The spatial properties (beam divergence, astigmatism), and spectral properties (linewidth, frequency stability), of laser diodes is poor, whereas solid-state lasers are characterised by beams of exceptional spatial quality. The output from laser diodes is tuneable with temperature. However, the high currents required for operation induce large

thermal gradients in pulsed operation, which result in a spread in output frequency. Solid state lasers, on the other hand, can be made to yield extremely narrow linewidth output much more stable in frequency[5]. More recently, laser diodes exhibiting very narrow linewidths using the technique of self-injection locking, by means of a tuneable external cavity have become commercially available[6]. The wavelengths available to diode lasers are predominantly in the near infrared, although progress towards visible laser diodes is being made. Solid state lasers on the other hand easily produce output across the spectrum from the infrared into the ultra-violet.

Laser diodes are essentially continuous wave (CW) devices which operate near their facet damage threshold. Thus they are unable to deliver much higher peak powers in pulsed operation, than in CW operation. Solid state lasers, however, may be simultaneously pumped by many laser diodes, enabling emission energies far in excess of any single laser diode to be achieved. Also solid-state media have good energy storage capabilities which enables them to be operated in Q-switched mode with extremely high output power levels.

All of this has lead to the development of highly efficient, reliable, stable, compact all solid-state laser devices. These are variously able to provide laser output of ultra-short duration, extremely high peak powers, pure spectral quality and very good spatial quality all at a wide variety of wavelengths. Initially only a discrete number of wavelengths were available. The high powers from these lasers meant, however, that nonlinear optical processes such as harmonic generation, sum frequency mixing, stimulated Raman scattering and optical parametric oscillation could be accessed to generate high quality coherent radiation covering the entire visible spectrum as well as the infrared and the ultra-violet.

With the advent of tuneable vibronic solid-state media like Ti:sapphire and Alexandrite[7,8], the possibility of widely tuneable high quality all-solid-state laser sources arose. Vibronic lasers are essentially four level lasers. In the case of a single frequency laser like Nd:YAG, the laser transition takes place between two discrete states. In general the result of locating an active ion in a host material is to change its energy level structure. The energy levels of the ion undergo splittings due to the presence of the crystal field. The crystal itself is not stationery, but undergoes vibrations which are termed phonons. In the case of vibronic lasers

the energy levels involved in the lasing transition are broadened, by splitting, into bands by a strong interaction of the lasing ion with the lattice phonons of the crystal host. The lasing transition is thus tuneable within these bands.

Much effort is being devoted to the development of new laser materials in general and specifically new vibronic solid-state media which cover parts of the spectrum not yet covered by the presently available materials. In recent years the appearance of a selection of excellent new vibronic crystal media[7-10] has enabled these media, with their many advantages over cumbersome dyes, to be utilised as viable alternative solid-state sources of tuneable laser radiation. Besides the obvious advantages of reliability, longevity, improved beam quality and easy maintenance which solid-state media enjoy over dyes, they also offer the flexibility of either lamp- or diode-pumping as well as substantial energy storage lifetimes which facilitate the generation of high power pulses by Q-switching. The lack of flowing dye also reduces the noise and hence the linewidth[4,11] of these lasers.

The possible applications of these compact tuneable all solid-state sources are many and varied. In the research environment they offer the stability required for high resolution spectroscopy, holography and optical computing. The ultrashort pulses, obtainable due to their broad gain bandwidths through mode locking, offer opportunities for studying physical, chemical and biological processes on an extremely short time scale. They have commercial applications in material processing (micromachining), LIDAR (laser radar) and atmospheric studies (identification of gases). Satellite based global sensing and wind speed measurements are also possible. A compact source of blue radiation will have beneficial implications for digital data storage with higher information density being possible. A compact source of the three primary colours will make high resolution projection of large video images a reality. In the medical field, infrared sources covering the high absorption band of water will be useful. There are presently systems used for shattering kidney stones and for the non invasive removal of tattoos. The military too will find novel and useful applications for these lasers. Examples are: range finders, laser radar and target designators as well as in countermeasures packages against these.

With regard to this particular work, it was specifically the recent appearance of the very promising chromium-doped vibronic media, namely Cr:LiCAF and Cr:LiSAF[9,10], which provided the inspiration. These materials offer a major advantage over the existing vibronic media, namely Ti:sapphire and alexandrite, which cover similar regions of the near infrared. Their absorption bands are shifted into the region accessible by red laser diodes, enabling a compact tuneable source to be envisaged[12]. The other major advantage of the Cr-doped Colquiriites is their relatively long upper state lifetime[9,10] which permits efficient energy storage and hence Q-switching. These improvements brought about an opportunity for the development of all-solid-state laser for the generation of tuneable, nanosecond duration pulses in the near infrared[13]. It was this possibility which provided the impetus for this work.

At the outset of this work (1993), the available red laser diodes were not of sufficient brightness to be used as a pump source for Cr:LiCAF or Cr:LiSAF. It was therefore decided that the project would best be pursued by constructing a frequency-doubled, Q-switched, 1.321μm Nd:YLF laser as a substitute pump source. The output at about 660nm would be ideal for pumping either of the Cr-doped media. This Nd:YLF pump laser represented a novel source and was published[14] and presented at two conferences[15,16].

A comparison of Cr:LiSAF and Cr:LiCAF was carried out to see which was best suited for a diode-pumped, Q-switched tuneable laser. The comparison also considered the gain-switched performance under pumping from the Q-switched Nd:YLF laser. It was decided that Cr:LiSAF was the better of the two materials.

Because a gain-switched laser was envisaged due to pumping by a Q-switched solid-state laser, it was later decided that Ti:sapphire offered a superior alternative to achieving a pulsed, all-solid-state, tuneable, line-narrowed laser source. This also afforded an ideal opportunity to compare the gain-switched performance of Cr:LiSAF with the much more established Ti:sapphire. The development of these two lasers as well as the comparison of their respective performance has been presented at two conferences in 1995[15,16]. Ultimately the superior performance of Ti:sapphire meant that the initial goal of this work was achieved, not with Cr:LiSAF, but with Ti:sapphire. The development and performance of the single frequency,

gain-switched Ti:sapphire laser was presented at a conference at the end of 1995[17]. In fact the Ti:sapphire laser seems promising enough that it will hopefully attract commercial interest.

This thesis provides a detailed record of the development of the final all-solid-state, gain-switched, injection seeded Ti:sapphire laser. A detailed comparison of the four vibronic media, Alexandrite, Ti:sapphire, Cr:LiCAF and Cr:LiSAF is included. This justifies first the choice of Cr:LiSAF for the initial laser and second the switching of attention to Ti:sapphire as the most promising way to reach the goal. A detailed account of the development of both the Cr:LiSAF laser and the Ti:sapphire laser are presented. The development of the novel diode-pumped, Q-switched Nd:YLF laser and its frequency doubling is also discussed and presented in detail.

References

[1] T.M. Baer, *Laser Focus World*, **June**, (1986), p82

[2] R.L. Byer, *Science* , **239**, (1988), p742

[3] T.Y. Fan and R.L. Byer, *IEEE J. of Quant. Elec.*, **QE-24**, (1988), p895

[4] G.P.A. Malcolm and A.I. Ferguson, *Contemp. Phys.*, **32**, (1991), p305

[5] T.Y. Fan, "Diode-pumped solid-state lasers", Talk given at St. Andrews University Summer School on Physics, **June**, (1995)

[6] Environmental Optical Sensors, Inc., *2001 Tunable Diode Laser*, Gunpark Drive, Boulder, CO 80301-3376, USA

[7] P.F. Moulton "New developments in solid state lasers", *Laser Focus* , **May**, (1983), p83

[8] J.C. Walling, O.G. Peterson, H.P. Jenssen, R.C. Morris, and E.W. O'Dell, "Tunable alexandrite lasers", *IEEE J. of Quant. Elec.*, **QE-16**, (1980), p1302

[9] S.A. Payne, L.L. Chase, H.W. Newkirk, L.K. Smith and W.F. Krupke, "$LiCAF_6:Cr^{3+}$: A Promising New Solid-State Laser Material", *IEEE J. of Quant. Elect.*, **QE-24**, (1988), p2243

[10] S.A. Payne, L.L. Chase, L.K. Smith, W.L. Kway and H.W. Newkirk, "Laser performance of $LiSrAlF_6:Cr^{3+}$, *J. Appl. Phys.*, **66**, (1989), p1051

[11] P.A. Schulz, "Single-Frequency Ti:Al_2O_3 Ring Laser", *IEEE J. of Quant. Elec.*, QE-24, (1988), p1039

[12] R. Scheps, "Cr-doped solid state laser pumped by visible laser diodes", *Opt. Materials*, 1, (1992), p1

[13] L.L. Chase and S.A. Payne, "New Tunable solid-state lasers Cr^{3+}:$LiCaAlF_6$ and Cr^{3+}:$LiSrAlF_6$", *Opt. and Phot. News*, August, (1990), p16

[14] G.R. Morrison, M. Ebrahimzadeh, C.F. Rae and M.H. Dunn, "Diode-pumped, Q-switched, 1.321μm Nd:YLF laser and its frequency doubling", *Opt. Comm.*, 118, (1995), p55

[15] G.R. Morrison, M. Ebrahimzadeh, C.F. Rae and M.H. Dunn, "All-solid-state gain-switched vibronic lasers as sources of tunable, narrow-linewidth light", The Rank Prize Funds, Mini-Symposium on Solid-State Lasers, April 1995

[16] G.R. Morrison, M. Ebrahimzadeh, C.F. Rae and M.H. Dunn, "All-solid-state gain-switched Cr:LiSAF laser", Conference on Lasers and Electo-optics (CLEO '95), Baltimore USA, May 1995, Technical Digest Series 15 , p15

[17] G.R. Morrison, C.F. Rae, M. Ebrahimzadeh and M.H. Dunn, "Comparison of all-solid-state gain-switched Cr:LiSAF and Ti:sapphire lasers", Quantum Electronics Conference (QE-12), Southampton UK, September 1995, Technical Digest, P3-1

CHAPTER 2

THEORETICAL PRELIMINARIES

This chapter deals with the theoretical background for this work. It begins with a discussion on the basic laser theory. This is developed into a model which can be used to predict the performance of the laser systems developed here. Descriptions are also given of resonator design, second harmonic generation and injection seeding which have also been utilised.

2.1 Theory of laser action

In this section a basic theoretical treatment of laser action will be presented. This will then be developed into a laser model which can be used to aid design considerations, promote understanding of the physical processes involved and will also enable estimation and comparison of the actual laser performance to be made. References [1] and [2] have been used extensively.

2.1.1 Interaction of radiation and matter

It is necessary to begin by briefly considering the interaction of radiation with an atomic system. Specifically, the concepts of spontaneous emission, stimulated absorption and stimulated emission will be introduced. These processes can be described in terms of the Einstein coefficients. To maintain simplicity an idealised atomic system consisting of two energy levels E_1 and E_2 with corresponding average population densities n_1 and n_2, and E_2-E_1= $h\nu_{21}$ is considered. Here ν_{21} is the frequency of the radiation resulting from a transition between the levels. It is also important to specify the form of the electromagnetic radiation which will interact with this system. This will be described in terms of an energy density per unit frequency. In general the radiation can be expressed in terms of a photon density, ϕ. Within this photon density there will exist photons characterised by a continuous range of frequencies. This spread in photon frequencies centred about ν_0 can be described by a normalised lineshape function $g(\nu,\nu_0)$, which is generally a Gaussian or Lorentzian

distribution, or some combination of the two called a Voight profile. Thus the energy density per unit frequency can be expressed by

$$\xi(\nu) = h\nu g(\nu, \nu_0)\phi. \qquad (2.1.1)$$

A detailed description of the lineshape function will not be given here. Suffice it to say that as well as the incident field being described by its lineshape function, the emission from an atomic transition will similarly be described by its lineshape function which will depend in detail on the local environment and the lifetime of the transition. Thus in the idealised model considered here, the assumption of infinitely sharp energy levels resulting in monochromatic radiative emission has been made. In general, consideration of the overlap of the lineshape functions of the atomic transition and the interacting electromagnetic field is required.

Spontaneous emission

An atom initially in the upper level will decay spontaneously to the lower level at a rate proportional to the average population density of the upper level.

$$\frac{\partial n_2}{\partial t} = -A_{21} n_2 \qquad (2.1.2)$$

Here A_{21} is the Einstein coefficient of spontaneous emission and represents the transition probability per unit time for a spontaneous emission transition to occur between two given energy levels. The reciprocal of this transition rate is just the lifetime for spontaneous emission from level 2,

$$\tau_{21} = 1/A_{21} \,. \qquad (2.1.3)$$

This definition is apparent when the solution of Equation (2.1.2) for spontaneous emission is considered,

$$n_2(t) = n_2(0)\exp\left(-t/\tau_{21}\right). \qquad (2.1.4)$$

Stimulated absorption

The case of stimulated transitions deals explicitly with the interaction of radiation and matter. The assumption of a quasi monochromatic beam of frequency ν_{21} passing through the two

level system is made. In this case the lower level will be depopulated at a rate proportional to both the lower level population density and the beam energy density per unit frequency $\xi(\nu_{21})$, according to

$$\frac{\partial n_1}{\partial t} = -B_{12}\xi(\nu_{21})n_1. \qquad (2.1.5)$$

Here $B_{12}\xi(\nu_{21})$ can be viewed as the stimulated absorption transition rate or the probability per unit frequency that the radiation will induce a transition from level 1 to level 2.

Stimulated emission

In an analogous fashion to absorption, an atomic system with a transition frequency ν_{21} can be induced to emit radiation in the presence of an electromagnetic field of the same frequency. This process is termed stimulated emission. With the same set-up as above, the rate of change of the upper level population density in response to stimulated emission can be expressed by

$$\frac{\partial n_2}{\partial t} = -B_{21}\xi(\nu_{21})n_2 \qquad (2.1.6)$$

where $B_{21}\xi(\nu_{21})$ represents the stimulated emission rate or probability per unit frequency that stimulated emission will take place.

Evaluation of the Einstein coefficients

A simple relationship exists between the Einstein A and B coefficients. If the atomic system is considered to be in thermal equilibrium, then the populations of the levels are described by Boltzman statistics

$$\frac{n_2}{n_1} = \exp\left(\frac{-(E_2 - E_1)}{kT}\right) \qquad (2.1.7)$$

Also, the net rate of change of the level populations due to the various emission and absorption processes must be zero or in other words, the number of emissions should equal the number of absorptions. Thus equating equation (2.1.5) with equations (2.1.6) and (2.1.2),

and using equation (2.1.7) enables the following expression for the radiation density for a body in thermal equilibrium to be obtained:

$$\xi(\nu_{21}) = \frac{\left(A_{21}/B_{21}\right)}{\left(B_{12}/B_{21}\right)\exp\left(h\nu_{21}/kT\right) - 1} \qquad (2.1.8)$$

However, a body in thermal equilibrium acts like a black body and hence radiates according to Planck's law,

$$\xi(\nu) = \frac{8\pi\nu^2}{c^3}\frac{h\nu}{\exp\left(h\nu/kT\right) - 1} \qquad (2.1.9)$$

Equating equations (2.1.8) and (2.1.9) gives the relationships between the Einstein coefficients:

$$\frac{A_{21}}{B_{21}} = \frac{8\pi\nu^2 h\nu}{c^3} \quad \text{and} \quad B_{21} = B_{12} \qquad (2.1.10)$$

It should be noted that the simplified system considered here is degenerate, i.e. there are no level splittings or fine structure. In general each energy level may actually consist of a number of components, counted by the multiplicity factor, g_i, which only reveal themselves when the active ion is subject to external fields (like that of the host crystal). In the case of a non-degenerate system, the fine structure of each energy level is revealed and the energy level is seen to consist of a number of splittings. These splittings will share out the population of that level equally. The different degeneracies of the two levels in the above system are taken into account in the second of the above relationships by multiplying the left hand side by the factor g_1/g_2.

Macroscopic absorption and amplification

In this section the Einstein coefficients will be related to macroscopic physical constants which are more easily used in analysing laser action. Consider a collimated, quasi-monochromatic beam of energy density $\xi(\nu_s)$, incident on the simplified two level system. The system will react to the presence of this beam by undergoing stimulated absorption and

emission as described above. Notice that spontaneous emission has been neglected in this analysis. Using equations (2.1.5) and (2.1.6), the net rate of change of the population density of the lower level is described by

$$\frac{\partial n_1}{\partial t} = -B_{21}\xi(\nu_s)\left(\frac{g_2}{g_1}n_1 - n_2\right) \qquad (2.1.11)$$

It should be noted that an assumption about the lineshape of the stimulated transition has been made. The assumption, which is part of the simplified two-level model being used, is that all atoms in the volume of the incident field will undergo stimulated transitions. In general broadening of the atomic transition as described by its probability factor $g(\nu, \nu_{21})$ would have to be accounted for, and the overlap of this with the lineshape function of the incident field must be considered. Equation (2.1.11) may be transformed into an equation describing the evolution of the incident beam as it passes through the medium. By multiplying both sides by $h\nu$ and noting that in time dt the beam travels a distance dx, where $dt = dx/c$, equation (2.1.11) can be written as:

$$\frac{\partial \xi(\nu_s)}{\partial x} = -\frac{h\nu_s}{c}B_{21}\xi(\nu_s)\left(\frac{g_2}{g_1}n_1 - n_2\right) \qquad (2.1.12)$$

which has the solution

$$\xi_s(x) = \xi_s(0)\ \exp(-\alpha(\nu_s)x) \qquad (2.1.13)$$

where an absorption coefficient has been defined as

$$\alpha(\nu_s) = \sigma_{21}(\nu_s)\left(\frac{g_2}{g_1}n_1 - n_2\right) \qquad (2.1.14)$$

and an absorption cross-section has also been introduced:

$$\sigma_{21}(\nu_s) = \frac{h\nu_s}{c}g(\nu_s, \nu_{21})B_{21} \qquad (2.1.15)$$

Notice that the factor $g(\nu_s, \nu_{21})$ which describes the overlap of the incident field frequency distribution and the frequency spread function of the atomic transition has been included for completeness. Equation (2.1.13) indicates that as the electromagnetic wave travels through the medium, it experiences exponential absorption. However, from equation (2.1.14) it is seen

that if the system can be arranged so that more atoms are in the upper level ($n_2 > n_1$), then the incident wave will be amplified exponentially. In the case of gain, equations (2.1.13) and (2.1.14) are rewritten as:

$$\xi_s(x) = \xi_s(0)\ \exp(g(\nu_s)x) \qquad (2.1.16)$$

and

$$g(\nu_s) = \sigma_{21}(\nu_s)\left(n_2 - \frac{g_2}{g_1}n_1\right) \qquad (2.1.17)$$

respectively, where $g(\nu_s)$ is the gain coefficient. These processes are all of critical importance in achieving laser action. However, lasing is only possible in a select group of materials. It is therefore necessary to consider the requirements for a good laser medium. A simplified four-level model of an atomic system will suffice to illustrate these requirements and will also yield some useful expressions for describing laser action.

2.1.2 Basic theory of a four-level laser

The four-level atomic system

All the solid-state media investigated here can be represented as four-level systems. Therefore the theory used to describe laser action will be based on this model. To be useful as a laser medium it is necessary, as was mentioned above, that a population inversion can be induced. Generally the energy levels in a collection of atoms, constituting the medium, will be populated according to the thermal distribution described by Boltzman statistics. However, by an externally applied excitation or pump mechanism to the medium, these average population densities can be rearranged. Provided a few simple criteria are satisfied by the medium, this can result in a population inversion between two of the atomic energy levels. It is these energy levels which give rise to the laser transition because the photons emitted by this transition, if appropriately fed back, will stimulate further emission and thus result in laser action. Figure 2.1 depicts the situation involved in stimulated emission from an optically pumped idealised 4-level atomic system. The pumping mechanism depopulates the ground state $|0\rangle$ at a rate W_p. The pumped atoms are excited into the pump band (level $|3\rangle$) from

which they can decay back to the ground state by various routes. Most of the atoms will decay rapidly by a nonradiative transition (τ_{32} fast) to the upper laser level |2>. This level is required to be a metastable level, i.e. long lived ($\tau_{21} >> \tau_{32}, \tau_{10}$). In this way most of the pumped atoms will end up in the upper laser level. The final requirement to ensure a population inversion is that the atoms which have undergone the transition from the upper laser level |2> to the lower laser level |1> are then rapidly de-excited back down to the ground state, or $\tau_{10} << \tau_{21}$. Thus to be a useful laser medium it is crucial that the upper laser level be a metastable level. In addition the absorption band (or pump band), and the lower laser level must decay extremely rapidly to the upper laser level and the ground state, respectively. This requirement amounts to both these transitions being between closely separated levels so that they can proceed by rapid nonradiative decay processes. In solid-state media these transitions correspond to phonon excitations of the crystal lattice. The metastable state will have no such nearby levels and its only decay routes are by weak optical transition to the lower laser level or slow multi-phonon processes. In this way a population inversion is easily built up between level |2> and level |1>. Ideally these requirements will be accompanied by a lower laser level which is high enough above the ground state so that its thermal population is negligibly small.

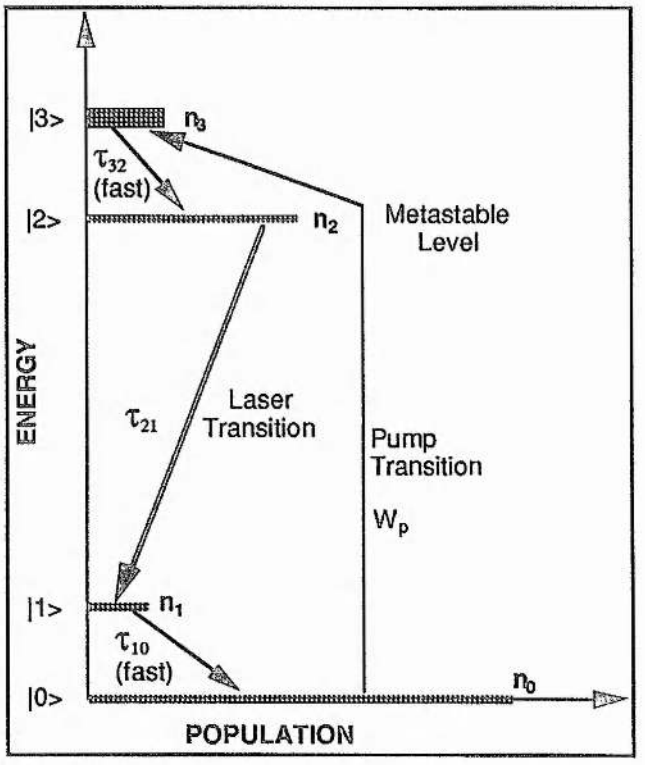

Figure 2.1: Depicts a simplified energy level diagram of a four-level laser.

The population inversion rate equation

If the above criteria are all satisfied, then the only level whose population changes appreciably is that of the upper laser level. The rate of change of the upper laser level population density is given by:

$$\frac{dn_2}{dt} = W_p n_0 - n_2 \sigma_{21} \phi c - \frac{n_2}{\tau_f}. \qquad (2.1.18)$$

Here the pumping $W_p n_0$ is seen to increase the population density while both the stimulated emission $n_2 \sigma_{21} \phi c$, (using equation (2.1.1) in (2.1.11) with (2.1.15)), and spontaneous emission n_2/τ_f, (from equation (2.1.2) with (2.1.3)), are seen to reduce the population density. The factor $1/\tau_f = 1/\tau_{21} + 1/\tau_{20}$ is the total spontaneous emission lifetime out of the upper laser level. Implicit in this equation are all the criteria mentioned above. To reiterate, the extremely rapid depopulation of levels |3> and |1> implies that $n_1 \approx n_3 \approx 0$ and the assumption was made that the number of excited atoms is small compared to the total number, or

$$n_d = n_o + n_2 \cong n_o \qquad (2.1.19)$$

Here n_d is the total number density of atoms in the system and so corresponds to the dopant density in a rare earth doped laser crystal. With these assumptions, equation (2.1.18) describes the evolution of the population inversion. It now remains to consider how this population inversion can be exploited to achieve laser action.

Decay of a field within a resonator

To complete the description of laser action within this model, an equation describing the build-up of the radiation field is required. This equation together with equation (2.1.18) will form two coupled equations describing the dynamic interaction of the population inversion and the radiation intensity. However, before the equation describing the radiation can be written down the mechanism by which the radiation within a laser resonator decays must be considered. As mentioned above laser action requires a feedback mechanism whereby the photons emitted at the laser transition are sent back through the medium so that further emission can be stimulated. The feedback is usually provided by a set of mirrors forming a

resonator around the medium. Discussion of the particular requirements of such an optical resonator will be deferred until a later section, but for now a laser medium of length l, contained within a simple resonator consisting of two mirrors of reflectivity R_1 and R_2, separated by a distance l' is considered.

The decay of the circulating field which has been built up in this resonator is now investigated. If the gain mechanism is switched off at time $t=0$, the evolution of the circulating radiation is given by,

$$\frac{\partial \xi}{\partial t} = -\frac{\xi}{\tau_c} \tag{2.1.20}$$

which has a solution

$$\xi(t) = \xi(0)\exp\left(-t/\tau_c\right) \tag{2.1.21}$$

describing exponential decay of the circulating radiation. In this picture τ_c can be interpreted as the average lifetime of photons in the resonator. It will now be shown that τ_c represents all the losses in the resonator. Using equation (2.1.13), the absorption losses as the radiation passes through the gain medium as well as losses upon reflection at the mirrors can be accounted for, so that after one round trip, the circulating intensity can be described by

$$\xi(2l') = \xi(0)R_1R_2\exp(-2\alpha l)\prod_i T_i^2 \tag{2.1.22}$$

Here α represents the parasitic absorption losses associated with transmission through the medium (laser crystal) and the T_i are the one way transmissions through the i^{th} internal element. This represents diffraction at the apertures, reflective losses at the surfaces, scattering and other parasitic losses. Now equation (2.1.22) will be the same as equation (2.1.21) when it is also evaluated after one round trip, taking time

$$t_R = 2l'/c \tag{2.1.23}$$

Comparing these two equations after one round trip and solving for τ_c, yields

$$\tau_c = \tau_R\left[L + \ln\frac{1}{R}\right]^{-1} \tag{2.1.24}$$

where all the losses have been lumped into a single factor

$$L = 2\alpha l \ln\left(R_1 \prod_i T_i^2 \right)^{-1} \qquad (2.1.25)$$

so that $R = R_2$ represents the reflectivity of the output coupler. It can therefore be seen that the cavity decay time represents the various losses in the optical resonator.

The laser rate equations

The loss mechanism, (equation (2.1.20) with (2.1.24)) described above, for the radiation circulating in the resonator can now be combined with the gain mechanism, (expressed in equations (2.1.12) and (2.1.17)) derived in section (2.1.1), to obtain an equation describing the evolution of the circulating radiation in a laser cavity. Equation (2.1.1) can be used so that the following equation

$$\frac{d\phi}{dt} = n_2 \sigma_{21} \phi \frac{l}{l'} c - \frac{\phi}{\tau_c} + S \qquad (2.1.26)$$

describing the changing photon density (in cm^{-3}) is obtained. The term S, describes the contribution of spontaneous emission at the appropriate frequencies. These appropriate frequencies are the frequencies supported by the optical resonator (see section (2.2.2)), which lie under the gain bandwidth of the laser medium. This spontaneous emission term will be considered in more detail in section 2.4 when injection seeding of a laser is discussed. For the most part it will represent an insignificant contribution and for now it will be neglected. The factor l/l' represents the fact that at any given time only the fraction of the photons in the gain medium will undergo amplification. For completeness Equation (2.1.18) describing the evolution of the population inversion is rewritten here,

$$\frac{dn_2}{dt} = W_p n_0 - n_2 \sigma_{21} \phi c - \frac{n_2}{\tau_f} \qquad (2.1.27)$$

since these two equations form a coupled system, commonly called the laser rate equations, which can be used to describe laser action. These coupled rate equations will now be used to describe a few important features of lasers.

The oscillation condition and laser threshold

The oscillation condition is obtained by considering the solution of equation (2.1.26),

$$\phi(t) = \phi(0)\exp(cgl/l' - 1/\tau_c)t, \qquad (2.1.28)$$

where equation (2.1.17) has been used. In order to achieve oscillation the photon density is required to remain the same after one round trip of the resonator, taking a time $t = t_R = 2l'/c$. This amounts to the argument of the exponential in the above equation being equal to zero, or using equation (2.1.24),

$$2gl = L + \ln\frac{1}{R} \qquad (2.1.29)$$

which amounts to the round-trip gain just balancing the round-trip losses. This also represents the threshold condition, since for a slightly higher gain, the gain will be able to overcome the cavity losses and the circulating radiation will build-up exponentially. From the above threshold condition the required population inversion can be calculated. Substituting for the gain g, from equation (2.1.17) in the above and solving for the population inversion yields

$$n_{th} = \frac{l'}{lc\sigma_{21}\tau_c} \qquad (2.1.30)$$

for the threshold population inversion. This can be obtained directly from equation (2.1.26) with $d\phi/dt = 0$ as appropriate for threshold operation. This can be related to a threshold pumping rate by noting that at threshold the population inversion will be in a steady-state $\partial n_2/\partial t = 0$ and there is zero circulating field, $\phi = 0$. Substitution of these conditions into equation (2.1.27) yields

$$W_{p(th)} = \frac{n_{th}}{n_d \tau_f} \qquad (2.1.31)$$

To make contact with real systems it is important to examine the various efficiency factors relating this pumping rate to an actual pumping mechanism. Before this is done, however, it is necessary to first look at the circulating power within a laser operating above threshold and how the build-up of this circulating power diminishes the gain.

2.1.3 Laser operation above threshold

Gain saturation

Regarding the case of a system initially far above threshold, it is clearly no longer in the regime of small signal ($\phi \cong 0$) gain discussed above. The gain will now be greater than that specified by the threshold condition expressed in equation (2.1.29), and so the circulating intensity will build-up rapidly according to equation (2.1.28). However, equation (2.1.27) indicates that a large circulating photon density will tend to reduce the population inversion and hence the gain. The population inversion will eventually reach a steady state $dn_2/dt = 0$ and hence the gain will settle down to a value such that population reduction caused by the stimulated and spontaneous emissions will just balance the population increases resulting from pumping,

$$n_2 = \frac{W_p n_0 \tau_f}{1 + \sigma_{21} \phi c \tau_f} \tag{2.1.32}$$

Converting the photon density into an intensity

$$I = h\nu\phi c, \tag{2.1.33}$$

defining a saturation intensity by

$$I_s = h\nu / \sigma_{21}\tau_f \tag{2.1.34}$$

and using equation (2.1.17) enables equation (2.1.32) to be rewritten as

$$g = \frac{g_0}{1 + I/I_s} \tag{2.1.35}$$

where

$$g_0 = \sigma_{21} W_p n_d \tau_f \tag{2.1.36}$$

has been defined as the initial, unsaturated gain of the system. The above definition of the saturation intensity is now clear as that circulating intensity which reduces the gain to one half of its initial value. This phenomenon is known as gain saturation and has been shown to be caused by the build-up of a strong circulating intensity. Finally, it should be noted that this derivation is only applicable to homogeneously broadened media where all active atoms in the medium are in the same local environment. Comparison with non-homogeneously broadened systems will not be considered here.

Output power

When trying to predict the output power emitted by a laser, more care must be taken in the discussion of the circulating power. Essentially in a laser resonator there will be two travelling waves, one moving left and one moving to the right. In the case of a small output coupling, the intensities of these two waves are essentially the same and of equal magnitude to the circulating intensity. Thus in the laser medium the intensity is the sum of the left and right propagating waves, so that

$$I = I_R + I_L \cong 2I_{cir} \tag{2.1.37}$$

Since the gain saturation, equation (2.1.35), was derived for a single pass situation, the above expression is substituted, yielding

$$g = \frac{g_0}{1 + 2I_{cir}/I_S} \tag{2.1.38}$$

for the gain saturation in a laser oscillator with a circulating field. The power output from such a laser oscillator can be obtained by considering only that portion of equation (2.1.26) representing useful output coupling

$$P_{out} = -h\nu Al' \frac{d\phi}{dt}\bigg|_R \tag{2.1.39}$$

Here Al' is the volume of the laser mode in the cavity. Using equation (2.1.26) together with equation (2.1.24) the output photon rate can be replaced to obtain

$$P_{out} = \frac{h\nu Al'}{t_R}\phi \ln\frac{1}{R} \tag{2.1.40}$$

This can be written in a more useful form by using equations (2.1.33) and (2.1.37) yielding the output power in terms of the circulating intensity

$$P_{out} = AI_{cir} \ln\frac{1}{R} \tag{2.1.41}$$

In the case of small output coupling the logarithmic factor can be replaced by the transmission, $T = (1 - R) \approx 1/\ln R$ of the end mirror.

2.1.4 Operational efficiency

In order that this description of a laser can be useful in modelling real results, account needs to be taken of the various idealisations which have been made to simplify the discussion. Fortunately most of these modifications can be applied in a straight forward manner as reductions in the incident pump power, yielding an effective pump power which contributes solely to the laser process. The various efficiency factors which link the model to reality will now be discussed in turn. With the exception of the energy storage efficiency factor associated with Q-switching, all the factors described below apply equally well to pulsed and CW modes of operation.

Coupling efficiency

The coupling efficiency factor η_T refers to the reduction in pump power as it is delivered into the laser medium. Since all of the systems considered here are solid-state laser, end-pumped systems, only this much simplified situation is of concern here. In this case the efficiency with which the pump light is delivered into the laser rod aperture accounts for losses in the transmission through the coupling optic arrangement as well as the loss incurred in passing through the end mirror of the laser cavity. The highly divergent nature, in one plane, of the pump laser diodes inevitably leads to transmission losses as conventional optics struggle to capture and suitably control the output of these sources[3,4]. Various novel schemes have been devised to improve coupling efficiency,[5,-8] but most are limited to about 85% efficiency. A third possibility is to design the laser resonator with an elliptical mode which overlaps the naturally elliptical pump mode produced by laser diode pumps[9]. In the case of solid-state laser pumping of another laser, near diffraction limited quality of the pump beams means that coupling efficiencies approaching 100% are routinely attained. For end-pump laser systems

$$\eta_T \cong 0.85 - 0.99 \qquad (2.1.42)$$

is generally attained.

Pump absorption efficiency

This factor basically accounts for the fact that due to the nature of the absorption process, some pump radiation will be lost to the system. As shown in section (2.1.5), radiation is

absorbed exponentially with distance travelled through the medium. From equation (2.1.13) it follows that the ratio of power absorbed to incident power is given by

$$\eta_a = 1 - \exp(-\alpha l) \qquad (2.1.43)$$

for a medium of length l. Again this factor owes its simplicity to the fact that laser diode pump sources emit over a narrower frequency range than the absorption band of many solid-state media and this frequency can usually be tuned to coincide with the peak of the absorption band of a given medium.

Care must be taken to avoid saturation effects for this equation is to be accurate. In the same way that the gain of a laser can be saturated by the circulating field, the absorption of the pump can become saturated. Saturation of the absorption can be expressed by an identical expression to equation (2.1.35) for gain saturation. The difference is in the saturation intensity. In the case of gain, the saturation intensity as given by equation (2.1.34), depends on the stimulated emission cross-section. In the case of the absorption, however, the absorption saturation intensity depends similarly on the absorption cross-section. It should be noted that the relevant frequency in this case is that of the pump radiation and not that of the oscillating field.

<u>Spatial mode overlap efficiency</u>

This factor, as discussed here, is specific to diode end-pumping and solid-state laser pumping, Side pumping and flashlamp pumping require a more complex analysis. It takes account of the fact that the Gaussian nature of the pump beam and also of the circulating laser power has been neglected. It can be easily incorporated into the laser model by assuming a Gaussian spatial distribution for the population inversion, as determined by the pump laser mode in the end-pumped geometries being considered here. As mentioned earlier, discussion of the selection of a laser mode by appropriate resonator design will be delayed until a later section. For now a Gaussian laser mode is assumed. Inclusion of these considerations into the model requires only that an overlap integral of these spatial modes within the gain medium[10-14] is considered. With the assumption of TEM_{00} Gaussian modes the overlap efficiency factor becomes,

$$\eta_B = \frac{2\varpi_l^2}{\varpi_p^2 + \varpi_l^2} \qquad (2.1.44)$$

where ϖ_p and ϖ_l are the beam waist sizes of the pump and laser modes averaged through the medium. The above efficiency factor becomes unity when the pump mode is smaller than the laser mode. In fact the above described analysis does not require detailed knowledge of the beam cross-sectional energy distribution, showing instead that consideration of beams of uniform transverse energy distribution within a defining radius is sufficient[11,12]. Optimum focusing of the pump power in terms of lowering the threshold amounts to achieving a focus such that the pump beam (and hence the laser) Rayleigh range is equal to the length of the laser medium[13].

Upper state efficiency

The upper state efficiency accounts for two sources of loss. The first is the fact that energy is lost in the rapid nonradiative decays between the pump level and the upper laser level and also in those between the lower laser level and the ground state. This is known as the Stokes efficiency and is represented by the ratio of the energy of a laser photon to that of a pump photon, thus

$$\eta_S = \frac{\nu_l}{\nu_p} = \frac{\lambda_p}{\lambda_l} \qquad (2.1.45)$$

Secondly, as noted in the four-level laser model, not all atoms excited into the upper laser level will undergo the laser transition. Some will decay via other spontaneous decay routes. This is known as the quantum efficiency and is given by

$$\eta_Q = \frac{\tau_3}{\tau_{32}} \frac{\tau_f}{\tau_{21}} \leq 1 \qquad (2.1.46)$$

Here τ_3 is the fluorescence decay time, through all routes, out of the pump band and similarly τ_f is the fluorescence lifetime of the upper laser level. Therefore this efficiency factor represents the ratio of the number of laser photons to the number of absorbed pump photons. Provided the medium satisfies the conditions of a four-level system, this factor approaches

unity. Extremely rapid thermal repopulation of the upper laser level from within the manifold containing the upper laser level ensures that high quantum efficiencies are attained.

Energy storage efficiency

This efficiency factor takes account of the fact that stored energy leaks out of the medium by spontaneous decay during the gain build-up process required for Q-switching. In Q-switching the aim is to store pump energy and deliver it in pulses of much shorter duration and thus attain very high peak powers. This is achieved by maintaining the cavity in a low Q state (high loss) whilst the medium is strongly pumped. At the end of the pump cycle, which is of an appreciable duration with respect to the upper state lifetime, the cavity Q is switched to a high Q state (low losses) and a powerful pulse will rapidly build-up. During the pumping cycle energy will leak away by spontaneous decay so that the gain upon Q-switching may be substantially lower than the case where no leakage is considered. In this case of no leakage the population inversion will be given by $n_2 = W_p n_d \tau_f$. During a pumping cycle of duration τ_P the population inversion will decay exponentially at a rate determined by the upper state lifetime so that the actual population inversion density is given by

$$n_2 = W_p n_d \tau_f \left(1 - \exp(-\tau_P/\tau_f)\right) \qquad (2.1.47)$$

Dividing by the integrated population inversion over the pumping cycle, i.e. $W_p n_d \tau_P$ gives the fraction still available at the time of Q-switching and hence the storage efficiency

$$\eta_{st} = \frac{\left[1 - \exp(-\tau_p/\tau_f)\right]}{\tau_p/\tau_f}. \qquad (2.1.48)$$

From this efficiency factor it is seen that the highest efficiency is achieved for a pump cycle short compared to the fluorescence lifetime. This should be intuitive since a short pump cycle relative to the upper state lifetime will provide a correspondingly short period for deleterious decay to occur. In this limit of a very short pump cycle, we can no longer truly consider the process to be that of Q-switching, instead it is referred to as gain-switching. This terminology refers to the fact that essentially the gain has been turned from low to high before the system

can reach threshold even in the high Q state. As such there is no need to physically switch the Q of the cavity. In the case of gain-switching the storage efficiency factor is set to unity.

2.1.5 Measurable quantities

In this section a description is given of how the measurable output quantities of a laser are determined by the internal parameters discussed in the above model. This relationship for the case of quasi-cw lasers is presented so that the results may be applied to the systems which were investigated. The output energy is obtained by integrating equation (2.1.41) for the output power over the pump duration. Assuming a square wave pump pulse of duration τ_p, this gives

$$E_{out} = AI_{cir}\tau_p \ln\frac{1}{R} \qquad (2.1.49)$$

The circulating intensity can now be substituted for by making use of equation (2.1.38). Also assuming that the pump cycle is of sufficient duration, the gain in equation (2.1.38) will be saturated by the effect of the circulating field and will approach the steady state gain value determined by the threshold condition given by equation (2.1.29). With these substitutions equation (2.1.49) becomes

$$E_{out} = \left(\frac{\ln\frac{1}{R}}{L+\ln\frac{1}{R}}\right) AI_s g_0 l\tau_p - \frac{AI_s \ln\frac{1}{R}}{2}\tau_p \qquad (2.1.50)$$

where the saturation intensity is given by equation (2.1.34). Recalling that the unsaturated gain is proportional to the pumping rate, $g_0 = \sigma_{21} W_p n_d \tau_f$ (equation (2.1.36)), this can be rewritten in terms of the power of the pump source and the various efficiency factors described earlier. Since $W_p n_d$ represents the population inversion density created by the pump mechanism per unit time, it can be written in terms of the absorbed pump power P_{abs} as

$$W_p n_d = \eta_Q \eta_S \frac{P_{abs}}{h\nu_l V} \qquad (2.1.51)$$

where V represents the pumped volume of the laser medium. The quantum efficiency has been included to account for the number of absorbed pump photons which don't lead to a

laser transition and the Stokes efficiency accounts for the energy differential between a pump photon and a laser photon. If the various efficiency factors, discussed earlier, which quantify the losses associated with coupling the pump light into the active medium are included, then equation (2.1.51) can be rewritten in terms of the input pump power as

$$W_P n_d = \eta_Q \eta_S \eta_T \eta_B \eta_a \frac{P_{in}}{h\nu_l V} \tag{2.1.52}$$

Substituting this into equation (2.1.36) yields

$$g_0 l = \eta \frac{P_{in}}{I_S A} = K' E_{in} \tag{2.1.53}$$

for the unsaturated gain. All the efficiency terms of equation (2.1.52) $\eta = \eta_Q \eta_S \eta_T \eta_B \eta_a$ have been grouped and a pump constant

$$K' = \frac{\eta}{I_S A \tau_P} \tag{2.1.54}$$

has been introduced, which relates the gain through the crystal in the absence of saturation to the pump energy. The assumption of a square wave pump of duration τ_P and energy $E_{in} = P_{in}\tau_P$ has been made. The output energy, as in equation (2.1.50), can now be written in terms of the total pump energy, yielding

$$E_{out} = \left(\frac{\ln \frac{1}{R}}{L + \ln \frac{1}{R}} \right) \eta E_{in} - \frac{A I_s \ln \frac{1}{R}}{2} \tau_P \tag{2.1.55}$$

It will be useful to simplify this expression by lumping all the resonator parameters, obtaining

$$E_{out} = \sigma_s \left(E_{in} - E_{th} \right) \tag{2.1.56}$$

where σ_s represents the slope efficiency of the laser as measured by taking an input versus output measurement of the laser. Basically this sums up the overall optical efficiency of the system. Further efficiency factors may be included to account for the conversion from electrical to optical energy. By comparing equations (2.1.56) and (2.1.55) the following expression for the slope efficiency is obtained:

$$\sigma_s = \left(\frac{\ln \frac{1}{R}}{L + \ln \frac{1}{R}} \right) \eta_Q \eta_S \eta_T \eta_B \eta_a \qquad (2.1.57)$$

and the threshold pump energy required is given by

$$E_{th} = \left(\frac{L + \ln \frac{1}{R}}{2} \right) \frac{1}{K'} \qquad (2.1.58)$$

From these two expressions it is apparent that the various efficiency factors should be as close to unity as possible for increased system efficiency and reduced threshold. Similarly internal losses should be kept to a minimum for best performance. For resonators with small output coupling the approximation $T \cong -\ln R$ is valid and so differentiating equation (2.1.55) with respect to output coupling will enable the optimum output coupling for a given laser to be determined.

$$T_{opt} = \left(\sqrt{2 g_0 l / L} - 1 \right) L \qquad (2.1.59)$$

The approximation of small output coupling is reasonable for all the end-pumped systems considered in this work. From this result it is clear that increased small signal gain requires increased output coupling for optimised performance. In many lasers the small signal gain will be much larger than the internal losses so that the required output coupling for optimised performance scales with internal losses. A final point to note is that for the threshold condition where gain equals the internal losses, the optimised output coupling is zero as expected.

A method whereby the cavity losses L and the product of the efficiency factors η can be measured will now be discussed. This will enable equation (2.1.56) to be used to estimate the output energy of the laser. The method was first proposed by Findlay and Clay[15] and it utilises equation (2.1.58) which can be rewritten as

$$-\ln R = 2K' E_{th} - L \qquad (2.1.60)$$

Thus by measuring the threshold energy as a function of output coupling enables the $2K'$ and the internal losses L, to be respectively determined from the slope and intercept of the

corresponding plot. These two values can then be used in equation (2.1.59) to determine the output coupling required to optimise the system. From the slope together with equation (2.1.54) the system efficiency factors can be calculated provided the pump beam area in the laser medium is known. It should be noted, however, that in systems end-pumped by laser diodes the various efficiency factors can be estimated reasonably accurately. This method has been extended to situations where the pump intensity profile is accurately known by Hodgson and Weber[16].

2.2 Resonator Physics

As a prelude to considering resonator design, a description of the propagation of radiation fields is required. The basic relevant results for the propagation of Gaussian beams are considered below. Reference texts[17,18].

2.2.1 Gaussian beam propagation

The simplest case of the propagation of the fundamental Gaussian mode will be considered here. This mode is characterised by azimuthal symmetry and has a Gaussian intensity distribution in cross-section. The case of beams with other modulations superimposed on the cross-sectional intensity distribution will be dealt with later. An azimuthally symmetric field propagating in the z-direction through a homogeneous medium is described by

$$\vec{E}(x,y,z,t) = \mathrm{Re}[\vec{E}(r,z)e^{i(\omega t - kz)}] \qquad (2.2.1)$$

In the slowly varying amplitude approximation, the solution of the wave equation for a single such component is found to be:

$$E(r,z) = E_0 \frac{w_0}{w(z)} \exp\{-i[kz - \theta(z)] - r^2[1/w^2(z) + ik/2R(z)]\} \qquad (2.2.2)$$

where the following parameters have been used

$$w^2(z) = w_0^2[1 + (z/z_0)^2] \qquad (2.2.3)$$

$$R(z) = z[1 + (z_0/z)^2] \qquad (2.2.4)$$

$$\theta(z) = \tan^{-1}(z/z_0) \tag{2.2.5}$$

$$z_0 = \frac{\pi w_0^2}{\lambda} \tag{2.2.6}$$

The coefficient of the r^0 term describes the phase variation compared to the plane wave solution. Of more interest is the coefficient of the r^2 term. This coefficient can be rewritten as $ik/2q(z)$, yielding

$$\frac{1}{q(z)} = \frac{1}{R(z)} - \frac{i\lambda}{\pi w^2(z)} \tag{2.2.7}$$

where $k = 2\pi/\lambda$ has been used. This is called the fundamental Gaussian beam solution in terms of which the propagating beam can be described. The first term can be identified with the spherical wave front radius which evolves according to equation (2.2.4). Noting that the second term in the above equation is the only real term in equation (2.2.2) enables the intensity profile to be written down as

$$I(r) = I(0)\exp\left(-\frac{2r^2}{w^2}\right) \tag{2.2.8}$$

From this it is apparent that w can be used to define a beam spot size, since at $r = w$ the beam intensity has fallen to $1/e^2$ of its on axis value. The beam can therefore be considered to be contained within the area defined by the spot size radius, w. The spot size radius evolves according to equation (2.2.3) and is illustrated in Figure 2.2. Of particular interest is the value of the beam radius $w(z = 0) = w_0$ which is the minimum spot size of the beam. This is called the beam waist radius and it is located in the focal plane of the beam.

The quantity z_0 defined by equation (2.2.6) is known as the Rayleigh range and is illustrated in Figure 2.2. This defines the distance from the beam waist at which the beam area has doubled, i.e. $w(z = z_0) = \sqrt{2}\, w_0$. Twice this distance is called the beam confocal parameter which defines the extent of the waist region.

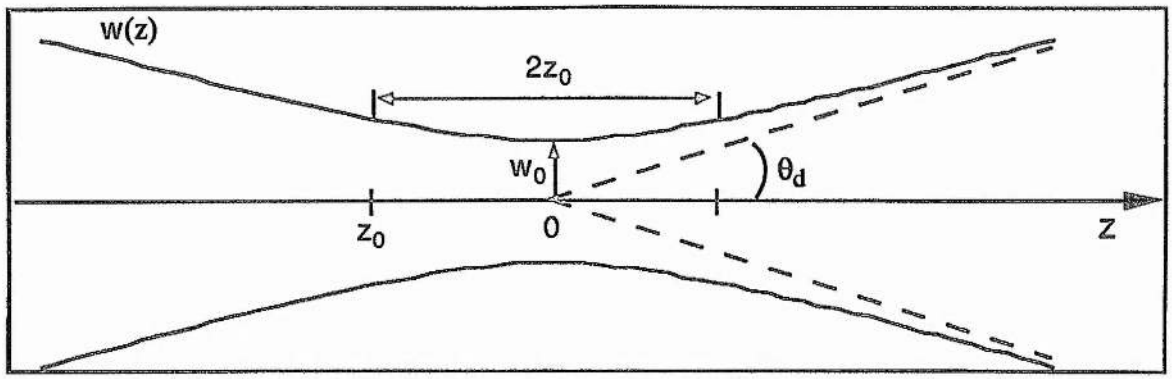

Figure 2.2 Showing the evolution of the beam spot radius of a Gaussian beam for propagation along the z-axis.

The final parameter of importance concerning propagation of Gaussian beams is the beam divergence, θ_d. This quantifies the divergence of the beam and is the half-cone angle of the cone to which the propagating beam radius is asymptotic. From Figure 2.2 it is apparent that in the far field, i.e. $z >> z_0$, the divergence angle is given by

$$\theta_d = \tan^{-1}\left(\frac{w(z)}{z}\right) \approx \tan^{-1}\left(\frac{w_0}{z_0}\right) \cong \frac{\lambda}{\pi w_0} \qquad (2.2.9)$$

This is the ideal divergence for a fundamental Gaussian beam. Beams of higher order Gaussian modes will be characterised by a larger far field divergence. Beams which propagate with the divergence expected for a fundamental Gaussian beam are said to exhibit diffraction limited propagation. This will be considered following the discussion on focusing of Gaussian beams.

<u>Focused Gaussian Beams</u>

Consider a Gaussian beam of divergence θ_d and initial waist w_0 which is incident on a lens of focal length f. If the beam radius at the lens is $\overline{w}$, then the new beam waist radius at the focus is given by

$$w_0' = \frac{\lambda}{\pi}\left[\theta_d^2 + \left(\frac{\overline{w}}{f}\right)^2 - \frac{2\lambda}{f\pi}\sqrt{\left(\frac{\overline{w}}{w_0}\right)^2 - 1}\right]^{-1/2} \qquad (2.2.10)$$

and is located a distance f from the lens. If the lens is placed in the near field where $\overline{w} \cong w_0$ then the new waist is still located a distance f from the lens and is given by

$$w_0' = f\theta_d \Big/ \sqrt{\left(\frac{f\theta_d}{w_0}\right)^2 + 1} \qquad (2.2.11)$$

A more surprising result is obtained by considering the case when the lens is located a distance f from the initial waist. This situation is illustrated in Figure 2.3. Then substituting equation (2.2.3) into equation (2.2.10) yields for the new waist

$$w_0' = \frac{\lambda f}{\pi w_0} = f\theta_d \qquad (2.2.12)$$

The surprising result is that the new waist is again to be found a distance f from the lens. This is contrary to geometric optics where this arrangement would result in a collimated beam focused at infinity.

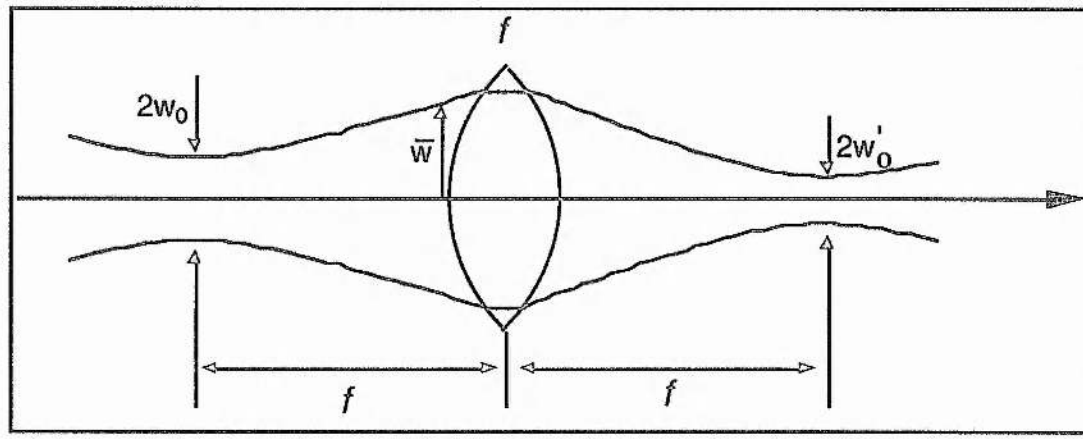

Figure 2.3: Illustrating the interesting property of Gaussian beam propagation through a lens located one focal length away from the initial waist. The new waist is found to occur a distance of one focal length away from the lens.

Real beams and beam quality

As alluded to earlier, real laser beams are rarely of a purely fundamental Gaussian nature. This can be attributed to diffraction at apertures like those introduced by the insertion of the active medium. Hence the earlier term, diffraction limited, for beams propagating divergence given by equation (2.2.9). The gain in the active medium itself will introduce distortion from

the expected empty cavity analysis. It is therefore important to consider higher order solutions to the wave equation, solutions which exhibit fluctuations in the transverse distribution of the fields. Fortunately, though, it turns out that all the propagation equations presented earlier are still valid provided all the beam radius parameters w are replaced by W/M where by convention the capital W represents beam radii of higher order modes. The M factors represent the departure of these fields from the fundamental Gaussian solution. This also enables a procedure for evaluating the quality of real beams to be implemented. Consider the equivalent of equation (2.2.12) for higher order beams

$$M^2 = \frac{\pi W_0 W_0'}{\lambda f} = \frac{\theta_g}{\theta_d} \qquad (2.2.13)$$

where the definition

$$\theta_g = \frac{W_0'}{f} \qquad (2.2.14)$$

has been made. This represents the actual divergence of the beam. The M^2 factor is therefore the ratio of the actual divergence of the beam to the expected divergence of a fundamental Gaussian beam of waist radius W_0'. As such, M^2 quantifies the departure from diffraction limited propagation for a given laser beam. From this discussion a method for measuring the M^2 factor should be clear. First a waist, W_0, should be created and accurately measured. A lens should then be placed one focal length away from this waist. Measurement of the beam radius in the focal plane of the lens then gives W_0' (not necessarily the waist radius) and thus equation (2.2.13) can be evaluated.

2.2.2 Resonator design

It is now prudent to consider the design of optical resonators which will support Gaussian beams. As mentioned earlier, the azimuthal symmetry of the major components used to construct these resonators result in Gaussian waves. To begin with only very simple resonators consisting of only two curved mirrors will be considered. The results for these simple resonators will prove to apply to more complicated designs which can often be

reduced to much simpler equivalents. The frequency selective properties of optical resonators will also be considered as well as their stability.

The basic resonator and stability

The results of the most basic resonator, consisting only of two mirrors of radius of curvature R_1 and R_2 separated by an optical length L, are well known[19]. A stable cavity is defined as an optical resonator which supports a low-loss, self-replicating mode. Such modes supported by a resonator are termed eigenmodes. The stability of the above simple resonator is discussed in terms of the parameters

$$g_i = 1 - \frac{L}{R_i} \qquad (2.2.15)$$

The ability of a resonator to support a low-loss, self-replicating mode translates into the following condition being satisfied,

$$0 < g_1 g_2 < 1 \qquad (2.2.16)$$

The beam radii of an eigenmode at the mirrors of a stable resonator can be written in terms of these parameters[20], yielding

$$w_1^2 = \left(\frac{\lambda L}{\pi}\right)\sqrt{\frac{g_2/g_1}{1-g_1 g_2}}, \qquad \frac{w_2^2}{w_1^2} = \frac{g_1}{g_2} \qquad (2.2.17)$$

The beam waist is given by

$$w_0^2 = \left(\frac{\lambda}{\pi}\right)\frac{\sqrt{L(R_1-L)(R_2-L)(R_1+R_2-L)}}{R_1+R_2-2L} \qquad (2.2.18)$$

which is located at distances

$$t_1 = \frac{L(R_2-L)}{R_1+R_2-2L}, \qquad t_2 = \frac{L(R_1-L)}{R_1+R_2-2L} \qquad (2.2.19)$$

from the R_1 and R_2 mirrors, respectively.

Resonators with an internal lens

This case has been discussed in depth in reference[20]. Its usefulness lies in the fact that folded resonators can be unfolded and reduced to cavities of this form. With the definition:

$$g_i = 1 - \frac{L_j}{f} - \frac{L_0}{R_i} \qquad (2.2.20)$$

where $L_0 = L_1 + L_2 - L_1 L_2 / f$, it can be shown that the usual stability condition given by equation (2.2.16) is still applicable. The beam radii at the mirrors are still given by the previous expression, i.e. equation (2.2.17), with L replaced by L_0. The beam waist in each arm of the cavity may be found by constructing the equivalent two mirror cavity such that the previous results, i.e. equations (2.2.18) and (2.2.19), apply. Using the usual geometric optics imaging rules, one of the mirrors may be imaged through the lens so that the equivalent simple resonator is formed[20], as illustrated in Figure 2.4.

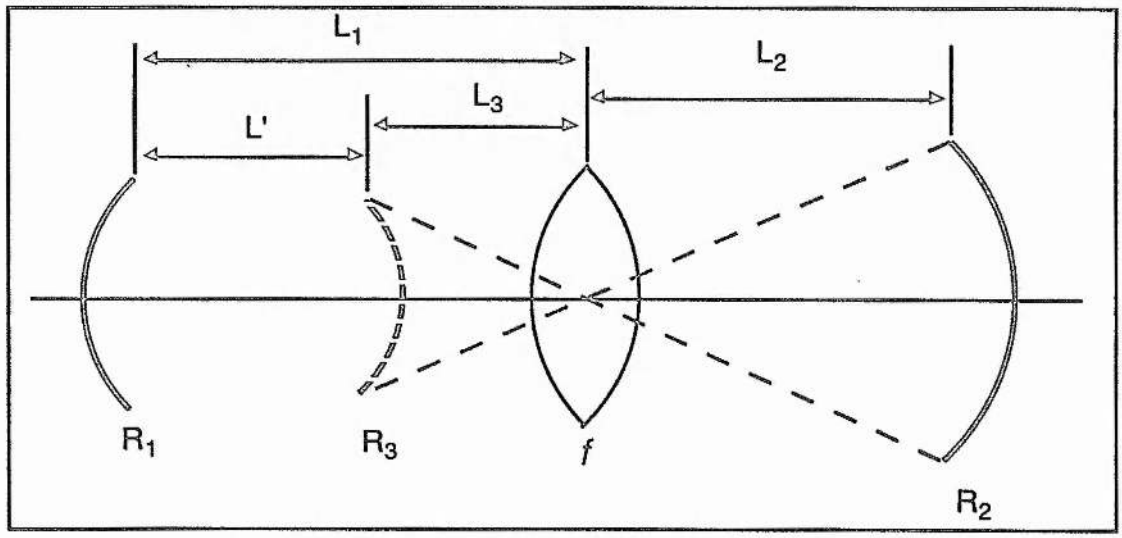

Figure 2.4 Illustrates the construction of the equivalent simple resonator from a resonator containing a thin lens of focal length f

For a thin lens of focal length f, the imaging rules yield the length, L', and the radius of curvature, R_3, for the imaged lens forming the equivalent resonator. The explicit expressions for the imaged mirror radius of curvature and the new length of the equivalent resonator are:

$$R_3 = \frac{f^2}{(f - L_2)\left(\frac{f - L_2}{R_2} - 1\right)} \qquad (2.2.21)$$

and

$$L' = L_1 + \frac{L_2 f}{L_2 - f} \qquad (2.2.22)$$

These can be used to define stability parameters (using equation (2.2.15)) which can be used as before.

Stability sensitivity and cavity design

This is not to be confused with stability, which refers to the existence of low loss modes within the resonator. Resonator sensitivity refers to the variation in mode size and location in response to mechanical or optical perturbations. Sensitivity to axial perturbations will be discussed here. Mirror tilt sensitivity is discussed elsewhere[21,22]. It has been shown by Steffen et al.[23] that resonators which are most insensitive to axial perturbations are those which roughly satisfy the condition

$$g_1 g_2 = \frac{1}{2} \qquad (2.2.23)$$

This type of insensitivity is equivalent to that arising from the presence of a fluctuating thermal lens in the laser medium[23].

A complementary approach to the sensitivity problem is found by considering explicitly the stability range of a particular cavity. The case of the simple trioptic cavity depicted in Figure 2.4 is once again considered. The stability range can be determined by considering a small variation, δ, in the length of one of the arms[24]

$$L_1 = R_1 + f + \delta \qquad (2.2.24)$$

which is then substituted into the stability condition given by equation (2.2.16) to yield maximum and minimum values for the length variation. These are found to be

$$\delta_{\min} = \frac{f^2}{L_2 - R_2 - f}, \qquad \delta_{\max} = \frac{f^2}{L_2 - f} \qquad (2.2.25)$$

which enables a stability range to be defined as

$$2S = \delta_{\max} - \delta_{\min} \qquad (2.2.26)$$

The beam waist and its location can now be written in terms of these quantities, yielding:

$$z_{10}^2 = \left| \frac{(R_1 + \delta - \delta_{max})(R_1 + \delta - \delta_{min})(\delta - \delta_{max})(\delta - \delta_{min})}{(R_1 + 2\delta - \delta_{min} - \delta_{max})^2} \right| \qquad (2.2.27)$$

and

$$t_1 = \frac{(R_1 + \delta - \delta_{max})(R_1 + \delta - \delta_{min})}{(R_1 + 2\delta - \delta_{min} - \delta_{max})} \qquad (2.2.28)$$

Where z_{10} is the Rayleigh range of the mode. It is interesting to consider this solution for the case of a plane parallel resonator containing an internal lens. As shown below this corresponds to the type of resonator considered here. In this case the Rayleigh range in terms of the length perturbation is given by

$$z_{10}^2 = \left| (\delta - \delta_{max})(\delta - \delta_{min}) \right| \qquad (2.2.29)$$

where $\delta_{min} = 0$ from equation (2.2.25).

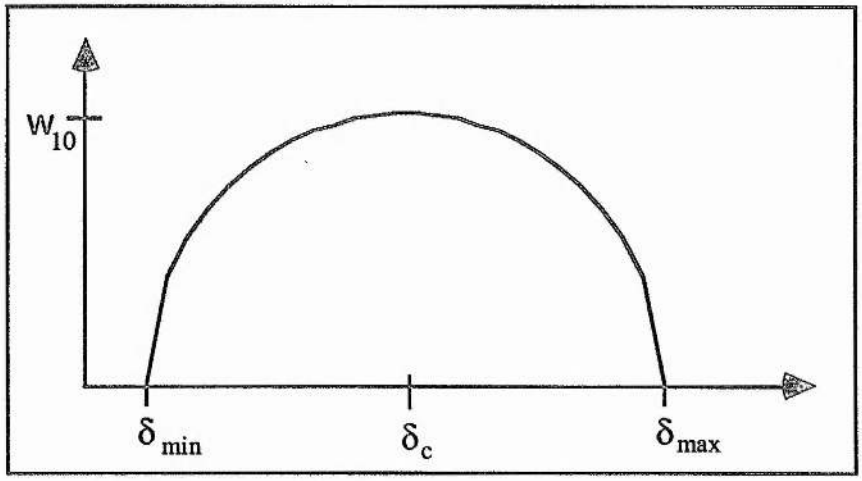

Figure 2.5: Illustrates the variation over the stability range of the beam waist, w_{10}, with small variations, δ, in the separation of one of the mirrors and the internal lens, L_1.

From equation (2.2.28) it is clear that the waist is located at the surface of the plane mirror, as expected. The beam waist as a function of the cavity length adjustment, δ, for this case is plotted in Figure 2.5, where a 'flat' insensitive region is evident at the centre of the stability region. Recalling from above that resonators most insensitive to cavity length variations are those satisfying equation (2.2.23) implies that such resonators have large stability ranges as defined by equation (2.2.26).

Multi-element cavities

In this section resonators consisting of many mirrors are shown to have equivalent two-mirror forms. Thus all the previously presented results concerning resonator stability and sensitivity will be applicable.

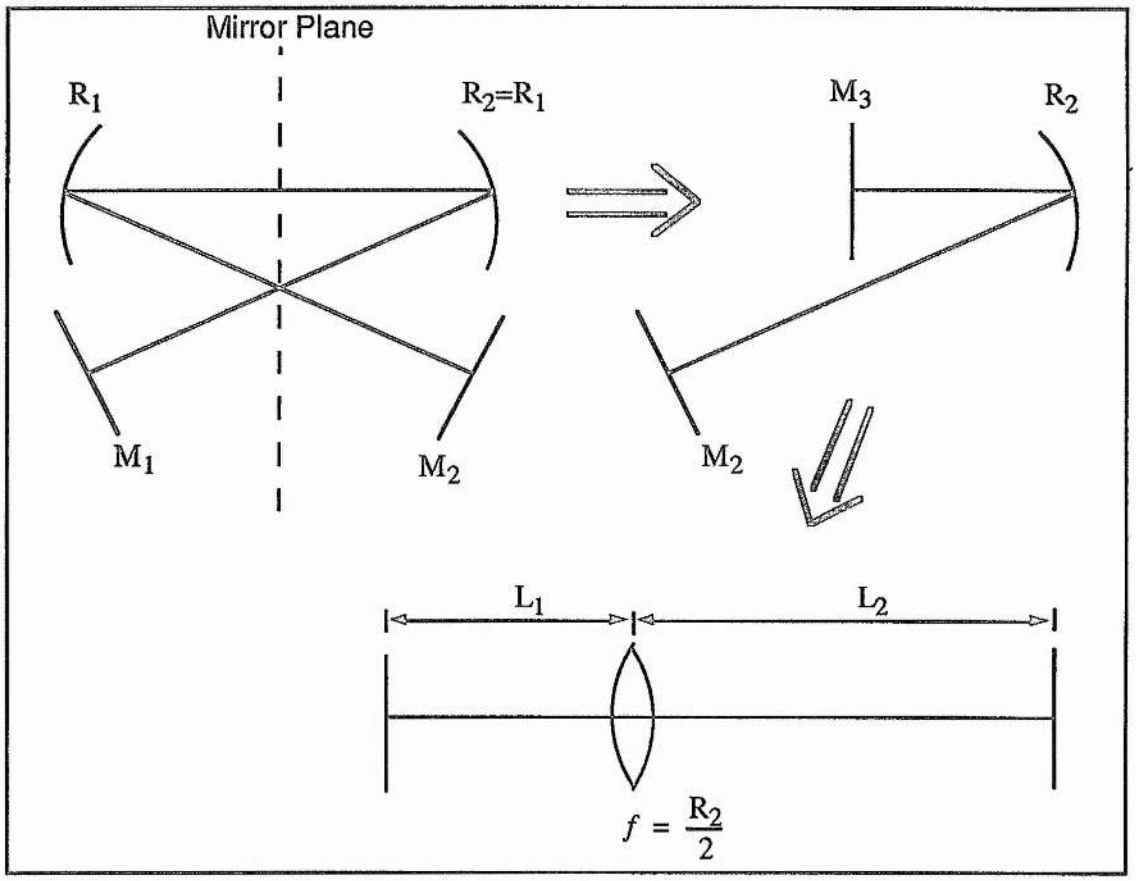

Figure 2.6 Illustrates the equivalence of an X-cavity to a plane parallel cavity with an internal lens. This was shown earlier to have an equivalent two mirror form.

Cavities such as X-cavities (or four-mirror folded cavity) are well known for their insensitivity to perturbations of both length and focal power of an internal thermal lens. As illustrated in Figure 2.6 these X-cavities can be shown by mirror symmetry to be equivalent to a folded three-mirror cavity which is itself equivalent to a plane parallel resonator with an internal lens. The various waist radii can therefore be calculated as before.

The results of the previous section can now be used to design a stable resonator with a given waist radius in one of the arms. The waist radius will in general be determined by threshold

considerations discussed in section (2.1.5). The maximum beam waist radius for a given plane parallel cavity with internal lens is found at the centre of the stability region, $\delta_c = 2S/2$ as defined by equation (2.2.26). For the above cavity which has been shown to be equivalent to an X-cavity, the maximum beam waist radius is given by

$$w_{10\max} = f\sqrt{\frac{\lambda}{2\pi}\frac{1}{L_2 - f}} \text{ , and } L_1 = f + \delta_c \qquad (2.2.30)$$

Thus for curved mirrors of known radius $2f = R_1 = R_2$, the lengths of the cavity arms can be calculated. In this way a stable resonator may be constructed to yield the desired beam waist radius.

Astigmatism in resonators

It should be noted that folded resonators as described above lead to beam astigmatism, that is, the beam has different divergence properties in different planes. Brewster angled intracavity elements have a similar effect. The relevant results required to compensate for the astigmatism produced in folded cavities or cavities containing tilted surfaces (e.g. Brewster cut elements), are presented in this section[24,25]. In the case of a tilted mirror, the rays in the sagittal plane ($\vec{E}\perp$ plane of incidence) and those in the tangential plane ($\vec{E}\parallel$ plane of incidence) will experience different focusing strengths. The effective focal length of the mirror in each plane is given by[24]

$$f_\perp = f/\cos\vartheta \ , \qquad f_\parallel = f\cos\vartheta \qquad (2.2.31)$$

where ϑ is the angle of incidence relative to the normal of the reflecting surface. In the case of a Brewster angled cell of thickness d (through the centre of the cell), and refractive index n, the different effect on the sagittal and tangential bundles can be expressed by different effective distances through the cell. These are given by[25].

$$d_\perp = d\sqrt{n^2-1}/n^2 \ , \qquad d_\parallel = d\sqrt{n^2-1}/n^4 \qquad (2.2.32)$$

For a cavity with astigmatism caused by either one or both of the above elements, there will be two separate stability ranges according to equation (2.2.26) and hence there will be different modes in each plane. The purpose of astigmatic compensation is to produce a

maximum overlap of these two stability ranges so that the congruence between the modes in each plane is maximised. Astigmatic compensation is achieved when the relationship

$$2d\left(n^2-1\right)\sqrt{n^2+1}/n^4 = 2f\sin\vartheta\tan\vartheta \qquad (2.2.33)$$

is satisfied.

Frequency selection

The laser resonator is important not only for defining the spatial propagation mode, but also for defining the spectral properties of the output radiation. For simplicity the discussion here of the spectral selection characteristics of optical resonators will be restricted to the case of a plane parallel Fabry-Perot resonator. The most important feature of the resonator is that only certain discrete frequencies are permitted within the cavity. In general the allowed TEM_{mnq} modes within a resonator are separated in frequency by[21]

$$\Delta\nu = \left(\frac{c}{2L}\right)\left[\Delta q + \left(\frac{1}{\pi}\right)\Delta(m+n)\cos^{-1}\left(1-\frac{L}{R}\right)\right] \qquad (2.2.34)$$

where the Δq term describes the longitudinal frequency spacing and the $\Delta(m+n)$ term describes the spacing in frequency of the transverse modes in Cartesian co-ordinates. Further simplification is attained by considering only fundamental Gaussian solutions and hence disregarding transverse modes. In this case the frequency separation of successive axial modes is given by

$$\Delta\nu = \left(\frac{c}{2L}\right) \qquad (2.2.35)$$

This corresponds to the free spectral range of a Fabry-Perot etalon. Basically this implies that only a discrete set of frequencies, separated in frequency by that in equation (2.2.35), will be supported by the resonator.

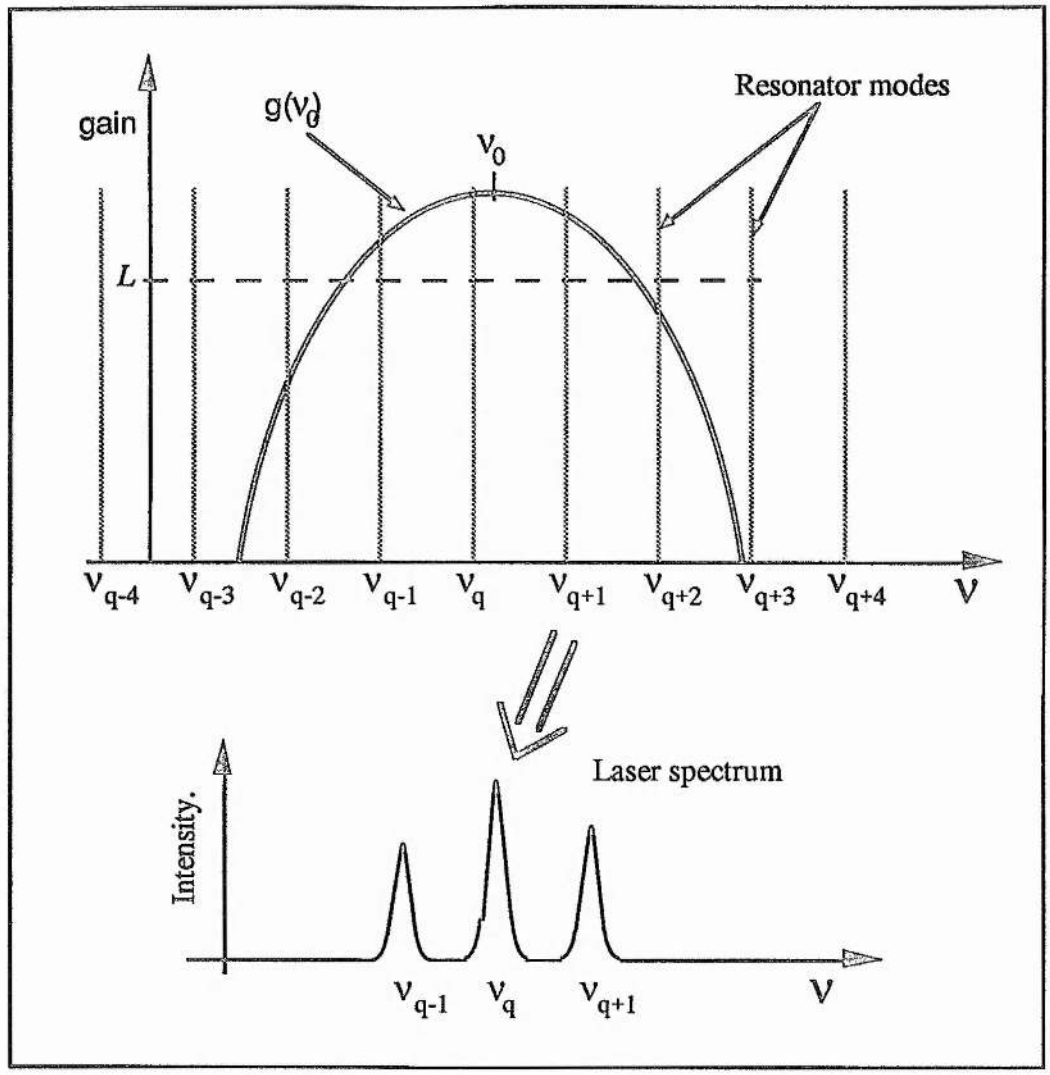

Figure 2.7 Depicts the interaction of the allowed resonator modes with the above threshold gain which selects the output laser spectrum.

In general the frequency range over which gain is available is finite and depends on the detail of the gain medium itself. As was discussed earlier, the gain bandwidth can be described in terms of a lineshape function so that the output frequencies will in general be obtained by considering the convolution of the allowed resonator frequencies with the gain bandwidth function (see equation (2.1.15)). Provided a given mode, falling under the gain curve, is above threshold laser output at that frequency will result. This is depicted in Figure 2.7.

In many lasers systems attempts are made to limit the number of axial modes so that oscillation over only a single cavity resonance is achieved. This is termed single-frequency operation of the laser. If this situation is achieved, the linewidth of the single-frequency

output $\Delta\nu$, will generally be much smaller than that of the passive resonator $\Delta\nu_c$. The theoretical lower limit, $\Delta\nu_L$, for the linewidth of a single-frequency laser is given by the Schawlow-Townes limit. This can be written as the passive resonator linewidth divided by the number of photons in the resonator:

$$\Delta\nu_L = \frac{\Delta\nu_c}{\phi V} \qquad (2.2.36)$$

where ϕV is the number of photons in the laser mode volume. For a single-frequency laser well above threshold, this is seen to imply an output linewidth which is very much less than the passive resonator linewidth.

Spatial hole burning and single-frequency operation

Various methods can be utilised in order to achieve single-frequency operation. Most are applied to lasers in which spatial hole burning has been reduced or even eliminated. Spatial hole burning is associated with standing-wave oscillators. A standing-wave oscillator operating at a single frequency will set up a spatial standing-wave intensity distribution in the gain medium. This will result in a the population inversion being saturated at the peaks of the spatial intensity pattern, while there will be no reduction of the inversion at the nodes. It is therefore possible for a different frequency to become resonant provided its standing-wave intensity peaks reside in the undepleted regions of the medium. For this reason, multimode operation due to spatial hole burning may be reduced by locating the gain medium at one of the ends of the laser cavity[26]. Spatial hole burning may be eliminated altogether by achieving unidirectional operation of a ring-laser cavity. In the case of a travelling-wave oscillator, the intensity distribution within the cavity is spatially uniform, enabling a single frequency to saturate the entire active volume.

Once spatial hole burning has been eliminated it becomes easier to attain single-frequency operation. The simplest method for reducing the number of laser modes in operation is by interferometric mode control. This technique involves the insertion of various types of devices into the laser cavity. These devices work in a common way in that they are resonant at discrete frequencies whilst simultaneously discriminating against intermediate frequencies.

Common examples are Fabry-Perot etalons and birefringent filters. An etalon can be described as a frequency filter, allowing only a discrete set of frequencies to pass with high transmission. By suitably matching the free spectral range of an etalon to that of the laser resonator, only a single mode may be selected from under the gain curve. A birefringent filter applies variable polarisation rotation as a function of frequency. If used in conjunction with intracavity Brewster surfaces, this will provide preferential transmission for a narrow frequency band. By rotating the filter, the frequency experiencing low loss may be varied. In this form it is known as a birefringent tuner and is useful for wavelength selection in vibronic media.

Unfortunately by their very nature these interferometric techniques are lossy and so reduce the efficiency of the system. A much more reliable and efficient technique for obtaining single-frequency operation is known as injection seeding. In this case a low power single-frequency source is injected into the laser cavity. This injected signal will force the laser to operate on only the nearest modes allowed by the resonator. This technique will be considered in more detail in a following section.

2.3 Q-switching theory

In this section the cavity rate equation formalism developed earlier will be used to derive equations which will be useful in modelling the performance of lasers under the Q-switch mode of operation. Separate theoretical models for the cases of optimised and non-optimised output coupling will be constructed. It will be shown that the same theory can be applied to gain-switched systems.

2.3.1 General Q-switching theory

A description of Q-switching begins with the cavity rate equations (2.1.26) and (2.1.27). During the pumping cycle the cavity Q is held low by ensuring that the losses are high enough so that the oscillation condition is never satisfied. Therefore in the low Q cavity there will be no circulating field, $\phi = 0$, for the duration of the pumping cycle, so that the build-up of the population inversion is described by

$$\frac{dn_2}{dt} = W_p n_0 - \frac{n_2}{\tau_f} \qquad (2.3.1)$$

which can be solved to yield equation (2.1.47) for the population inversion density at the end of the pump cycle. However, with the assumption that initially little of the population inversion is lost during pumping such that when the losses are suddenly reduced by switching the cavity Q to a much higher value, then the gain of the system is described by the small signal or unsaturated gain of equation (2.1.36). The correction for the assumption of no population inversion loss during the pump cycle can be made by including the storage efficiency factor in this analysis. It should be noted that a further assumption of instantaneous switching of the cavity Q has been made. Consider now the build-up of the circulating radiation density which is assumed to start from some small initial value usually provided by spontaneous noise. A very large circulating field as described by equation (2.1.26) together with the substitution of equation (2.1.30), that is

$$\frac{d\phi}{dt'} = \phi\left(\frac{n_2}{n_{th}} - 1\right) \qquad (2.3.2)$$

will rapidly build-up and a single short pulse will be emitted. Notice that a dimensionless time variable $t' = t/\tau_c$ has been defined. The equation describing the decrease in the population inversion density is obtained from equation (2.1.27) without pumping and where the effect of the circulating radiation is assumed to be the dominant factor in reducing the inversion density. The relevant equation becomes

$$\frac{dn_2}{dt'} = -\phi \frac{l'}{l} \frac{n_2}{n_{th}} \qquad (2.3.3)$$

where the above defined dimensionless time variable has again been used and equation (2.1.30) has also been substituted. Time can now be eliminated by dividing equation (2.3.2) by (2.3.3), yielding

$$\frac{d\phi}{dn_2} = \frac{l}{l'}\left(\frac{n_{th}}{n_2} - 1\right) \qquad (2.3.4)$$

This can be integrated with the initial conditions that there is no circulating photon density $\phi_i = 0$ and that the initial population inversion density is given by equation (2.1.53), i.e.

$$n_i = \eta_{st} \frac{K' E_{in}}{\sigma_{21} l} \tag{2.3.5}$$

where $g_0 = \sigma_{21} n_2$ has been used and the energy storage efficiency factor η_{st}, as defined by equation (2.1.48) in section (2.1.4), has been included. Integration from these initial conditions to some arbitrary time later yields the solution

$$\phi(t) = \frac{l}{l'}\left[n_{th} \ln \frac{n_2(t)}{n_i} - \left(n_2(t) - n_i\right) \right] \tag{2.3.6}$$

The maximum photon density is easily shown to occur when $n_2(t) = n_{th}$, and is given by

$$\phi_{\max} = \frac{l}{l'}\left[n_{th} \ln \frac{n_{th}}{n_i} - \left(n_{th} - n_i\right) \right] \tag{2.3.7}$$

A few points are worth noting here. The population inversion is seen to decrease from its initial value given by equation (2.3.5) due to the build-up of the circulating photon density. The above analysis implies that the photon density $\phi(t)$ will begin to decay away after reaching the above maximum when $n_2(t) = n_{th}$. However, the presence of the circulating field will be able to stimulate further emission thus driving the population inversion well below its threshold level. In this way it is clear that the decay of the circulating intensity is not merely given by the cavity decay constant.

Output quantities

The output power in the Q-switch pulse can be written down with the help of equation (2.1.40). The maximum output power is given by

$$P_{\max} = \frac{Alh\nu}{t_R} \ln\left(\frac{1}{R}\right)\left[n_{th} \ln \frac{n_{th}}{n_i} - \left(n_{th} - n_i\right) \right] \tag{2.3.8}$$

Now integrating the output power over time from zero to infinity will give the energy in the Q-switched pulse

$$E = \frac{Al'h\nu}{t_R} \ln\left(\frac{1}{R}\right) \int_0^\infty \phi(t) dt \tag{2.3.9}$$

Making use of equation (2.3.3) to change the variable of integration to population inversion and integrating from the initial population inversion n_i to some final population inversion n_f yields

$$E = \frac{Ah\nu}{2\sigma_{21}} \ln\left(\frac{1}{R}\right) \ln\left(\frac{n_i}{n_f}\right) \qquad (2.3.10)$$

for the energy in a Q-switch pulse. Recalling that l' is the optical length of the resonator and l is the length of the active medium, it is seen from the above that the extracted energy is independent of cavity length while the output power depends explicitly on the cavity length as expected.

In order to extract useful answers from equation (2.3.10) for the extracted energy, the final population inversion level will need to be determined. This can be obtained by evaluating equation (2.3.6) at a time after the end of the Q-switch pulse. At this time the population inversion will have reached its final level and there will be no circulating power in the cavity. The solution is given by

$$\ln\frac{n_i}{n_f} = \frac{\left(n_i - n_f\right)}{n_{th}} \qquad (2.3.11)$$

This is a transcendental equation which can be easily solved graphically or numerically. This equation can be solved by iteration. Making the substitutions $u_i = n_f/n_{th}$ and $y = n_i/n_{th}$ enables the above equation to be rewritten in iterative form, yielding

$$y_{i+1} = u\exp(y_i - u) \qquad (2.3.12)$$

For a small final population inversion and a large initial population inversion a reasonable first choice is $y_1 = 0$. After a few iterations this will result in the determination of the final population inversion density.

The final characteristic of the Q-switched pulse which is of interest is the pulse duration. If the pulse is assumed to be approximated by an asymmetric triangle, as represented in Figure 2.8 then it becomes a simple matter to estimate the pulse duration.

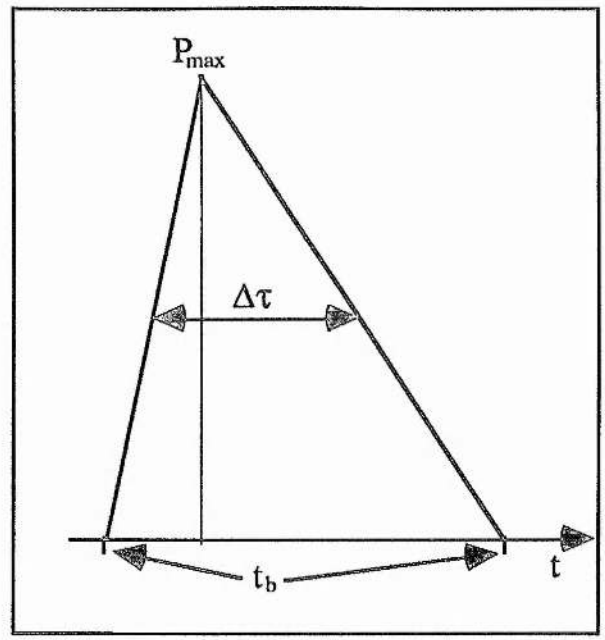

Figure 2.8 Illustrating the asymmetric approximation of a Q-switched pulse. The area under the curve is the total pulse energy.

Since the area under the triangle is just the pulse energy we can write for the FWHM pulse duration

$$\Delta\tau = \frac{t_b}{2} = \frac{E}{P_{\max}} = \tau_c \frac{n_i - n_f}{n_{th} \ln \frac{n_{th}}{n_i} - (n_{th} - n_i)} \qquad (2.3.13)$$

where equations (2.3.11) and (2.1.30) have been used for the threshold inversion.

2.3.2 Optimised Q-switching performance

The above equations for the Q-switched performance of a laser can be greatly simplified for the case of an optimally coupled laser. The equations are much more useful to the laser engineer in this form since they are expressed in terms of a single variable which represents the ratio of the small signal gain to the spurious internal losses. This variable is easily determined or estimated for diode-pumped lasers and can be used to determine the required output coupling necessary to optimise Q-switch performance. This optimally coupled theory was first derived by Degnan[27] using the method of Lagrange multipliers. Alternatively this optimisation is easily obtained by maximising the output energy expression of equation

(2.3.10) with respect to the output coupling. Since the logarithmic factor in equation (2.3.11), which appears in the energy expression, also depends on the output coupling through the threshold inversion density, the optimisation amounts to requiring that

$$\frac{d}{dy}\left\{\left(\frac{g}{y}-L\right)(y-u)\right\}=0 \qquad (2.3.14)$$

is solved. Where the substitutions: $g=2g_0l$, $y=n_i/n_{th}$ and $y=n_f/n_{th}$ have been made and the logarithmic factor has been replaced using equation (2.3.11). Differentiation results in the optimisation requirement becoming that

$$\frac{(y-u)}{y}\left[\frac{1}{(1-u)}\left(\frac{g}{y}-L\right)-\frac{g}{y}\right]=0 \qquad (2.3.15)$$

is satisfied. There are two possibilities. The first solution is that

$$y=u \Rightarrow n_i=n_f \qquad (2.3.16)$$

which is the trivial solution representing the minimum result of no lasing. The second possibility gives the maximised output result. This is achieved by setting the square brackets equal to zero which results in the maximum condition when

$$\frac{y}{u}=\frac{g}{L} \Rightarrow \frac{n_i}{n_f}=\frac{2g_0l}{L} \qquad (2.3.17)$$

Substitution into equation (2.3.11) and noticing that

$$y=\frac{n_i}{n_{th}}=\frac{2g_0l}{\ln\frac{1}{R}+L} \qquad (2.3.18)$$

enables the optimised output coupling to be determined. For a given laser with known losses and known pumping level (i.e. known initial population inversion) the optimum output coupling for Q-switched operation and the optimised output quantities can be expressed in terms of these parameters via the dimensionless optimisation parameter

$$z=\frac{n_i}{n_f}=\frac{2g_0l}{L}=\frac{2\eta_{st}K'E_{in}}{L} \qquad (2.3.19)$$

which is just the ratio of the small-signal gain factor to the parasitic loss factor. This factor depends only on the pump factor K' and the intracavity parasitic losses L which can be obtained by the technique proposed by *Findlay and Clay* [15] as outlined in section (2.1.5). The optimised output coupling is found to be

$$R_{opt} = \exp\left\{-L\left(\frac{z-1-\ln z}{\ln z}\right)\right\} \tag{2.3.20}$$

With the output coupler so optimised, the maximised output energy is given by

$$E = \frac{AhvL}{2\sigma_{21}}[z-1-\ln z] \tag{2.3.21}$$

and the FWHM duration of the optimised pulse is found to be

$$\Delta\tau_{opt} = \frac{t_R}{L}\left(\frac{\ln z}{z}\right)\left[1-\left(\frac{z-1}{z\ln z}\right)\left(1-\ln\left(\frac{z-1}{z\ln z}\right)\right)\right]^{-1} \tag{2.3.22}$$

For a given laser set-up we have therefore determined, with the above analysis, Q-switched performance has been maximised with respect to energy extraction. The analysis could also be performed for optimimum pulse duration. The optimised Q-switched performance as a function of the material parameters will be discussed in chapter 3. It is now time to move on and examine some of the details when implementing active Q-switching of a laser.

2.3.3 Prelasing and postlasing

The system of Q-switching implemented in the lasers considered here is that of electro-optic Q-switching. The particular intricacies of implementing the Q-switching will not be discussed here, but will be left to the relevant experimental chapters. It is worth noting however, how these techniques work so that problems that were later encountered can be understood. Basically, electro-optic Q-switching requires an intracavity crystal which exhibits optical birefringence upon the application of an external electric field to the crystal. In order to successfully utilise this technique it is also necessary that the laser have a well defined polarisation. The electro-optic crystal can then be used in conjunction with a polariser to act as an optical shutter. When the crystal has no voltage placed across it, the laser operates with a well defined linear polarisation defined by the polariser. When a voltage is applied across

the crystal, it becomes birefringent and the polarisation of the light passing through it is changed. The level of birefringence and hence the change in the polarisation of the transmitted light is determined by the magnitude of the applied voltage. It should be noted that the crystal will have a double effect on the polarisation of the laser field in a round trip of the resonator. When the light of changed polarisation is incident on the polariser, it will in general experience a degree of loss. In this way, by changing the voltage applied to the crystal, the cavity Q is made to change and can be made low enough such that the laser cannot reach threshold and so laser action does not take place. Q-switching is then achieved by rapidly turning the applied voltage off so that the cavity returns to its high Q state and a giant pulse is emitted.

It is in this switching process where most of the possible problems can arise. Firstly, in very high gain systems it may not be possible to achieve holdoff of laser action when the appropriate voltage is applied. This may be just a architectural problem which may be overcome with a different implementation of the technique. This situation where laser action breaks through just before the pumping cycle is complete and the cavity is Q-switched is termed prelasing and can have serious consequences. In this scenario the Q-switched pulse will be "seeded", possibly only in a small region of the laser rod while the rest of the gain will still have to build up from noise. The seeded portion will develop much more swiftly, resulting in very high powers in that small section of the rod which could therefore lead to damage.

A second practical problem which may arise is that secondary pulses may occur after the appearance of the main Q-switched pulse. This phenomenon is termed postlasing. Postlasing is associated with piezooptic effects in the crystal. As well as having an electrooptic response to applied external fields, these crystals will often also have an associated piezoelectric response. This will result in the crystal being compressed under the influence of an applied voltage. When the voltage is removed, the crystal will relax back to its original size in a finite time. There will be an added birefringence associated with the compression so that during the slow decompression of the crystal after removal of the voltage the stress-induced birefringence will also slowly decay away. This will therefore have dynamic effect on the

cavity losses. Because this decrease in the birefringence occurs on a 100ns time scale, it is possible that the main Q-switch pulse has been emitted before the cavity has returned to its lowest loss state. It is feasible then that when the cavity loss has decayed back to its lowest loss state, there is sufficient gain for a secondary pulse to be emitted.

2.3.4 Gain-switching

As was mentioned when the storage efficiency factor was discussed in section (2.1.4), the limiting case of a pump pulse of extremely short duration compared to the upper state lifetime of the medium represents the optimum Q-switching condition. If the laser is pumped so that it is far above threshold before laser oscillation has built up, the output will be of the form of relaxation oscillations. This is termed gain-switching. Even for very low loss cavities, it takes a finite period for the laser field to build-up from noise before an output is emitted. If the pump cycle is sufficiently short compared to the build-up time of the laser output then the gain will not be replenished after the first laser pulse has driven the population inversion well below threshold, and so only a single pulse is emitted. There will be no need to change the losses of the cavity in order to achieve a Q-switched pulse. It is therefore a misnomer to call the process Q-switching. To achieve a single gain-switched pulse the pumping process has to be so swift that it is as if the gain has instantaneously been turned on. As mentioned before, the storage efficiency is unity under gain-switching. The theoretical approach is identical to that of Q-switching and all the results hold.

However, a little more care is required in this situation when the pump threshold is considered. In the derivation of the Q-switching equations, the effect of the upper state lifetime was ignored. For any system operating well above threshold the build-up time is very short compared to the upper state lifetime and this approximation is valid. If, however, the gain switched system is operated near threshold then the build-up time for the oscillation field can become comparable to the upper state lifetime of the medium and it is no longer reasonable to neglect the decrease in the population inversion due to fluorescence losses. For this reason the observed threshold will be higher than that calculated from the simple gain equals loss condition in equation (2.1.30). Since operation near threshold is being considered,

the circulating photon density is assumed to be small. Below threshold the population inversion therefore decreases only through fluorescent decay according to

$$n_2(t) = n_i \exp\left(-t/\tau_f\right) \tag{2.3.23}$$

The new threshold population inversion, $\overline{n}_{th}$ must now be sufficiently large such that during the build-up time it decays to the old threshold inversion, n_{th}. Substituting into the above equation then defines the build-up time, t_{bu}, to reach threshold,

$$n_{th} = \overline{n}_{th} \exp\left(-t_{bu}/\tau_f\right) \tag{2.3.24}$$

In order to obtain a useful expression for the new population inversion threshold, equation (2.3.2) must be solved near threshold. Using equation (2.3.23), equation (2.3.2) can be solved, yielding

$$\ln\frac{\phi}{\phi_i} = \frac{n_i}{n_{th}}\frac{\tau_f}{\tau_c}\left(1-\exp\left(-\frac{t}{\tau_f}\right)\right) - \frac{t}{\tau_c} \tag{2.3.25}$$

Where the initial photon density ϕ_i is given by spontaneous emission in the correct mode. It is assumed that at threshold there will be a measurable photon density, ϕ_{th}. This is used together with equation (2.3.24) to evaluate the above expression at a time equal to the build-up time. The solution becomes

$$1+\frac{\tau_c}{\tau_f}\ln\frac{\phi_{th}}{\phi_i} = \frac{\overline{n}_{th}}{n_{th}} - \ln\frac{\overline{n}_{th}}{n_{th}} \tag{2.3.26}$$

From fluorescence noise estimates the logarithm $\ln(\phi_{th}/\phi_i)$ yields a value of about 20[28]. The choice of noise source therefore affects the outcome. This is a transcendental equation for $\overline{n}_{th}$ and so the usual method of determining the cavity losses, as outlined in section (2.1.5), is not applicable. Instead numerical methods are required.

From the above solution it is also possible to see the effect of the upper state lifetime. If this is assumed large compared to the build-up time then the above threshold condition reduces to the previous threshold condition, i.e. $\overline{n}_{th} = n_{th}$, as expected. It is clear then that when threshold is considered in a gain switched system, the fluorescent decay due to the finite

upper state lifetime must not be neglected. The effect of a finite upper state lifetime is to increase the threshold compared to that obtained by the simple gain equals loss condition. This leads to a pronounced slope near threshold in an input versus output energy curve. The implication of this phenomenon is that there is no longer a linear relationship between threshold and the intracavity losses. This means that it is not possible to determine the intracavity losses by the method of Findlay and Clay[15] as discussed in section (2.1.5).

2.4 Injection seeding theory

In this section the basic formalism necessary to describe the salient features of injection seeded oscillators will be presented. The formalism doesn't lend itself to an analytic solution and numerical recipes are required. The same understanding of the process is attainable in a more qualitative manner by using the phasor description of the interacting fields. The analytical model will be presented first. The phasor approach will then be used to obtain the correct description of the dynamic behaviour.

2.4.1 The analytic approach

The specific point of interest to be dealt with in considering the process of injection seeding of a laser oscillator is that of mode selection. It is therefore necessary to consider the laser rate equations describing the time evolution of the oscillating fields. Consider the evolution of a the field oscillating at the frequency of the seed input.

$$\vec{E}(t)=\frac{1}{2}\left[\vec{E}_{\omega_i}(t)\mathrm{e}^{j\omega_i t}+c.c.\right] \qquad (2.4.1)$$

where $\vec{E}_{\omega_i}(t)$ is the time varying complex phasor at the seed frequency ω_i. In the case when this seed frequency isn't resonant with the nearest cavity mode at frequency ω_c, then after one round trip the injected field will be out of phase by an amount $\Delta\omega=\omega_i-\omega_c$. In this general case, the field equivalent of the photon rate equation (given by equation (2.1.26)) is

$$\frac{d\vec{E}_{\omega_i}(t)}{dt}-\left[\frac{c\,n_2\sigma_{21}l}{2l'}-\frac{1}{2\tau_c}-j\Delta\omega_i\right]\vec{E}_{\omega_i}(t)=0 \qquad (2.4.2)$$

This accounts for the usual gain and losses associated with a laser, as well as an additional loss mechanism due to dephasing. This equation must be solved in conjunction with the inversion density equation (2.1.27) where the photon density written in terms of the electric field is given by

$$\phi = \frac{\varepsilon c}{2}\left|\vec{E}_{\omega_i}(t)\right|^2 \qquad (2.4.3)$$

These coupled equations then describe the evolution of the field at the seed frequency ω_i inside the laser oscillator. In order to proceed, the externally injected signal must now be included in equation (2.4.2). It will appear as a driving term on the right hand side of this equation, yielding

$$\frac{d\vec{E}_{\omega_i}(t)}{dt} - m(t)\vec{E}_{\omega_i}(t) = \frac{m(t)}{e^{m(t)t_R} - 1}\vec{E}^{i}_{\omega_i}(t) \qquad (2.4.4)$$

where

$$m(t) = \frac{c\, n_2 \sigma_{21} l}{2l'} - \frac{1}{2\tau_c} - j\Delta\omega_i \qquad (2.4.5)$$

and[29]

$$C\{m(t)\} = \frac{m(t)}{e^{m(t)t_R} - 1}$$

is the coupling coefficient which is determined by imposing the periodic boundary condition

$$\vec{E}_{\omega_i}(t + t_R) = \vec{E}_{\omega_i}(t)e^{m(t).t_R} + \vec{E}^{i}_{\omega_i}(t) \qquad (2.4.6)$$

The coupled equations, (2.1.27) and (2.4.4), may be solved to describe the build-up of the laser field in the presence of an injected field. These equations may also be used to describe the build-up of any other modes which may be initiated by noise. In this case there will be no frequency mismatch between the noise field and the generated field, so that $\Delta\omega_i = 0$ in equation (2.4.5). The injected field in equation (2.4.4) is replaced by the square root of the photon noise density per mode. The photon noise density per mode

$$\vec{E}_{noise} = \sqrt{\frac{n_2 c \sigma_{21} \tau_c}{2V}} \qquad (2.4.7)$$

when substituted into equation (2.4.4), is exactly the noise term mentioned in equation (2.1.26). V represents the resonator mode volume. The competition between modes arising naturally and those arising from an externally injected signal has been investigated[29,30] indicating that for a seeding field far enough from a cavity resonance, natural modes may still predominate.

In general the above coupled equations for an injection seeded oscillator will need to be solved numerically[29,31]. The equations may be separated into real and imaginary parts. The real part will describe the evolution of the field amplitude, while the imaginary part will describe the evolution of the phase, and hence frequency shift, of the oscillating field. While the numerical solution will not be presented here, it is possible to gain physical insight into the processes by considering the evolution of the oscillating fields in terms of their phasor description.

2.4.2 Phasor approach to mode selection

Mode selection and control by injection seeding can be qualitatively explained with the help of the phasor model description of the fields[32]. The general configuration in a seeding experiment is depicted in Figure 2.9.

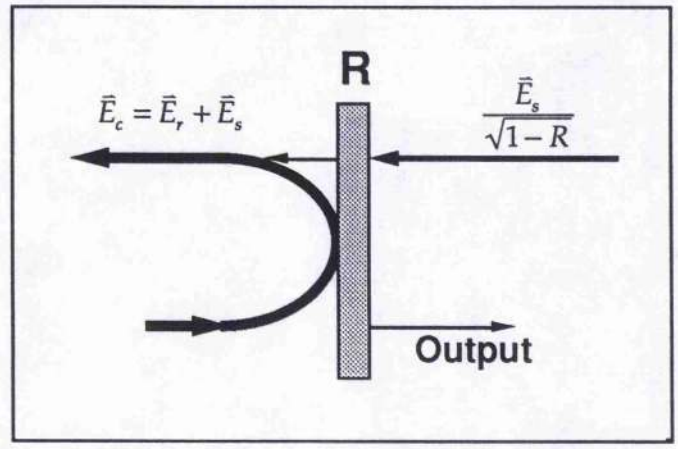

Figure 2.9 is a schematic representing the various fields in an injection seeded device.

The various fields are the injected seed field, $\vec{E}_s/\sqrt{1-R}$, the circulating field, $\vec{E}_c$, and the return field, $\vec{E}_r$. The circulating field, at any time, just inside the output coupler of reflectivity

R, is made up of the internal seed field $\vec{E}_s$ and the return field. The return field, $\vec{E}_r$, is simply the circulating field from one round trip previously which has subsequently propagated around the resonator experiencing the various gains, losses and phase shifts. This basically amounts to the periodic boundary condition expressed in equation (2.4.6) where the return field is the first term on the right hand side

$$\begin{aligned}\vec{E}_c(t+t_R) &= \vec{E}_c(t)e^{m(t).t_R} + \vec{E}_s(t) \\ &= \vec{E}_r(t+t_R) + \vec{E}_s(t)\end{aligned} \qquad (2.4.8)$$

In the phasor description of light, each field is represented by a rotating vector whose magnitude gives the field amplitude and whose rotation speed gives the frequency. By depicting the phasors representing the various fields in the reference frame of the injected field phasor, the relative phases become apparent. For example in the steady state at threshold, Figure 2.10 depicts the phasor relationships between the three fields. Case (a) represents the situation of on resonance seeding and case (b) represents the situation when the frequency of the injected signal does not correspond to any cavity mode. In this case after one round trip there will be a phase difference of

$$\Delta\omega = \omega_c - \omega_i, \qquad (2.4.9)$$

where ω_c is the nearest cavity mode frequency and ω_i is the frequency of the injected field. However, since the system is at threshold, the return phasor and the injected phasor will add up to reproduce the phasor of the circulating field after each round trip. The circulating field is thus oscillating at the injected signal frequency.

The case where the system experiences net gain (gain switching) is depicted in Figure 2.11. After each round trip the return field returns as the old circulating field but greatly amplified and having undergone a phase shift given by equation (2.4.9). The new circulating field is then obtained by adding the injected field. It is apparent that after only a few round trips the injected field becomes insignificant compared to the exponentially amplified circulating and return fields so the threshold circulating field is not reproduced upon each round trip. The rapidly amplified fields will continue to see a phase shift of $\Delta\omega t_R = (\omega_c - \omega_i)t_R$ per round trip. Since the phase diagram is defined in the reference frame of the injected signal which is

rotating at frequency ω_i, and phasor of the circulating field is rotating at frequency $(\omega_c - \omega_i)$ in this reference frame, then the frequency of the oscillating field will no longer be that of the injected signal but rather that of the nearest cavity mode.

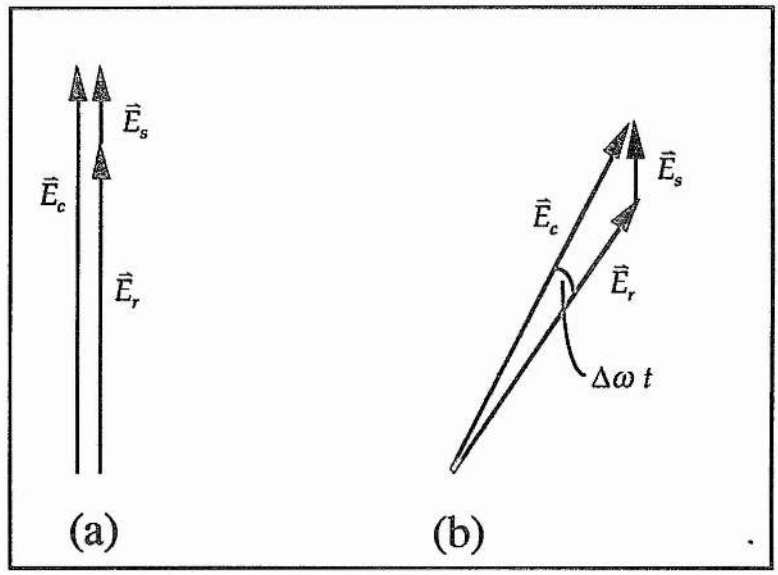

Figure 2.10 Indicates the phasor construction of the circulating field at threshold for the cases of (a) a resonant and (b) a non-resonant injected field.

The change in frequency of the oscillating field from that of the injected field to the nearest cavity mode occurs extremely rapidly, within a few round trips so that all the measurable output appears at a the cavity mode frequency[29,31]. The injected signal determines the initial conditions from which the laser pulse will build up. This control extends only to the selection of the cavity mode which will be allowed to predominate. It is important to keep in mind that the laser pulse initiated in the presence of a seed field, may also contain modes other than that selected by the seed field. If the injected field is far from any cavity resonance, it will suffer a large phase shift and hence experience less gain than the spontaneous fields in any allowed modes. While the injected signal will be large compared to the spontaneous emission in any allowed resonator mode, the loss due to a large phase shift may allow some of the competing spontaneously initiated modes to saturate the gain first. Even well seeded pulses may include contributions from spontaneously initiated modes which will degrade the spectral purity of the output[30].

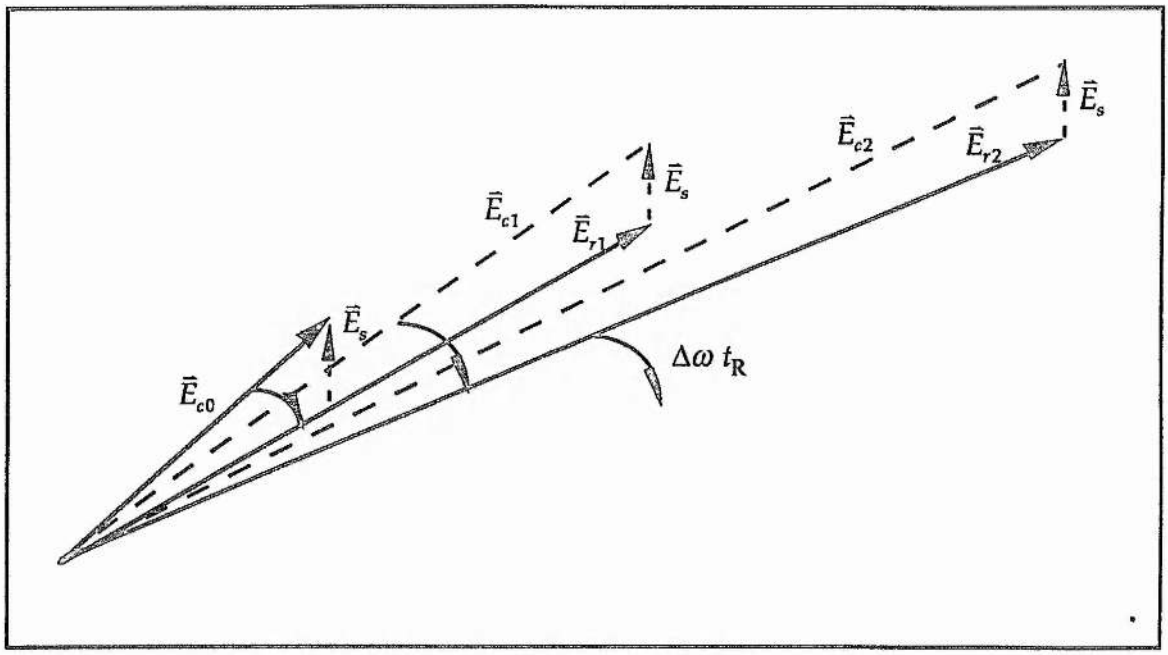

Figure 2.11 Indicates the evolution of the circulating field phasor in the presence of gain after successive round trips. There is a net rotation of the oscillating phasor of $\Delta\omega t_R$ per round trip.

This interpretation, afforded by the phasor model of the fields, is confirmed by the results of the numerical solution of the coupled equations describing the evolution of the oscillating field[29,31].

2.5 Theory of second harmonic generation

In this section the basic results of second harmonic generation will be introduced. This section is not intended to be comprehensive. The intention is to present the results required to determine the optimum crystal choice and system layout for the frequency doubling of a given source.

2.5.1 Basic SHG theory

Second harmonic generation is the simplest non-linear process in a family of interactions known as optical parametric interaction. These are general three-wave interactions, with $\omega_p = \omega_1 + \omega_2$, which can only take place in non-centrosymmetric media. In the simplified case of second harmonic generation, the two fields generated via the non-linear propagation

of the pump ω_p, are of the same frequency and at the second harmonic of the pump, i.e. $\omega_{SHG} = \omega_1 = \omega_2 = 2\omega_p$. In this case the simplified coupled non-linear equations describing the interaction of the fields through the medium are given by[33]

$$\frac{dE_p}{dz} = -\frac{i\omega_p}{2}\sqrt{\frac{\mu}{\varepsilon_p}}d_{eff}E_p^* E_{SHG}\, e^{-i\Delta kz} \tag{2.5.1}$$

$$\frac{dE_{SHG}}{dz} = -i\omega_p\sqrt{\frac{\mu}{\varepsilon_{SHG}}}d_{eff}\left|E_p\right|^2 e^{i\Delta kz} \tag{2.5.2}$$

The slowly varying amplitude approximation has been made and all losses have been neglected. The other symbols are defined as follows:

$$\varepsilon_i = \varepsilon_0(1+\chi_e) = \varepsilon_0 n_i^2 \tag{2.5.3}$$

is the permittivity of the medium at the relevant wavelength. χ_e is the linear susceptibility and n_i is the refractive index at the appropriate wavelength as given by the subscript. d_{eff} is the second order non-linear susceptibility which acts as a coupling coefficient which facilitates the exchange of energy between the fields. Finally, in the argument of the exponential, the term

$$\Delta k = k_{SHG} - 2k_p = \frac{2\omega_p}{c}\left(n_{SHG} - n_p\right) \tag{2.5.4}$$

describes the difference in phase of the fundamental and second harmonic fields, where the relation $k_i = \omega_i n_i / c$ has been used. In the case of plane waves with no pump depletion, i.e. $E_p(z)$ is constant, the magnitude of the second harmonic field generated over a crystal length l, is found to be

$$\left|E_{SHG}(l)\right|^2 = \omega_p^2\frac{\mu}{\varepsilon_{SHG}}d_{eff}^2\left|E_p\right|^4 l^2\frac{\sin^2\left(\Delta kl/2\right)}{\left(\Delta kl/2\right)^2} \tag{2.5.5}$$

This can be rewritten as an intensity for an input beam of area A, yielding[33]

$$I_{SHG} = \frac{P_{SHG}}{A} = \frac{1}{2}\sqrt{\frac{\varepsilon_{SHG}}{\mu}}\left|E_{SHG}\right|^2 \tag{2.5.6}$$

This enables an extraction efficiency to be defined

$$\eta_{SHG} = \frac{I_{SHG}}{I_p} = 2\left(\frac{\mu}{\varepsilon_0}\right)^{\frac{3}{2}} \frac{\omega_p^2 d_{eff}^2 l^2}{n_{SHG}^3} \frac{\sin^2\left(\Delta kl/2\right)}{\left(\Delta kl/2\right)^2} \frac{P_p}{A} \qquad (2.5.7)$$

The most important fact to notice here is that the extraction efficiency depends directly on the input pump intensity. Discussion of the optimisation of the generated second harmonic will be deferred to a subsequent section after the effects of Gaussian beam focusing are taken into account.

2.5.2 SHG with focused Gaussian beams

The simple solution presented above is for collimated plane waves. It is possible to take both the Gaussian beam nature and focusing into account. Provided the focused beam has a large confocal parameter compared to the non-linear medium length, or $z_0 >> l$, it can be treated as being essentially collimated in the interaction region. It therefore only remains to account for the Gaussian cross-section of the beam. Rewriting the field cross-section with a Gaussian variation

$$E_p(r) = E_{p_0} e^{-\left(r/w_0\right)^2} \qquad (2.5.8)$$

and integrating equation (2.5.7) over the extent of the beam yields for the efficiency,

$$\eta_{SHG} = \frac{I_{SHG}}{I_p} = 2\left(\frac{\mu}{\varepsilon_0}\right)^{\frac{3}{2}} \frac{\omega_p^2 d_{eff}^2 l^2}{n_{SHG}^3} \frac{\sin^2\left(\Delta kl/2\right)}{\left(\Delta kl/2\right)^2} \frac{P_p}{\pi w_0^2} \qquad (2.5.9)$$

which is essentially the same result as before. This equation predicts an increased efficiency upon decreasing the pump waist w_0. However, this simultaneously reduces z_0 (see equation (2.2.6)) so that at some point the condition $z_0 >> l$ is no longer satisfied and the variation of the beam radius $w(z)$ through the medium must be taken into account. There will thus be an optimal focusing condition for a given crystal length. It has been shown that, in the absence of double refraction, the optimal focusing condition yielding maximum conversion efficiency is given by[34]

$$2z_0 \cong \frac{l}{2.84} \qquad (2.5.10)$$

and as such falls outwith the realm of the above equation. Basically this result indicates that efficient frequency doubling is possible even with a beam area which is substantially greater than that at the focus. It is perhaps surprising that a higher efficiency is attained for beams focused more tightly than that given by the confocal condition.

2.5.3 Phase matching considerations

It is now important to consider the effect of the relative phase of the fundamental and second harmonic beams in the crystal. The phase difference is given in equation (2.5.4) which appears in the sinc^2 function in the conversion efficiency equations. As expected, this function implies optimum conversion for perfectly phase matched beams, or

$$\Delta k = \frac{2\omega_p}{c}\left(n_{SHG} - n_p\right) = 0 \qquad (2.5.11)$$

In general this will not be satisfied since the refractive indices at the two wavelengths will be different. Fortunately the natural birefringence of suitable crystals may be used to ensure that this condition is achieved. Birefringence will not be dealt with here. Suffice it to say that uniaxial or biaxial crystals have different refractive indices for propagation along the different crystal axes. Thus for propagation at an arbitrary angle through a crystal, the effective refractive index will be a sum of the principal refractive indices. In the case of a uniaxial crystal this is given by

$$\frac{1}{n_e^2(\theta)} = \frac{\sin^2\theta}{n_e^2} + \frac{\cos^2\theta}{n_o^2} \qquad (2.5.12)$$

where n_e is the extra-ordinary refractive index for propagation along the z-axis and n_o is the ordinary refractive index which is the same for propagation along both the x- and y-axes. It is therefore possible to select the propagation direction such that the phase-matching condition is satisfied. There are two possible polarisation configurations for achieving this in a negative uniaxial $n_o > n_e$ crystal. The first is where the linear polarisations of the two pump beams are parallel and in the second configuration they are perpendicular. The methods are respectively termed type-I and type-II processes and phase-matching is achieved as follows:

$$n^{e}_{SHG}(\theta_m) = n^{o}_{p} \qquad \text{type}-\text{I}$$

$$n^{e}_{SHG}(\theta_m) = \frac{1}{2}\left\{n^{e}_{p}(\theta_m) + n^{o}_{p}\right\} \qquad \text{type}-\text{II} \qquad (2.5.13)$$

θ_m is termed the phase-matching angle. If it turns out that phase-matching is achieved at an angle other than $\theta_m = 90°$ then there will be double refraction. In this case the fundamental and second harmonic Poynting vectors will propagate at an angle to one another which will therefore reduce the energy exchange between the beams. This phenomenon is termed walkoff, and the phase-matching leading to this is termed critical. In this case a further constraint is placed on the crystal length since no harmonic conversion can take place once the beams have separated[35].

In the case where the phase-matching condition is satisfied for propagation along or perpendicular to the optic axis, i.e. $\theta_m = 0°$ or $\theta_m = 90°$, and there is no separation of the beams, the phase-matching is termed noncritical. In some cases where the phase-matching is attained for angles sufficiently close to the noncritical condition, it is possible to utilise the temperature dependence of the refractive indices to force noncritical operation.

Most non-linear crystals are specified together with a detailed equation describing the dependence of the principal refractive indices on wavelength. These are called the Sellmeier equations. A model may be used to specify the temperature dependence of the principal refractive indices[36]. These two equations enable the phase-matching angle to be determined and also whether or not noncritical operation is possible for frequency doubling in a given crystal.

One final parameter which may affect SHG efficiency in the noncritical geometry is the finite divergence of the interacting beams. This will lead to change in the wave vector mismatch away from the optimum. By considering only small divergence away from optimum the mismatch is given by

$$\Delta k \approx \beta_\theta \delta\theta \text{ , where} \qquad (2.5.14)$$

$$\beta_\theta = \frac{4\pi}{\lambda_p n^{o}_{p}}\left(n^{o}_{SHG} - n^{e}_{SHG}\right)\sin 2\theta_m$$

This β_θ parameter is a measure of the angular sensitivity of the crystal and as such leads to an expression for the angular tolerance of the fundamental beam[37]

$$\Delta\theta_m = \frac{5.56}{l\beta_\theta} \tag{2.5.15}$$

This is the full external angle leading to performance levels at the FWHM of the generation process.

2.5.4 Optimising SHG efficiency

Optimum efficiency of the SHG process depends on the interplay of the various considerations discussed above. Eimerl[38] was able to show that the efficiency of the process depended only on the pump laser characteristics:

$$\eta = \eta_0\left(\frac{\sin\delta}{\delta}\right) \tag{2.5.16}$$

where

$$\eta_0 = \frac{5.46 d_{eff}}{\lambda_p n_p \sqrt{n_{SHG}}} \tag{2.5.17}$$

$$\delta = \frac{\Delta k l}{2} \tag{2.5.18}$$

The detuning parameter δ contains all the information about basic phase-matching, beam walkoff and beam divergence and temperature sensitivity. The analysis shows that for a given intensity and divergence, there is an optimal crystal length as described earlier. Basically any increase in this intensity by increased focusing is offset equally by a decreased optimal crystal length and increased dephasing due to the larger divergence[38]. Thus knowledge of the pump characteristics will enable both a suitable crystal and the correct focusing to be selected such that the efficiency of the second harmonic generation process is maximised.

References

[1] W. Koechner in: Solid-state Laser Engineering 3rd Ed. (Springer, 1992),

[2] A.E. Siegman in: Lasers, (University Science Books, 1986)

[3] Th. Graf and J.E. Balmer, *Opt. Lett.*, 18, (1993), p1317

[4] H.R. Verdún and Ti Chuang, "Efficient TEM_{00}-mode operation of a Nd:YAG laser end pumped by a three-bar high-power diode-laser array", *Opt. Lett*, 17, (1992), p1000

[5] T.S. Rose, J.S. Swenson and R.A. Fields, *OSA Proc. of Adv. Solid-State Lasers*, 13, Eds. L.L. Chase and A.A. Pinto, (1992), p186

[6] S. Yamaguchi and H. Imai, "Efficient Nd:YAG Laser End-Pumped by a 1 cm Aperture Laser-Diode Bar with a GRIN Lens Array Coupling", *IEEE J. of Quant. Elec.*, QE-28, (1992), p1101

[7] R. Beach, R. Reichert, W. Benett, B. Freitas, S. Mitchell, A. Velsko, J. Davin and R. Solarz, *Opt. Lett.*, 18, (1993), p1326

[8] W.A. Clarkson, A.B. Neilson and D.C. Hanna, "Novel beam shaping technique for high power diode bars", Conference on Lasers and Electo-optics (CLEO '94), Anaheim USA, May 1994, Technical Digest Series 8 , p360

[9] J. Zehetner, "Highly efficient diode-pumped elliptical mode Nd:YLF laser", *Opt. Comm.*, 117, (1995), p273

[10] K. Kubodera and K. Otsuka, "Single transverse mode $LiNdP_4O_{12}$ slab waveguide laser", *J. Appl. Phys.*, 50, (1979), p653

[11] D.G. Hall, R.J. Smith and R.R. Rice, "Pump-size effects in Nd:YAG lasers", *Appl. Opt.*, 19, (1980), p3041

[12] D.G. Hall, "Optimum mode size criterion for low-gain lasers", *Appl. Opt.*, 20, (1981), p1579

[13] M.J.F. Digonnet and C.J. Gaeta, "Theoretical analysis of optical fiber laser amplifier and oscillators", *Appl. Opt.*, 24, (1985), p333

[14] T.Y. Fan and R.L. Byer, "Diode laser pumped solid-state lasers", *IEEE J. of Quant. Elecl.*, QE-24, (1988), p895

[15] D. Findlay and R.A. Clay, "The measurement of internal losses in 4-level lasers", *Phys. Lett.*, 20, (1966), p277

[16] N. Hodgson and H. Weber, "Measurement of extraction efficiency and excitation efficiency of lasers", *J . of Mod. Opt.*, 35, (1988), p807

[17] A. Yariv in *Quantum Electronics 3rd Ed.*, John Wiley and Sons (1989), Ch. 6

[18] A.C. Walker in *The Physics and Technology of Laser Resonators*, eds. D.R. Hall and P.E. Jackson, Bristol: Hilger, (1989), Ch. 1

[19] H. Kogelnik and T. Li, "Laser Beams and Resonators", *Proc. of IEEE*, 54, (1966), p1312

[20] H. Kogelnik, "Imaging of optical modes - Resonators with internal lenses", *Bell Sys. Tech. J.*, 44, (1965), p455

[21] W. Koechner in *Solid-State Laser Engineering 3rd Ed.*, Springer-Verlag, (1992), Ch. 5

[22] D.R. Whitehouse, C.F. Luck, C van Mertens, F.A. Horrigan and M. Bass, Rept. TR ECOM-0269-F, "Mode control technology for high performance solid state laser", US Army Electr. Command, Fort Monmouth, NJ, (1963)

[23] H. Steffen, J.P. Lörtscher and G. Herziger, "Fundamental mode radiation with solid-state lasers", *IEEE J. of Quant. Elec.*, QE-8, (1972), p239

[24] H.W. Kogelnik, E.P. Ippen, A. Dienes and C.V. Shank, "Astigmatically compensated cavities for cw dye lasers", *IEEE J. Quant. Elec.*, QE-8, (1972), p373

[25] D.C. Hanna, "Astigmatic gaussian beams produced by axially asymmetric laser cavities", *IEEE J. of Quant. Elec.*, QE-5, (1969), p483

[26] A.E. Siegman in: Lasers, (University Science Books, 1986), Ch8, p465

[27] J.J. Degnan, "Theory of the optimally coupled Q-switched laser", *IEEE J. of Quant. Elec.*, QE-25, (1989), p215

[28] J.M. Egglestone, L.G. DeShazer and K.W. Kangas, "Characteristics and kintetics of laser-pumped Ti:sapphire oscillators", *IEEE . of Quant. Elec.*, QE-24, (1988), p1009

[29] J-L Lachambre, P Lavigne, G. Otis and M Noël, "Injection Locking and Mode Selection in TEA-CO_2 Laser Oscillators", *IEEE J. of Quant. Elec.*, QE-12, (1976), p756

[30] N.P. Barnes and J.C. Barnes,, "Injection seeding I: Theory", *IEEE J. of Quant. Elec.*, QE-29, (1993), p2670

[31] Y.K. Park, G. Giulina and R.L. Byer, "Single axial mode operation of a Q-switched Nd:YAG oscillator by injection seeding", *IEEE J. of Quant. Elec.*, QE-20, (1984), p117

[32] A.E. Siegman in: Lasers, (University Science Books, 1986), Ch 29, p 1154

[33] A. Yariv in *Quantum Electronics 3rd Ed.*, John Wiley and Sons (1989), Ch. 8

[34] G.D. Boyd and D.A. Kleinman, "Parametric interaction of focused Gaussian light beams", *J. Appl. Phys.*, 39, (1968), p3597

[35] G.D. Boyd, A. Ashkin, J.M. Dziedzic and D.A. Kleinman, *Phys. Rev.*, 137, (1965), p1305

[36] S.P. Velsko, M. Webb, L. Davis and C. Huang, *IEEE J. of Quant. Elec.*, QE-27, (1991), p2182

[37] W. Koechner in *Solid-State Laser Engineering 3rd Ed.*, Springer-Verlag, (1992), Ch. 10, p520

[38] D. Eimerl, "High Average Power Harmonic Generation", *IEEE J. of Quant. Elec.*, QE-23, (1987), p575

CHAPTER 3

VIBRONIC CRYSTAL SELECTION

3.1 Introduction

In this chapter a detailed comparison of the four most prominent near infrared vibronic laser materials will be presented. The four crystals; Alexandrite, Ti:sapphire, Cr:LiCAF and Cr:LiSAF will be discussed individually. Central to the discussion of each crystal will be the suitability for diode pumping as well the potential for efficient Q-switched operation. After the general discussion, the projected Q-switched performance of each material will be compared. This will be followed by an analysis of the comparative gain-switched performance of the various materials. These comparisons will enable the selection of the vibronic laser crystal best suited to the construction of a tuneable all-solid-state, Q-switched or gain-switched laser system. This chapter will also include a discussion on the feasibility of a direct diode pumped version of the above laser system. The comparisons made in this chapter are crucial in determining the choice of vibronic material used in this work.

3.2 Vibronic Laser Kinetics

Vibronic lasers can be treated as four-level lasers as described in section 2.1.2. However, there is a strong coupling between the vibrational modes of the host lattice and electron distribution of the active species. This results in the various discrete energy levels of laser materials akin to Nd:YAG being broadened into bands with many vibrational sub-levels as depicted in Figure 3.1. When an excited atom decays into the upper laser level, it loses vibrational energy and drops to the bottom of the pump band which is the upper laser level. In these materials the ground state is often the lowest vibrational sublevel of the lower laser band. In other words, after an active atom has undergone a laser transition to a vibrationally excited sublevel of the lower laser level, it will decay by losing vibrational energy, as phonons, to the lowest vibrational sublevel or ground state. This means that lasing can occur

for transitions terminating anywhere in the lower, vibrationally broadened, band. Left alone such a laser will operate over a substantial range near the peak of the gain curve.

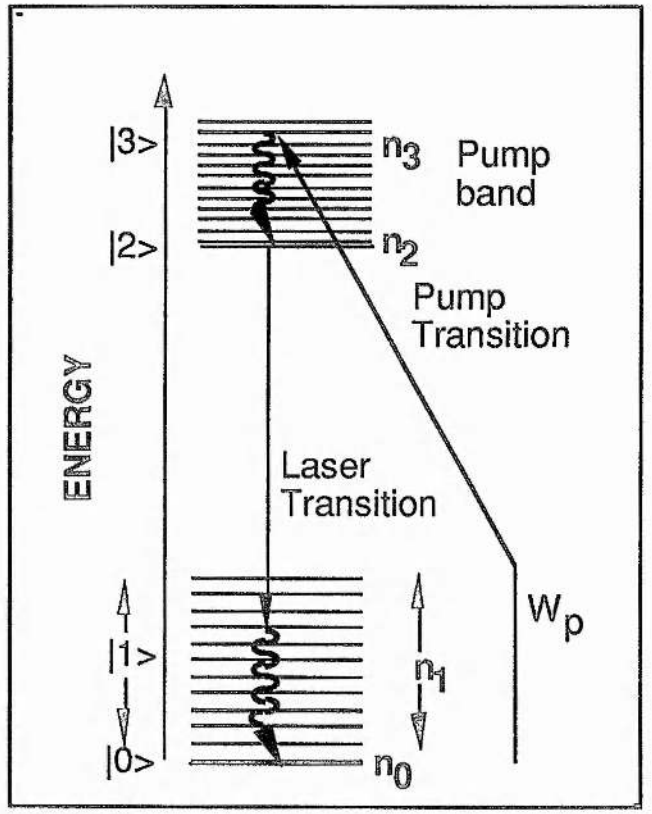

Figure 3.1 Is a schematic representation of the energy level diagram of a vibronic laser.

The employment of frequency selective techniques is required to restrict the operational bandwidth of such a laser while simultaneously allowing tuning anywhere within the laser gain curve. From Figure 3.1 it may be surmised that temperature plays a crucial role in the operation of vibronic lasers. Since the vibrational sublevels of the ground state are thermally populated, it is advantageous to prevent elevated temperatures. As the temperature rises it becomes more difficult for a population inversion with the lower vibrational sublevels to be attained. Therefore elevated temperatures result in more of the laser emission being at longer wavelengths. Due to strong electron-phonon coupling and the Jahn-Teller effect, nonradiative transitions are possible[1]. These nonradiative transitions out of the upper laser level become more prominent with increasing temperature and tend to reduce the population inversion and hence the operational efficiency.

3.3 Discussion of Near Infrared Vibronic Materials

A table comparing the relevant optical and thermo-mechanical properties of the four vibronic crystals is presented below. These materials will now be discussed in turn, highlighting the merits of each.

	Alexandrite [2]	Ti:sapphire	Cr:LiCAF	Cr:LiSAF
Emission X-section ($x10^{-19}$ cm^2)	0.07- 0.3 (@ 22° - 290°)	E ∥ c 3.2 E ⊥ c 1.7 [12]	E ∥ c 0.12 [29] E ⊥ c 0.09	E ∥ c 0.5 [36] E ⊥ c 0.25
Transition lifetime (μs)	260	3.2 [9,20]	170 [29]	67 [36]
Pump Band (nm)	380 - 630	400 - 650 [9,26]	550-700 [29,31]	550-750 [36]
Absorption X-section ($x10^{-19}$ cm^2)	0.5 (@22°)	E ∥ c 0.6 (@490nm) [9]	E ∥ c 0.25 [29] E ⊥ c 0.20	E ∥ c 0.45 [36] E ⊥ c 0.25
Tuning Range (nm)	700 - 825 (@ 22° - 290°)	680 - 1100 [20]	720-840 [29]	760-1010 [41]
Refractive Index	1.74 (250nm - 2.6μm)	1.76 [27]	1.39 [35]	1.41 [38] (400-1200nm)
dn/dT ($x10^6$ K^{-1})	E ∥ a 9.4 ± 0.5 [35] E ∥ b 8.3 ± 0.5	12.6 [27]	E ∥ c -4.6 [31,35] E ⊥ c -4.2	E ∥ c -4.0 [38] E ⊥ c -2.5
Dopant Concentration (at. %)	0.01 - 0.4 [3]	0.1-0.16	>8.8 [31]	up to 100 [39]
Thermal Conductivity ($W.cm^{-2}.K^{-1}$)	0.23 (@22°) [35]	0.46 [28]	E ∥ c 0.051 [31,35] E ⊥ c 0.046	E ∥ c 0.039 [38] E ⊥ c 0.029 [28]
Thermal Expansion coeff ($10^{-6.°}C^{-1}$)	E ∥ a 4.4 E ∥ b 6.5 E ∥ c 6.9 [35]	5.8 [28]	E ⊥ c 22 E ∥ c 3.6 [31,35]	E ⊥ c 18.8 E ∥ c -10.0 [38]
K_{1c} Fract. Toughness ($Mpa.m^{1/2}$)	2.6 [35]	1.7 [28]	0.31 [35]	0.4 [28]
Thermo-mechanical FOM, R_T ($W.m^{-1/2}$)	14 [35]	5 [28]	0.53 [35]	0.40 [38]

Table 3.1 Compares various optical and thermo-mechanical properties of the near infrared vibronic laser crystals under consideration. Included is a Thermo-mechanical figure of merit.

3.3.1 Alexandrite ($Cr:BeAl_2O_4$)

Alexandrite was the first discovered vibronic laser material. It was being investigated as an alternative to ruby[2]. By 1985 it was a mature technology with several commercial examples available[3]. Alexandrite is usually doped with between 0.01% and 0.4% Chromium. The pump band extends from 380nm to 630nm and is peaked around 590nm. This is accessible with standard flashlamps. CW operation is also possible with arc-lamp pumping or laser pumping. There is another narrow absorption feature at 680nm which enables diode pumping[4]. Mechanically, alexandrite is strong enough to withstand the highest power Xenon flashlamps. Although a thermal lensing problem arises with high power lamp pumping, this is parabolic in nature and is therefore, to a large degree, correctable[5].

Alexandrite is tuneable over 700-825nm with a small emission cross-section of the order of 10^{-20} cm^2 (see Table 3.1), in this range. The optical spectra show a strong polarisation dependence. The dominant cause is the orthorhombic crystal structure which dominates over thermally induced polarisation[5]. Ground state absorption is found to be the limiting factor at the high energy (below 700nm) region of the tuning range[6], while the low energy region is limited by excited state absorption[7] which is also appreciable at the shorter wavelengths. An interesting feature of Alexandrite is that the emission cross-section increases with temperature. Thus as opposed to the expected decline in performance at elevated temperatures for vibronic materials, Alexandrite exhibits increased gain in this case. It has been found that the tuning range of Alexandrite can be extended to 858nm at a temperature of 360°C[3]. The stimulated emission lifetime is also found to be temperature dependent. As indicated in Table 3.1 it is roughly 260μs at room temperature and decreases for increased temperatures.

The small stimulated emission cross-section, ($0.6x10^{-21}cm^2$ at room temperature compared to about $5x10^{-19}cm^2$ for Nd:YAG), poses problems for efficient energy extraction. The smaller emission cross-section means that alexandrite can store more energy per unit volume since parasitic lasing is suppressed, but it also tends to increase the threshold (see equation 2.1.58). The saturation intensity (see equation 2.1.34) is also greatly increased which makes it more difficult to efficiently extract the stored energy. In fact the saturation intensity required for efficient energy extraction is sufficiently large that care has to be taken not to exceed the

damage threshold of >30 GW/cm^2. The long upper state lifetime (see Table 3.1) permits efficient energy storage under flashlamp pumping. This enables good Q-switched performance provided circulation intensities are high enough for efficient extraction. The long upper state lifetime somewhat counteracts the effects of the small emission cross-section in keeping the cw threshold reasonably low (see equation 2.1.31).

In summary, the combination of a low emission cross-section, large upper state lifetime and good mechanical properties make alexandrite well-suited for high-energy pulsed operation with flashlamp pumping. It is also, therefore, a good material for an oscillator-amplifier configuration. It is difficult, however, to maintain TEM_{00} operation under the high thermal loads concomitant with flashlamp pumping. The small emission cross-section also makes it difficult to achieve single frequency operation due to the losses of intracavity elements.

3.3.2 Ti:sapphire (Ti:Al_2O_3)

Ti:sapphire was invented in 1982[8]. It has rapidly been transformed into the most widely commercialised vibronic laser with many models of both cw and pulsed types available. A schematic of the potential energy surfaces of the titanium ion in the sapphire host is reproduced in Figure 3.2, showing the effect of the interaction of the titanium electrons and the lattice field.

The absorption band of Ti:sapphire extends from 400-650nm, as depicted in Figure 3.3, with a peak absorption cross-section of about 6×10^{-20}cm^2 at 490nm[9]. While this absorption band is compatible with flashlamp pumping, the very short upper state lifetime of Ti:sapphire renders flashlamp pumping highly inefficient. Ti:sapphire is therefore predominantly a laser pumped material operating in cw or gain-switched modes. With a peak absorption near 500nm Ti:sapphire is ideally suited to pumping by argon ion lasers or frequency doubled Nd-doped lasers. The high absorption cross-section means that short crystals absorb efficiently even at low doping densities of 0.1-0.16%.

Ti:sapphire has the largest known tuning range (680-1100nm) of any known solid-state material. Its peak emission cross-section of 3.2×10^{-19}cm^2 occurring at 780nm is also one of the largest for vibronic materials. The fluorescence is highly polarised[9]. Although there is a

residual absorption in the lasing bandwidth[10], this is well understood and has been minimised to such an extent that it does not adversely effect laser operation[11]. This is quantified by a figure of merit (FOM) which is the ratio of the absorption at the absorption peak (490nm), to that at 800nm, near the emission peak. Values of FOM>200 are considered good. The lasing wavelength bandwidth is so large that more than one mirror set is required to efficiently cover the whole range.

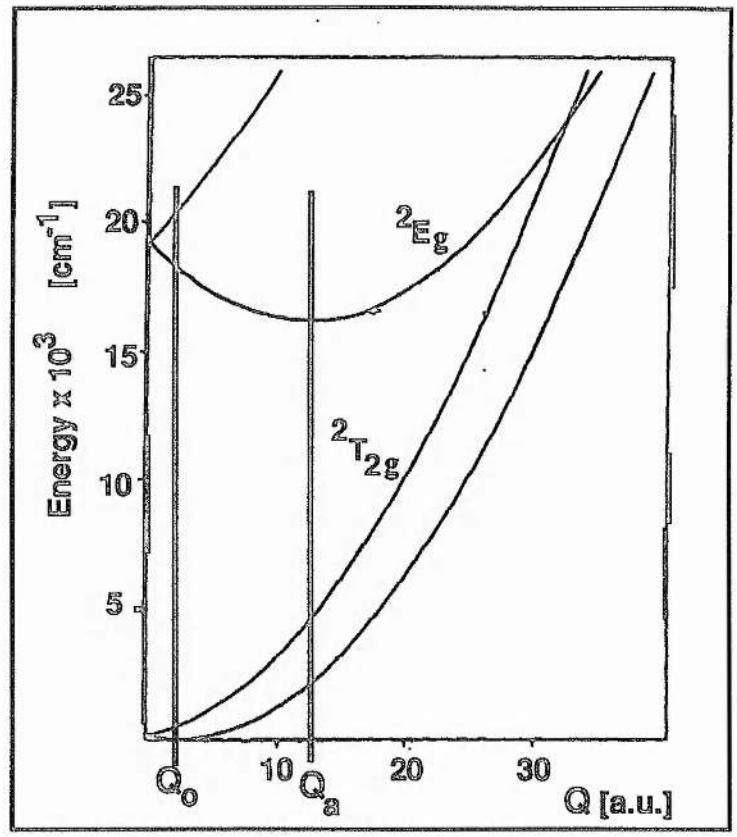

Figure 3.2: Representation of the relative locations of the potential energy surfaces of the titanium ion in the sapphire host as a function of a qualitative configurational coordinate[1].

Ti:sapphire (Ti:Al_2O_3) like ruby (Cr:Al_2O_3) is a hard crystal with good thermal, optical and mechanical properties. Thermal effects are observed, but seem to be easily corrected[11]. The upper state lifetime is reduced at temperatures above room temperature as a result of thermal quenching of the fluorescence due to multiphonon nonradiative decay[1,9].

The large stimulated emission cross-section successfully counterbalances the very short upper state lifetime in keeping the cw threshold down. Many cw Ti:sapphire lasers have been

demonstrated[1,9-14]. These have also been successfully line-narrowed[11,15] and stabilised as spectroscopic sources[16]. The very large emission cross-section (for vibronic media) makes Ti:sapphire ideally suited for pumping by a short-pulse source. Gain-switched Ti:sapphire lasers have been around for some time[9,17], as indeed have such sources offering line-narrowed output[18-24], including frequency-doubled versions[25].

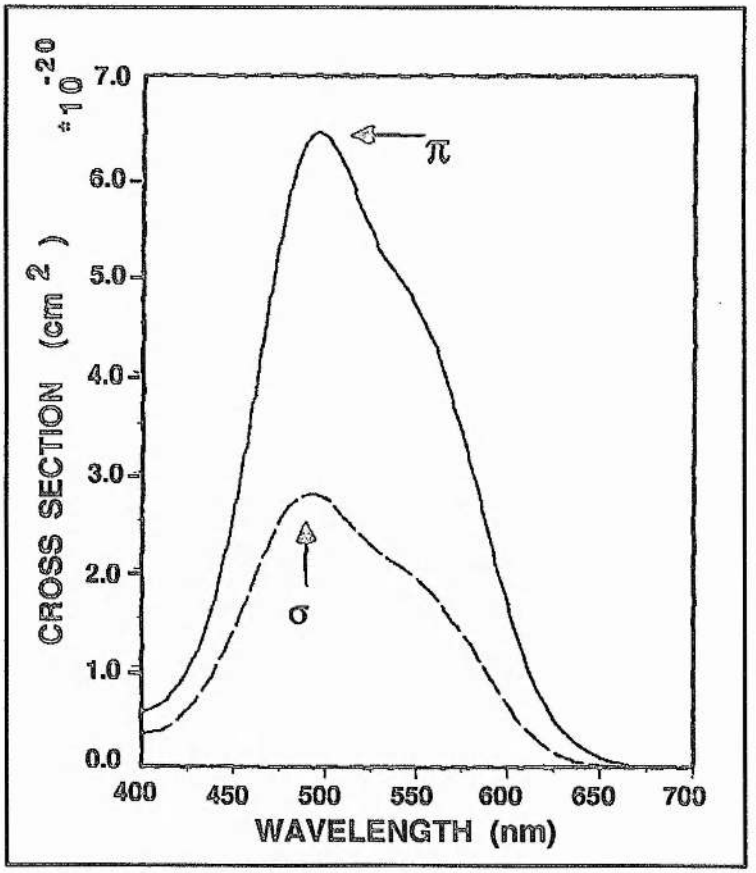

Figure 3.3: Polarised absorption cross sections for the $^2T_2 \rightarrow {}^2E$ transition in Ti:sapphire[9].

In summary, Ti:sapphire is an excellent material with regard to its spectroscopic and mechanical properties and its thermal handling capability. Its rather small upper state lifetime dictates that it is predominantly a laser pumped material. The high emission cross-section helps to keep the threshold low for cw operation and also facilitates rapid and efficient energy extraction in pulsed operation. It is the most widely established tuneable solid-state laser, having ousted the more cumbersome dye laser in many areas.

3.3.3 Cr:LiCAF (Cr:$LiCaAlF_6$)

A schematic of the potential energy surfaces of the chromium ion in the LiCAF host is reproduced in Figure 3.4, showing the effects of the interaction of the chromium electrons and the lattice field.

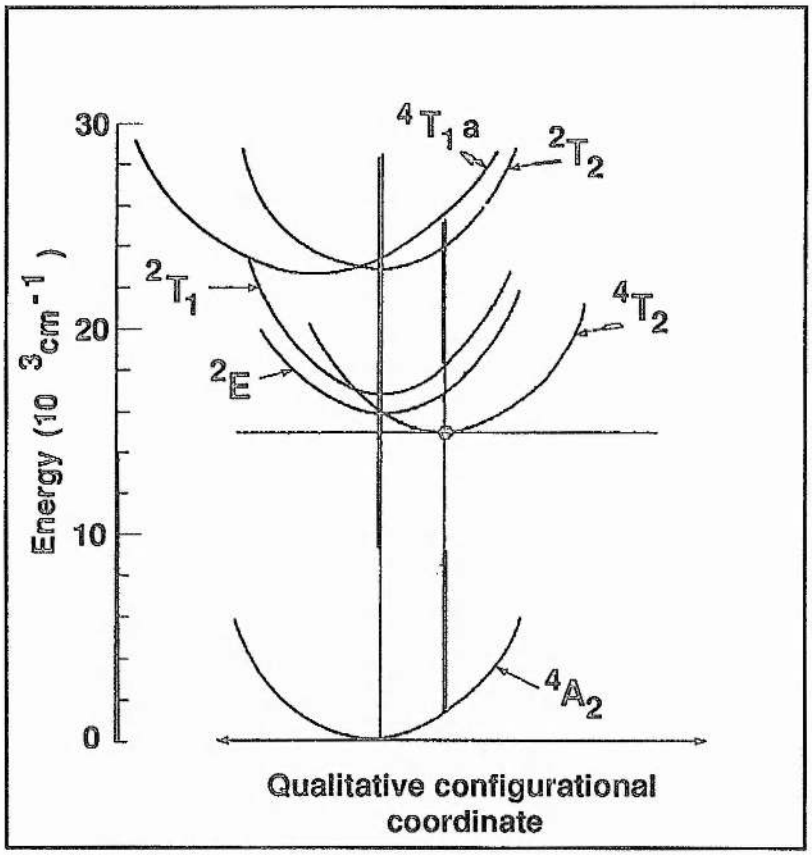

Figure 3.4: Representation of the relative locations of the potential energy surfaces of the chromium ion in the LiCAF host as a function of a qualitative configurational coordinate[29a].

The pump band of Cr:LiCAF extends from 550nm to 700nm[29], which overlaps well with the emission bands of xenon flashlamps. Peak absorption of $0.25 \times 10^{-19} cm^2$ occurs near 630nm. The upper state lifetime is also sufficiently long, 170μs[29], so that efficient flashlamp pumping is feasible. The pump bandwidth encompasses the 665-675nm wavelength range available to manufacturers of red laser diodes and Cr:LiCAF can, therefore, be laser diode-pumped[30]. The fact that crystal quality is not compromised with high doping levels[31] makes diode pumping in small crystals possible. The broad absorption band also means that

diodes don't have to be temperature stabilised, which helps to maintain high overall system efficiency.

The tuning range of Cr:LiCAF extends over 720-840nm which is roughly the same as that of alexandrite. Cr:LiCAF also suffers from a low stimulated emission cross-section; peak of $1.2x10^{-20}cm^2$ at 780nm[29], which limits efficient energy extraction. The fluorescence is polarised with stronger emission for polarisation parallel to the c-axis. Excited state absorption has been shown to exist in Cr:LiCAF, but it does not significantly reduce the performance[32]. Even though the upper state lifetime is suitable for the energy storage requirements of Q-switching, the small emission cross-section reduces its suitability for Q-switched operation. Cr:LiCAF is not susceptible to nonradiative decay at room temperatures[29] and has been shown to be totally unaffected below temperatures of 255°C[33]. There are two major problems when high-power operation is implemented; mechanical failure due to thermal stress and thermal beam degradation due to thermally-induced refractive index changes. The power level at which mechanical failure occurs is highest for materials with high fracture toughness, a low thermal expansion coefficient and a good thermal conductivity[34]. This is well illustrated by the thermo-mechanical figure of merit which appears for each of the considered media in Table 3.1. On the other hand, good beam quality requires a small refractive index change with temperature and isotropic thermal expansion. Unfortunately there is a trade-off between these two qualities in the available media. While fluoride hosts (Cr:LiCAF, Cr:LiSAF, Nd:YLF) tend to be characterised by excellent thermal properties, oxide hosts (alexandrite, Ti:sapphire, Nd:YAG) seem to exhibit superior Thermo-mechanical properties[35]. On the positive side, however, Cr:LiCAF is nearly as robust as Nd:YLF which has found numerous applications. Thermal distortions are much reduced in Cr:LiCAF; the thermal lensing effect of the negative dn/dT of Cr:LiCAF will tend to cancel with the positive contribution due to thermal expansion[35]. This means that Cr:LiCAF will have much reduced thermal lensing and so excellent beam quality may be expected.

In summary, alexandrite is more suited for high thermal load applications while Cr:LiCAF which exhibits low thermal distortion is more suited to applications like rangefinders, lidar and spectroscopy which require moderate powers with good beam quality[34].

3.3.4 Cr:LiSAF ($Cr:LiSrAlF_6$)

A schematic of the potential energy surfaces of the chromium ion in the LiCAF host is reproduced in Figure 3.4, showing the effects of the interaction of the chromium electrons and the lattice field. The potential energy surfaces of chromium in the LiSAF crystal host are expected to be similar[29a].

In Cr:LiSAF the pump band extends from 550nm to 750nm, with a peak absorption cross-section of $4.5x10^{-20}cm^2$ at 640nm[36]. The absorption and emission spectra appear in Figure 3.5. As with Cr:LiCAF this overlaps well with emission bands of xenon flashlamps. Cr:LiSAF also absorbs well over the 665-675nm emission region available to by red laser diode manufacturers[37]. Although the upper state lifetime, at 67μs, is somewhat reduced compared to Cr:LiCAF, efficient flashlamp pumping is still possible. Cr:LiSAF can accept very high doping concentrations without appreciable lifetime quenching and crystal quality degradation[38]. This fact together with good absorption of red laser diode emission means that efficient diode-pumping of small crystals is possible. Again the broad pump bandwidth means that diodes don't have to be temperature stabilised which helps to maximise overall system efficiency. Furthermore, this ability to accept high doping levels gracefully enables Cr:LiSAF to be wing-pumped, using either the long wavelength wing (e.g. 752nm) or the short wavelength wing (e.g. 488)[39]. The short wavelength wing is also accessible to pumping by frequency-doubled Nd-doped lasers at 530nm, as will be discussed in chapter 5. Harter et al.[40] looked at wing-pumping at longer wavelengths with the intention of evaluating the possibility of pumping by AlGaAs laser diodes. They found that bulk damage occurred at fluences above $15J/cm^2$ for 50-ns pulses. This is promising as it implies that saturated operation is possible without the risk of optical damage.

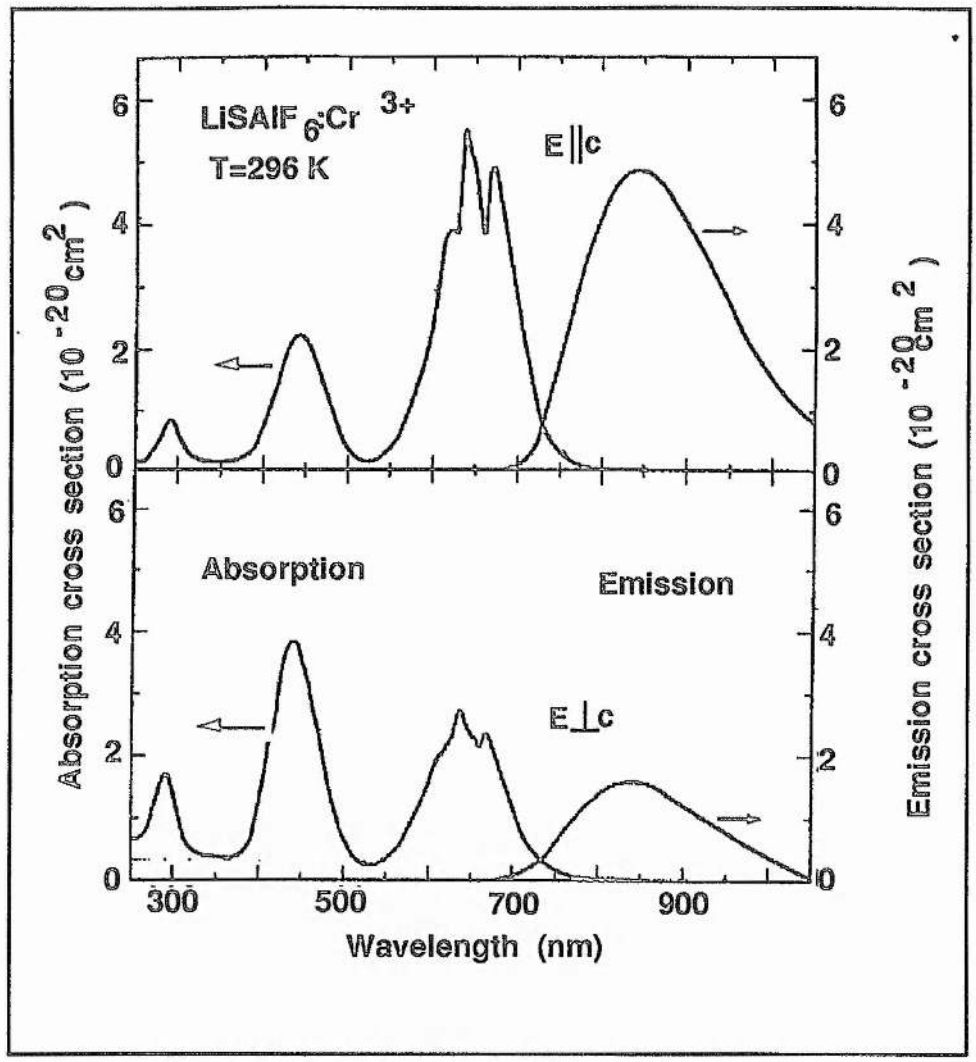

Figure 3.3: Polarised absorption and emission spectra of Cr:LiSAF [36].

The tuning range of Cr:LiSAF, which extends from 760nm to 1010nm[41], is surpassed only by that of Ti:sapphire. The emission cross-section, upper state lifetime product is the highest of all Cr-doped vibronic media. This serves to maintain low thresholds and improve extraction efficiency through a reduced saturation intensity. The large stimulated emission cross-section ($5x10^{-19}cm^2$ at peak) will also facilitate efficient Q-switch pulse extraction. However, it has been found that excited state absorption[36,42,43] and upconversion [39,40,43,44] are not negligible effects in Cr:LiSAF. The excited state absorption cross-section has been found to be roughly one third of the peak emission cross-section across the emission bandwidth[42,43]. The σ-polarised emission is completely suppressed by excited state

absorption[42,43]. Excited state absorption is also present in the pump band which reduces efficiency further.

An additional drawback has been encountered during high-power operation. The upper state lifetime of Cr:LiSAF was found to decline precipitously above 70 °C due to the onset of nonradiative decay which thus reduces laser efficiency[33]. This, together with a poor thermal conductivity (see Table 3.1 for a comparison), is a serious limitation to the power handling capability of Cr:LiSAF.

As mentioned before, fluoride hosts like Cr:LiSAF and Cr:LiCAF have poor mechanical properties compared to oxides, such as alexandrite and Ti:sapphire[35]. Like Cr:LiCAF, this restricts the possible applications of Cr:LiSAF to those not requiring high average powers. While reasonable beam quality may be expected due to the balancing of thermal expansion and thermal lensing, it should be noted that in Cr:LiSAF there is a large difference in the thermal expansion along the *a*- and *c*- axes[38]. This may result in a large thermally induced distortion in Cr:LiSAF if appropriate measures are not instituted.

3.4 Comparison of the Q-switched Performance

This discussion of projected Q-switched performance will exclude Ti:sapphire from consideration. As mentioned earlier, the short upper state lifetime of Ti:sapphire makes it an inefficient energy storage medium. Under gain-switched operation this is no longer a problem and Ti:sapphire must be considered. Comparison of the projected gain switching performance of the vibronic materials will follow in the next section.

In order to decide what material properties are desirable for efficient Q-switched operation of a particular laser medium, it is necessary to consider the equations governing Q-switching performance. The pertinent theory for an oscillator with optimised output coupling was outlined in section 2.3.2. There are three factors to consider; absorption of the pump radiation, efficient energy storage during pumping and energy extraction.

In general absorption will depend on various material properties, but equally on the type of pump source being considered. There is an interplay of various factors here. Basically it is desirable to have as large a gain as possible. This translates into absorbing as much of the

pump radiation within as small a volume as possible. The length of the absorption region is determined by material parameters such as the absorption cross-section and doping level. The doping level can, in some materials, be chosen to achieve a specific absorption length. This is also influenced by the type of pump system being employed; the high divergence of laser diode-pumps often requires short absorption regions, while laser pump sources aren't restrictive in this way. The area of the pump mode is limited by optical damage and saturation considerations. It is particularly important to keep in mind the overlap of the laser mode with the effective gain region created by the pump mode.

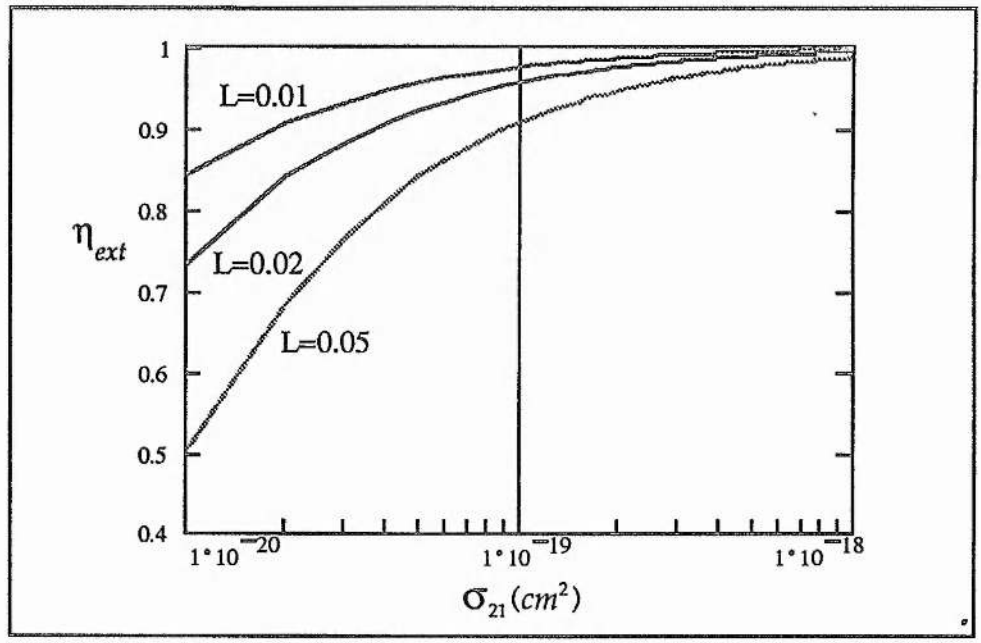

Figure 3.6 is a plot of Q-switched extraction efficiency as a function of stimulated emission cross-section, all other parameters being equal. The different curves are for increasing cavity losses.

Efficient storage of the pump energy has been discussed previously and is expressed in equation (2.1.48). From this expression it is clear that a good matching of the pump duration with the upper state lifetime is required for efficient energy storage in a Q-switched system. The question of energy extraction is encapsulated in equations (2.3.21) and (2.3.32). The energy extraction efficiency as a function of stimulated emission cross-section and parasitic losses is depicted graphically in Figure 3.6. This extraction efficiency is basically the ratio of the output energy, as given by equation (2.3.21), to the useful stored energy which is given by

$$E_u = n_i A l h\nu_l \qquad (3.4.1)$$

This is obtained from equations (2.1.53) and (2.1.54) with the substitution $E_u = \eta\eta_{st}E_{in}$. From Figure 3.6 it is clear that efficient energy extraction is enhanced by a large stimulated emission cross-section and small parasitic intracavity losses.

Equation (2.3.22) for the optimised pulse duration is also minimised for larger emission cross-sections. The effect of intracavity parasitic losses on the pulse duration is more subtle and is depicted in Figure 3.7 in which it is seen that for a given stimulated emission cross-section there is a unique parasitic loss which leads to a minimum duration of the extracted pulse. Obviously everything is usually done to minimise the parasitic losses in order to achieve efficient energy extraction. In real Q-switched lasers it is difficult to limit the parasitic losses to less than a few percent. The design flexibility which laser engineers do have in order to minimise the pulse duration is associated with the cavity length.

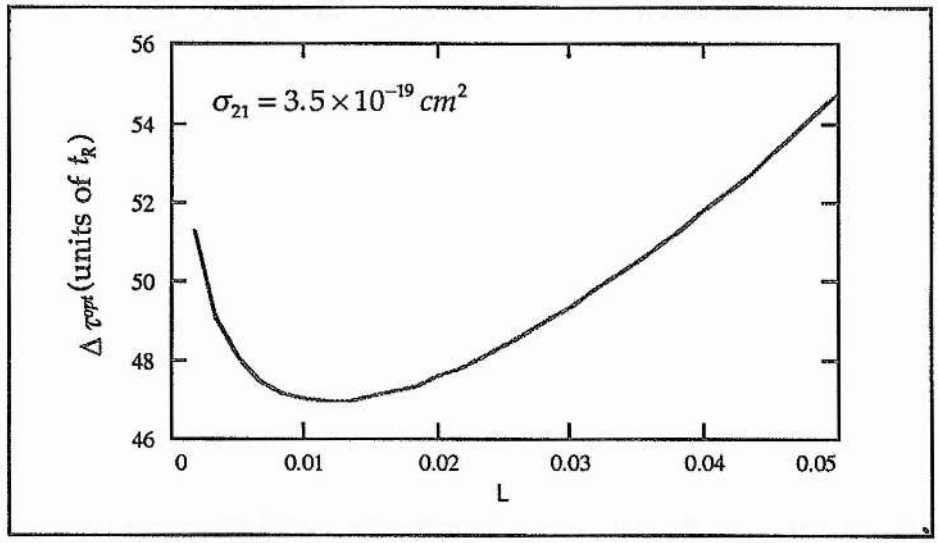

Figure 3.7 A graph illustrating the effect of the parasitic losses on the duration of the extracted Q-switched pulse. The pulse duration (in units of cavity round trip time) is shown to have a unique minimum for a given emission cross-section.

Cr:LiCAF and Alexandrite have low emission cross-sections and for this reason, efficient, rapid extraction when Q-switching or amplifying is difficult. The high saturation intensity required for efficient pulse extraction with these materials may also lead to optical damage, thus restricting the peak power of Q-switched pulses. The higher emission cross-section of

Cr:LiSAF would appear to hand it the advantage. This becomes even more important (see Figure 3.6) when tuning and line-narrowing are contemplated, as these generally require the insertion of lossy intracavity elements. Even accounting for the reduced stimulated emission cross-section, by taking account of excited state absorption, Cr:LiSAF would still appear to be superior in this regard. This advantage is enhanced by the much broader emission bandwidth of Cr:LiSAF.

The fact that Cr:LiSAF and Cr:LiCAF can accept high doping levels without compromising crystal quality is favourable for the reasons described above regarding absorption. This is also beneficial when diode-pumping is considered.

Cr:LiCAF and alexandrite are very similar in terms of their spectroscopic properties and would therefore seem to be in direct competition. As mentioned before, alexandrite has the edge for high power applications, given its power handling capabilities. If good beam quality is essential then Cr:LiSAF with its superior spectroscopic properties is the optimal choice, provided the pump mechanism employed can be made to match well into the 67μs upper state lifetime. These considerations have led to Cr:LiSAF being the medium of choice which has resulted in more effort being expended to improve its quality than that of Cr:LiCAF[45].

In conclusion, considering the analysis of the optimised Q-switch cavity presented above, Cr:LiSAF is seen to dominate in the two critical areas. First and foremost the stimulated emission cross-section is higher which leads directly to more energetic pulses. Secondly, the better crystal quality means that intracavity losses are lower, leading again to more energetic pulses. This also leads to much more rapidly extracted pulses which translates into higher peak powers.

3.5 Comparison of Gain-switching

In the case of gain-switched operation of these vibronic media, Ti:sapphire once again comes into consideration, since gain-switching removes any energy storage deficiencies associated with a short upper state lifetime. The stimulated emission cross-section now becomes the most important spectroscopic property. For this reason, only Cr:LiSAF and Ti:sapphire are considered. Basically the analysis is the same as for the Q-switched operation comparison

except that energy storage is no longer an issue. Ti:sapphire, with a stimulated emission cross-section of nearly ten times Cr:LiSAF, is the ideal vibronic host for gain-switching. Because of its mechanical robustness, it is also perfect for high power applications. Again the large emission cross-section means that the losses associated with tuning and line-narrowing by intracavity dispersive elements are easily overcome.

3.6 Direct Diode-pumping

Ti:sapphire cannot be directly pumped by laser diodes as its pump bands are outwith the emission range of the presently available high-power laser diodes. There are three advantages for Cr:LiSAF and Cr:LiCAF over alexandrite when laser-diode pumping of these vibronic laser media is considered. Firstly, the absorption cross-section for the two polarisations in the fluorides doesn't vary as much, allowing polarisation combination of diode pumps[30] Secondly, the absorption in the 665-675nm range available to red laser diode laser manufacturers is much higher in the two fluoride materials and finally, Cr:LiSAF and Cr:LiCAF can be highly doped, thus enabling short absorption lengths. Thus alexandrite will be dropped as a candidate for diode pumping.

The first example of diode-pumped Cr:LiSAF[37] shows polarisation coupling of two laser diodes and results in highly efficient cw operation. The authors also demonstrated Q-switched operation of diode-pumped Cr:LiSAF. Later Cr:LiSAF was shown to deliver the highest output and efficiency for 1W pump power when compared with Cr:LiCAF under cw, diode-pumped operation[46]. Diode-pumped Cr:LiSAF has also been tuned with a birefringent filter[47]. The losses associated with the intracavity tuner were overcome by utilising a resonant reflector. Stable operation will require active stabilisation of the cavity lengths, thus adding to the complexity.

The high-power red laser diodes currently available for diode-pumping these materials suffer from low brightness. That is, their output is highly divergent and is limited to low powers by facet damage. The traditional solution to this problem is to focus tightly into a highly doped sample. Unfortunately, Cr:LiSAF's low thermal conductivity results in an elevated operational temperature, in such a sample. Even aggressive cooling is insufficient to prevent deleterious thermal quenching from preventing laser operation at moderate powers. An

unsatisfactory fix is found by implementing beam chopping of the pump to reduce the thermal load[48]. Recently a scalable diode-pumping approach has been suggested which will somewhat overcome these thermal limitations. The technique is based on an asymmetric cavity mode. This has the double advantage of reducing the mode-matching constraints on the highly astigmatic diodes and also restricts the heat flow to one-dimension rather than being radial. This improves the efficacy of active cooling of the medium. Scalability lies in being able to increase the length of the emitting area and hence the asymmetry of the mode[49].

Unfortunately the red laser diodes cannot be pulsed to yield higher powers, as is possible with the AlGaAs laser diodes used to pump the Nd-doped laser materials. Recall that laser diodes are essentially continuous wave (cw) devices which operate near their facet damage threshold. This seems to be more restrictive in the case of the red (AlGaInP) laser diodes.

The solution to the thermal problems associated with diode-pumping Cr:LiSAF may be found in the form of the recently reported Cr:LiSGAF (Cr^{3+}:$LiSrGaF_6$). While Cr:LiSGAF has spectroscopic properties very similar to Cr:LiSAF, it seems to be unaffected by the thermal quenching at moderate temperatures which plagues Cr:LiSAF[50]. Furthermore, Cr:LiSGAF has more favourable thermal expansion coefficients which will lead to less inherent strain and a more uniform thermally induced distortion.

3.7 Conclusions

It seems that Cr:LiSAF is a suitable candidate for diode-pumping and operating in Q-switched mode provided high average powers are not required. Line-narrowed operation using intracavity interferometric techniques would also seem feasible provided the gain could be kept high enough. For these reasons it was decided to pursue the development of an all-solid-state, Q-switched, line-narrowed, tuneable Cr:LiSAF laser. In the absence of red laser diodes, a frequency-doubled 1.3μm Nd:YLF laser was constructed to be used as a diode-laser pump substitute. The Cr:LiSAF laser is discussed in the chapter subsequent to the following chapter in which the design, construction and performance of this pump laser is described.

Because a Q-switched Nd:YLF laser was used as the pump source for the Cr:LiSAF laser, this became a gain-switched system. From the discussion in this chapter it is clear that the

vibronic material best suited to gain-switched operation is Ti:sapphire. It was therefore decided that a Ti:sapphire version of the above laser would also be constructed. This would afford an invaluable comparison of the performance of the two lasers to be made. In particular, the performance of the Cr:LiSAF in this configuration could be gauged against that of the well established Ti:sapphire medium. The Ti:sapphire laser will be described in the chapter following the chapter in which the Cr:LiSAF laser is described.

References

[1] P.Albers, E.Stark and G. Huber, "Continuous-wave laser operation and quantum efficiency of titanium-doped sapphire", *J. Opt. Soc. Am.*, **B3**, (1986), p134

[2] J.C. Walling, O.G. Peterson, H.P. Jenssen, R.C. Morris, and E.W. O'Dell, "Tunable alexandrite lasers", *IEEE J. of Quant. Elec.*, **QE-16**, (1980), p1302

[3] J. Hecht, "Tunability makes vibronic lasers versatile tools", *Laser Focus World*, **Oct.**, (1992), p93

[4] R.Scheps, J.F. Myers T.R. Glesne and H.B. Serreze, "Monochromatic end-pumped operation of an alexandrite laser", *Opt. Comm.*, **97**, (1993), p363

[5] J.C. Walling, D.F. Heller, H. Samelson, D.J. Harter, J.A. Pete and R.C. Morris, "Tunable Alexandrite Lasers: Development and Performance", *IEEE J. of Quant. Elec.*, **QE-21**, (1985), p1568

[6] M.L. Shand, J.C. Walling and H.P. Jenssen, "Ground State Absorption in the Lasing Wavelength Region of Alexandrite: Theory and Experiment", *IEEE J. of Quant. Elec.*, **QE-18**, (1982), p167

[7] M.L. Shand and J.C. Walling, "Excited-State Absorption in the Lasing Wavelength Region of Alexandrite", *IEEE J. of Quant. Elec.*, **QE-18**, (1982), p1152

[8] P.F. Moulton "New developments in solid state lasers", *Laser Focus* , May, (1983), p83

[9] P.F. Moulton, "Spectroscopic and laser characteristics of Ti:Al_2O_3", *J. of Opt. Soc. Am. B*, **B3**, (1986), p125

[10] P. Lacovara, L. Esterowitz and M. Kokta, "Growth, Spectroscopy, and Lasing of Titanium-doped Sapphire", *IEEE J. of Quant. Elec.*, **QE-21**, (1985), p1614

[11] P.A. Schulz, "Single-Frequency Ti:Al_2O_3 Ring Laser", *IEEE J. of Quant. Elec.*, QE-24, (1988), p1039

[12] G.F. Albrecht, J.M. Egglestone and J.J. Ewing, "Measurements of Ti^{3+}:Al_2O_3 as a lasing material", *Opt. Comm.*, 52, (1985), p401

[13] A. Sanchez, R.E. Fahey, A.J. Strauss and R.L. Aggarwal, "Room-temperature continuous-wave operation of a Ti:Al_2O_3 laser", *Opt. Lett.*, 11, (1986), p363

[14] G.T. Maker and A.I. Ferguson, "Ti:sapphire laser pumped by a frequency-doubled diode-pumped Nd:YLF laser", *Opt. Lett.*, 15, (1990), p375

[16] W. Vassen, C. Zimmermann, R. Kallenbach and T.W. Hänsch, "A frequency-stabilised titanium sapphire laser for high-resolution spectroscopy", *Opt. Comm.*, 75, (1990), p435

[17] J.M. Egglestone, L.G. DeShazer and K.W. Kangas, "Characteristics and Kinetics of Laser-Pumped Ti:Sapphire Oscillators", *IEEE J. of Quant. Elec.*, QE-24, (1988), p1009

[18] P. Brockman, C.H. Bair, J.C. Barnes, R.V. Hess and E.V. Browell, "Pulsed injection control of a titanium-doped sapphire laser", *Opt. Lett.*, 11, (1986), p712

[19] N.P. Barnes, J.A. Williams, J.C. Barnes and G.E. Lockard, "A Self-injection Locked, Q-Switched, Line-narrowed Ti:Al_2O_3 Laser", *IEEE J. of Quant. Elec.*, QE-24, (1988), p1021

[20] W.R. Rapoport and C.P. Khattak, "Titanium sapphire laser characteristics", *Appl. Opt.*, 27, (1988), p2677

[21] G.A. Rines and P.F. Moulton, "Performance of gain-switched Ti:Al_2O_3 unstable-resonator lasers", *Opt. Lett.*, 15, (1990), p434

[22] T.D. Raymond and A.V. Smith, "Injection-seeded titanium-doped-sapphire laser", *Opt. Lett.*, 16, (1991), p33

[23] C.E. Hamilton, "Single-frequency, injection-seeded Ti:sapphire ring laser with high temporal precision", *Opt. Lett.*, 17, (1992), p728

[24] J.C. Barnes, N.P. Barnes, L.G. Wang and W. Edwards, "Injection Seeding II: Ti:Al_2O_3 Experiments", *IEEE J. of Quant. Elec.*, QE-29, (1993), p2685

[25] A.J.W. Brown, C.H. Fisher and K.W. Kangas, "Efficient, high-energy, narrow-band, blue-light source", *Opt. Lett.*, 18, (1993), p1177

[26] R.L. Aggarwal, A. Sanchez, R.E. Fahey and A.J. Strauss, "Magnetic and optical measurements on Ti:Al_2O_3 crystals for laser applications: Concentration and absorption cross section of Ti^{3+} ions", *Appl. Phys. Lett.*, 48, (1986), p1345

[27] M.D.Perry, "Cr:LiSAF", *Data Sheet 2002*, (1992), Lightning Optical Corporation, Tarpon Springs, Florida, USA

[28] A.J. Henderson *private communication*, Science and Engineering Services Incorporated, Burtonsville, MD 20866, U.S.A.

[29a] S.A. Payne, L.L. Chase and G.D. Wilke, "Optical spectroscopy of the new laser materials $LiSrAlF_6:Cr^{3+}$ and $LiCAlF_6:Cr^{3+}$", *I. of Lumin.*, 44, (1989), p167

[29] S.A. Payne, L.L. Chase, H.W. Newkirk, L.K. Smith and W.F. Krupke, "$LiCAlF_6:Cr^{3+}$: A Promising New Solid-State Laser Material", *IEEE J. of Quant. Elect.*, QE-24, (1988), p2243

[30] R. Scheps, "Cr:$LiCAF_6$ Laser Pumped by Visible Laser Diodes", *IEEE J. of Quant. Elect.*, QE-27, (1991), p1968

[31] S.A. Payne, L.L. Chase, L.J. Atherton, J.A. Caird, W.L. Kway, M.D. Shinn, R.S. Hughes and L.K. Smith, "Properties and performance of the $LiCAF_6:Cr^{3+}$ laser material", *SPIE Solid State Lasers*, 1223 (1990), p84

[32] H.W.H. Lee, S.A. Payne and L.L. Chase, "Excited-state absorption of Cr^{3+} in $LiCaAlF_6$: Effects of asymmetric distortions and intensity selection rules", *Phys. Rev. B*, **B39**, (1989), p8907

[33] M. Stadler, M. Bass and B.H.T. Chai, "Thermal quenching of fluorescence in chromium-doped fluoride laser crystals", *J. Opt. Soc. Am.*, **B9**, (1992), p2271

[34] L.L. Chase and S.A. Payne, "New Tunable solid-state lasers Cr^{3+}:$LiCaAlF_6$ and Cr^{3+}:$LiSrAlF_6$", *Opt. and Phot. News*, **August**, (1990), p16

[35] B.W. Woods, S.A. Payne, J.E. Marion, R.S. Hughes and L.E. Davis, "Thermomechanical and thermo-optical properties of the $LiCAF_6:Cr^{3+}$ laser material", *J. Opt. Soc. Am.*, **B8**, (1991), p970

[36] S.A. Payne, L.L. Chase, L.K. Smith, W.L. Kway and H.W. Newkirk, "Laser performance of $LiSrAlF_6:Cr^{3+}$, *J. Appl. Phys.*, **66**, (1989), p1051

[37] R. Scheps, J.F. Myers, H.B. Serreze, A. Rosenburg, R.C. Morris and M. Long, "Diode-pumped Cr:LiSrAlF$_6$ laser", *Opt. Lett.*, **16**, (1991), p820

[38] M.D. Perry, S.A. Payne, T. Ditmire, R. Beach, G.J. Quarles, W. Ignatuk, R. Olson and J. Weston, "Better materials trigger Cr:LiSAF laser development", *Laser Focus World*, **September**, (1993), p85

[39] S.A. Payne, W.F. Krupke, L.K. Smith, W.L. Kway, L.D. DeLoach, and J.B. Tassano, "752nm Wing-Pumped Cr:LiSAF Laser", *IEEE J. of Quant. Elect.*, **QE-28**, (1992), p1188

[40] D.J. Harter, J. Squier and G. Mourou, "Alexandrite-laser-pumped Cr^{3+}:LiSrAlF$_6$, *Opt. Lett.*, **17**, (1992), p1512

[41] M. Stadler, B.H.T. Chai and M. Bass, "Flashlamp pumped Cr:LiSrAlF$_6$ laser",, *Appl. Phys. Lett.*, **58**, (1991), P216

[42] P. Beaud, Y.-F. Chen, B.H.T. Chai and M.C. Richardson," Gain properties of LiSrAlF$_6$:Cr^{3+}, *Opt. Lett.*, **17**, (1992), p1064

[43] W.R. Rapoport, "Excited-State Absorption and Upconversion in Cr:LiSAF", *OSA Proc. Adv. Solid State Lasers*, **13** (1992), p21

[44] F. Hanson, C. Bendall and P. Poirier, "Gain measurements and average power capabilities of Cr^{3+}:LiSrAlF$_6$, *Opt. Lett.*, **18**, (1993), p1423

[45] Lightning Optical Corporation, Licensee for manufacture of Cr:LiCAF and Cr:LiSAF, Tarpon Springs, Florida, USA

[46] R. Scheps, "Cr-doped solid state laser pumped by visible laser diodes", *Opt. Materials*, **1**, (1992), p1

[47] Q. Zhang, G.J. Dixon, B.H.T. Chai and P.N. Kean, "Electronically tuned diode-laser-pumped Cr:LiSrAlF$_6$, laser", *Opt. Lett.*, **17**, (1992), p43

[48] F. Balembois, P. Georges and A. Brun, "Quasi-continuous-wave and actively mode-locked diode-pumped Cr^{3+}:LiSrAlF$_6$ laser", *Opt. Lett.*, **18**, (1993), p1731

[49] D. Kopf, J. Aus der Au, U. Keller, G.L. Bona and P. Roentgen, "400-mW continuous-wave diode-pumped Cr:LiSAF laser based on a power-scalable concept", *Opt. Lett.*, **20**, (1995), p1782

[50] L.K. Smith, S.A. Payne, W.L. Kway, L.L. Chase and B.H.T. Chai, "Investigation of the Laser Properties of Cr^{3+}:$LiSrGaF_6$", *IEEE J. of Quant. Elect.*, QE-28, (1992), p2612

CHAPTER 4

Nd:YLF PUMP LASER DEVELOPMENT

4.1 Introduction

In the previous chapter the performance of the various vibronic media was compared for pulsed, tuneable operation. Two materials, namely Cr:LiSAF and Ti:sapphire, were isolated as suitable candidates for further investigation. Specifically, they were found to occupy two distinct niches. Cr:LiSAF recommended itself as a vibronic medium which can be directly diode-pumped. It therefore offers the opportunity of realising a compact Q-switched, tuneable laser. While Ti:sapphire is best pumped by another laser, its large stimulated emission cross-section means that as a gain-switched tuneable laser, it should exhibit the best performance of the vibronic media. At the time of these considerations regarding suitable vibronic media, red laser-diodes of sufficient power were not available. It was therefore decided that a frequency-doubled 1.3μm Nd:YLF laser should be constructed to simulate pumping by red laser-diodes. In the interest of maintaining high efficiency it was decided that the Nd:YLF laser would be Q-switched and that the Cr:LiSAF laser would be gain-switched. Q-switching the pump laser would ensure efficient frequency doubling, while gain-switching Cr:LiSAF would overcome the mismatch of the upper state lifetimes of Cr:LiSAF and Nd:YLF.

The Nd:YLF pump lasers will be described in the following section. Although much work has been done within this Department on Q-switched, diode-pumped 1μm Nd-doped lasers[1,2], the operation of these lasers on the 1.3μm transition is quite novel[3,4]. For this reason, the development of the 1.3μm system and its frequency doubling will be described in detail, while the 1μm system will be described briefly at the end of this chapter.

4.2 The 1.321μm Nd:YLF laser

4.2.1 Introduction

Although transitions in the 1.3μm spectral region are important for the fibre-communications industry, there has been relatively little activity regarding these transitions in the well

established laser materials like Nd:YLF and Nd:YAG. While there have been a few reports of laser operation at these wavelengths, reliable values of the stimulated emission cross-sections are elusive. Initial reports were based on flashlamp pumped systems and, for Nd:YLF, gave values of $0.6\times10^{-19}cm^2$ for the 1.313μm transition, which is roughly one-sixth of the 1.047μm transition cross-section of $3.7\times10^{-19}cm^2$ [5,6]. The 1.338μm transition in Nd:YAG was quoted as having a slightly larger emission cross-section of about $0.9\times10^{-19}cm^2$ [6]. The emission cross-section at 1.047μm in Nd:YLF is now generally accepted to be about $1.8\times10^{-19}cm^2$ [7]. More recent work on the 1.3μm transitions in Nd:YLF has resulted in an estimate of $0.45\times10^{-19}cm^2$ for the 1.3μm emission cross-sections[8]. The two 1.3μm transitions in Nd:YLF have been found to be very similar in strength [3,8]. Grossman et al. [8] found that in a diode-pumped, acousto-optically Q-switched configuration, Nd:YLF outperformed Nd:YAG on both the 1μm and 1.3μm lines. They found that Nd:YAG tended to operate simultaneously on the adjacent 1.319μm and 1.338μm lines. On the other hand the adjacent 1.3μm lines of Nd:YLF are polarised so that the orientation of the crystal Brewster surfaces can select either for the 1.321μm (π-polarised) transition or the 1.313μm (σ-polarised) transition. A further advantage of Nd:YLF is the reduced thermal lensing compared to Nd:YAG[9]. This becomes an important concern when frequency-doubling which is optimised for high-quality beams. For these reasons Nd:YLF was selected as the medium for the 1.3μm laser to be used as the pump source for Cr:LiSAF.

4.2.2 Initial cavity design and problems

Basic layout

An end-pumped geometry was chosen to facilitate good pump and laser mode overlap within a small volume. This would result in high gain which would enable rapid and efficient Q-switch energy extraction. End-pumping geometries also allow short cavities which further help in achieving pulses of short duration. The initial cavity design is represented schematically in Figure 4.1. The output of a three-bar-stack laser-diode [SDL-3231-A3] operating at either 792nm or 797nm was coupled into the back facet of the Nd:YLF rod using the coupling optic system of Verdún and Chuang[10]. The temperature of the pump-diode was

tuned such that the output wavelength was suited for maximum absorption. This was found to be about 15°C for 792nm emission and about 25°C for 797nm emission. The rear surface of the laser rod was anti-reflection coated at the pump wavelengths. This resulted in 85% of the pump light being coupled into an elliptical spot, approximately 2.3 x 1.6mm in cross-section, just inside the Nd:YLF rod. The Nd:YLF rod was 8mm long and 3.3mm in diameter and was mounted in a water-cooled brass mount. The a-axis rod was oriented such that the incident diode light was polarised parallel to the c-axis. The Neodymium dopant was nominally 1.1% at. wt. giving a peak absorption of >7cm^{-1}. The cavity was formed by a high reflective coating (R≥99.3% at 1.321μm) on the rear surface of the rod and a plane high reflecting (R≥99.8% at 1.321μm) mirror. The cavity was about 20cm long and contained an enhanced polariser and a lithium niobate ($LiNbO_3$) electro-optic Q-switch crystal. The 25mm long Q-switch crystal was AR-coated at 1.3μm on both surfaces and had an insertion loss of 1-2%.

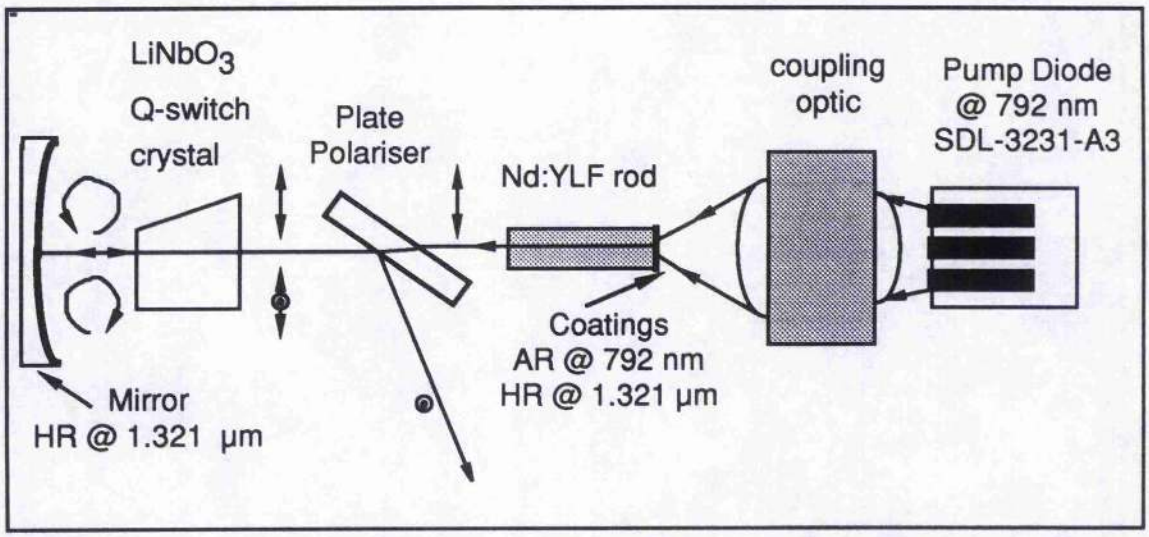

Figure 4.1 Is a schematic of the layout of the first 1.3μm Nd:YLF laser design which was considered. The development of the polarisation of the circulating field is indicated, illustrating the Q-switching technique of polarisation output coupling.

The Q-switching scheme

In this proposed arrangement, the polariser Q-switch combination is used both to implement Q-switched operation and also to provide optimum output coupling. Initially a dc quarter-wave voltage is applied to the lithium niobate crystal, as depicted above. The polariser allows only horizontally polarised fluorescence through the Q-switch crystal. With the dc quarter-

wave voltage applied, the lithium niobate crystal acts as a quarter-wave plate, turning horizontally polarised light into circularly polarised light. This then undergoes a further 180° phase shift, re-entering the lithium niobate crystal as circularly polarised light, but of the opposite sense. This circularly polarised light of the opposite sense then experiences the quarter-wave retardation in travelling through the lithium niobate crystal, emerging as linearly polarised light, polarised at right angles to the light incident on the Q-switch crystal. However, this is just the polarisation which experiences maximum reflection off the polariser and so all the light is essentially coupled out of the cavity, which is therefore in the low-Q state. Q-switching is achieved by applying a voltage pulse of the opposite potential to the dc quarter-wave voltage. This negates the effect of the dc quarter-wave voltage so that the lithium niobate crystal no longer affects the polarisation of the circulating light, thus switching the resonator to the high-Q state. If the voltage pulse is applied at the end of the pump pulse (i.e. when the stored energy is largest and the gain is thus highest), then a highly energetic, horizontally polarised laser pulse will build up within the resonator. Output is obtained off the polariser by choosing the Q-switching voltage pulse such that it doesn't quite negate the retardation effected by the dc voltage. This means that the back-travelling field exiting the electro-optic crystal will be slightly elliptically polarised, with the vertically polarised portion being effectively coupled out of the cavity off the polariser. In this way the optimum output coupling for a given laser cavity can be achieved by adjusting the Q-switching voltage pulse such that the output power is maximised.

Polariser requirements

This system proved impossible to efficiently implement; the major problem. arising from the high insertion loss of the enhanced polariser. These losses were estimated to be about 5% double-pass. While this may not be a problem for 1μm systems, the lower emission cross-section at 1.3μm is unable to overcome such losses. A general feature of this work on the 1.3μm lines is that the technology for intracavity components is not nearly as advanced as that at 1μm. While air-spaced cube polarisers are available (Litton Airtron) for use at 1.3μm they are prohibitively expensive.

An alternative scheme had to be found for a viable 1.3μm Q-switched source. A solution was found when a microscope slide was inserted into the cavity, at Brewster's angle, as a replacement for the polariser. It was found that the roughly 15% reflection of the vertically polarised light off each uncoated glass surface (see Figure 4.2)[11] was sufficient in a round-trip to prevent laser action when the cavity was in the low-Q configuration, i.e. with the dc quarter-wave voltage applied to the lithium niobate crystal. The applied dc voltage required to prevent laser action is termed the holdoff voltage.

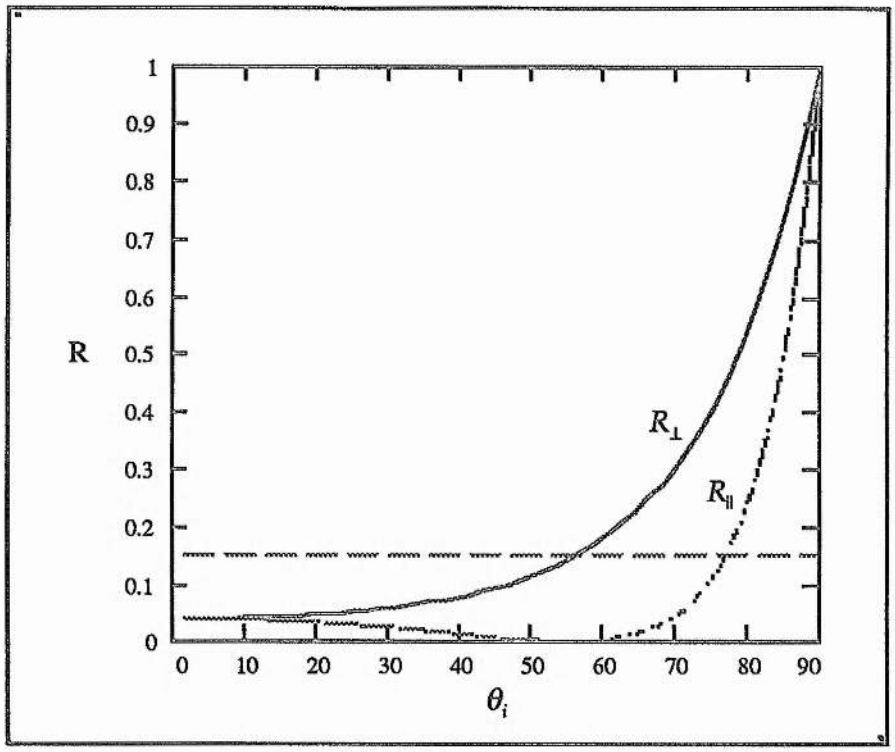

Figure 4.2 Reflectance at a glass (n=1.5) air boundary as a function of incident angle for the two polarisations.

While it was encouraging to obtain laser holdoff using only the losses off an uncoated glass slide, this alone did not guarantee a solution. There were two factors to consider. Firstly, the optical quality of the surfaces of a glass microscope slide are poor in terms of laser requirements. Parasitic losses were of the order of a few percent and may have contributed to achieving holdoff. The glass slide was therefore replaced by an uncoated glass etalon which was of the requisite optical quality (flatness < λ/50 @ 633nm). Secondly, the output could no longer be coupled out of the cavity off this polariser. From Figure 4.2 it is clear that only 15%

of the vertically polarised light may be coupled out from any one surface of the uncoated glass polariser. This means that output would be coupled from both surfaces of the polariser and also in both directions. This problem was overcome by replacing the end mirror with an output coupler.

These developments gave rise to the final configuration of the Q-switched 1.321μm Nd:YLF laser which was frequency-doubled and used to pump a Cr:LiSAF laser. This final configuration is described in detail in the next section.

4.2.3 The Q-switched 1.321μm Nd:YLF laser

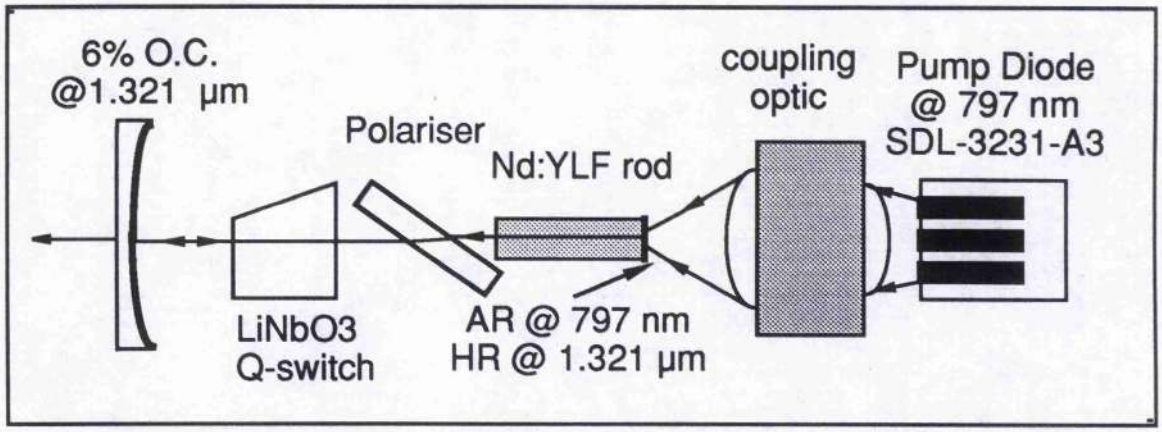

Figure 4.3 A schematic of the final configuration of the 1.3μm Nd:YLF laser. The polariser could be oriented to select either for either of the 1.3μm lines since they are orthogonally polarised.

The final configuration of the Q-switched 1.321μm laser is depicted schematically above in Figure 4.3. The configuration is exactly as described previously except for the polariser and the cavity was shortened to a physical length of 15cm. The polariser is simply an uncoated glass etalon (flatness < λ/50 @ 633nm) oriented at Brewster's angle. This orientation could either be as depicted above, selecting for the π-polarised, 1.321μm transition; or it could be oriented to select for the 1.313μm transition. This would be vertically polarised in the above diagram.

Q-switching implementation

Q-switching could be implemented in a similar fashion to that described in the previous section. If a quarter-wave dc voltage of about 1.65kV was applied to the lithium niobate electro-optic crystal, the field exiting the crystal after a double pass would again be vertically polarised. Since the polariser was now an uncoated glass etalon at Brewster's angle, only 14.8% would be coupled out per surface, (see Figure 4.2). This implies 27.4% in a single pass which becomes a 47.3% loss for vertically polarised light in the resonator. The situation becomes more complicated on the second pass as the surviving vertically polarised light is returned to the polariser with horizontal polarisation and thus passes through unimpeded. The accumulated loss off the intracavity Brewster angled surfaces, together with that of the output coupler, is sufficient, for high enough output coupling, to achieve lasing holdoff. Output coupling in this scheme could no longer be optimised by adjusting the Q-switching pulse voltage, but can be achieved by judicious selection of the output coupler. The optimised output coupler for this laser was found to be R=94% @ 1.321μm. The output mirror was chosen with a 10m radius of curvature for optimum pump and laser mode overlap. The selection of the output coupling and the actual Q-switched performance will be described in detail below. Before that the two 1.3μm lines will be compared and the free running performance of the laser will be described.

Comparison of the 1.3μm transitions

As mentioned in section 4.2.1, there have been few reports on the stimulated emission cross-sections of the two 1.3μm lines of Nd:YLF in the literature, with some confusion regarding the relative strength of the transitions. Most reports dealt with the 1.313μm line[5,6]. When the 1.321μm line was mentioned, the relative strength of the emission cross-sections of the two lines was only hinted at as being roughly equal[8]. An attempt was, therefore, made to experimentally determine the ratio of the stimulated emission cross-section of the two transitions. In order to do this, a series of slope efficiency measurements at both transitions were made for a range of flat output couplers. The cavity parameters in each case were left unchanged with only the reorientation of the polariser plate required to select for the

appropriate transition. The Q-switch crystal was removed for these measurements. The slope efficiency measurements which were obtained for a number of output coupler reflectivities ranging from 2% to 15%, are plotted in Figure 4.4. The results for the 1.313μm transition appear in (a) and those for the 1.321μm transition in (b). The cavity was as depicted in Figure 4.3 except there was no Q-switch crystal for these measurements.

The slopes of these graphs appear to display anomalous behaviour according to equation (2.1.57) for the slope efficiency. This equation implies that increased output coupling leads to an increased slope efficiency. This is clearly not the case in Figure 4.4 above where a distinct decline in slope efficiency with increased output coupling is observed. This is evident in most of the slope efficiency curves with high output coupling presented throughout this chapter. This is explained by the fact that for large output coupling the laser is nearer threshold and is therefore not solely on the linear portion of the input-output curve. Only when the laser is operated far above threshold is the true linear portion of the slope efficiency curve accessed[12].

The first measure of the ratio of the emission cross-sections can be obtained from the ratio of the intercepts of these graphs. From equation (2.1.56) it is clear that the intercepts of the output energy versus input energy graphs is given by the product of the threshold energy and the slope efficiency. From equations (2.1.57) and (2.1.58) this product is seen to yield the expression:

$$E_{th}\sigma_s = \frac{\ln R}{2} I_S A \tau_p \qquad (4.2.1)$$

Where equation (2.1.54) has been used for K'. Using equation (2.1.34) to substitute for the saturation intensity I_S yields the expression

$$E_{th}\sigma_s = \frac{\ln R}{2} \frac{hc}{\lambda_l \sigma_{21} \tau_f} A \tau_p \qquad (4.2.2)$$

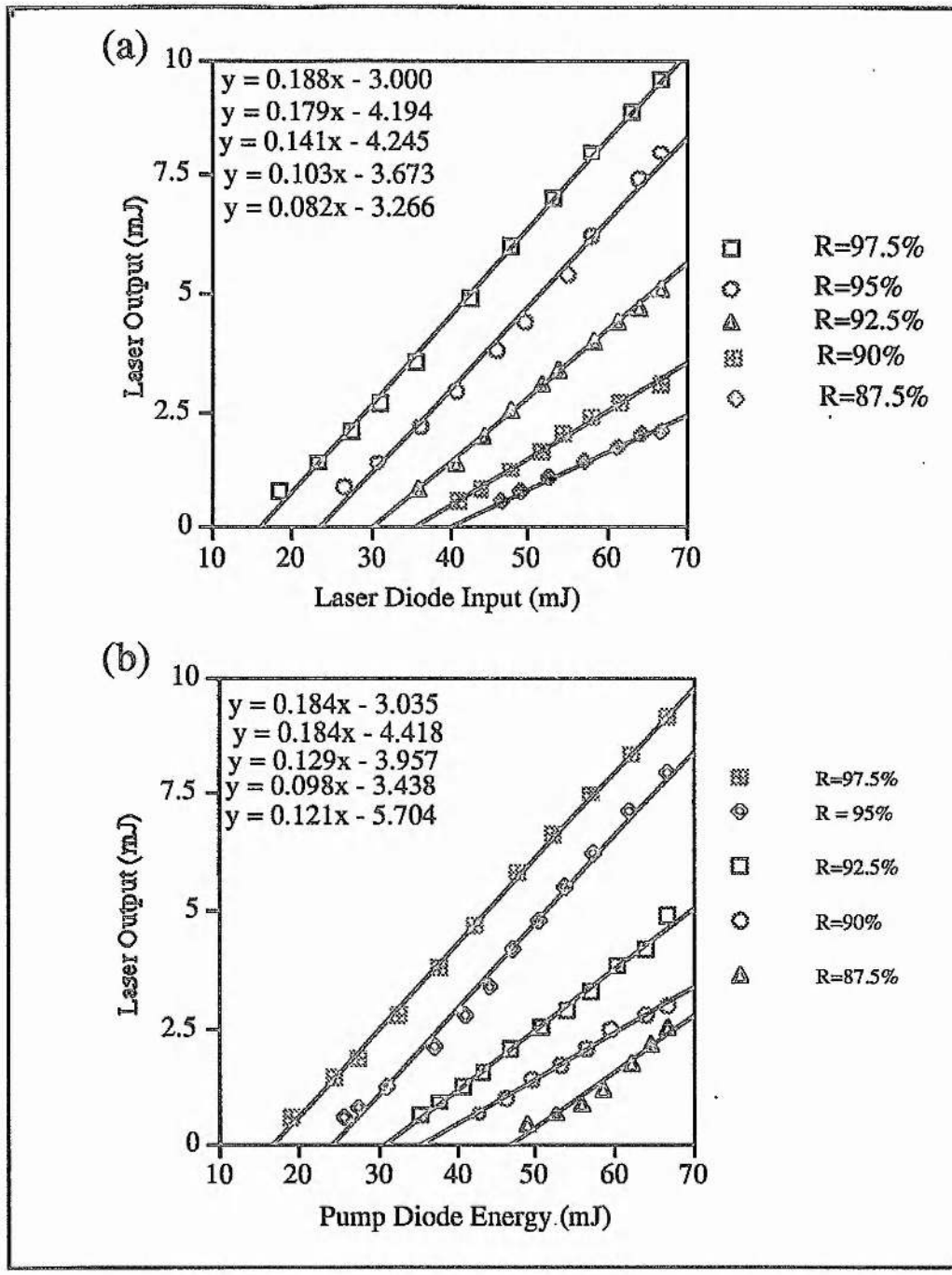

Figure 4.4 Long pulse operation slope efficiency measurements of the 1.3μm laser operating (a) on the 1.313μm line and (b) on the 1.321μm line. The laser cavity did not contain a Q-switch crystal.

In the case when operation on the two lines is selected only by reorienting the polariser, most of the factors are common for the two lines. Thus the ratio of the intercepts of the slope efficiency graphs of the two lines for a given output coupler is given by

$$\frac{(E_{th}\sigma_s)_{1.321}}{(E_{th}\sigma_s)_{1.313}} = \frac{(\lambda_l\sigma_{21})_{1.313}A_{1.321}}{(\lambda_l\sigma_{21})_{1.321}A_{1.313}} \tag{4.2.3}$$

Provided the beam areas can be assumed to be roughly the same, the ratio of the emission cross-sections can be expressed as

$$\frac{(\sigma_{21})_{1.313}}{(\sigma_{21})_{1.321}} = \frac{1.313}{1.321}\frac{(E_{th}\sigma_s)_{1.321}}{(E_{th}\sigma_s)_{1.313}} \tag{4.2.4}$$

The assumption of similar beam areas was found to be valid. Measurement of beam areas is discussed in a later section. The intercepts from the graphs appearing in Figure 4.4 for different output couplers can now be used to estimate the ratio of the cross-sections. The value for the 10% output coupler was not used as it appears to be inconsistent. That is, its slope is expected to be somewhere between the slopes obtained with the slightly smaller and slightly larger output coupler. The ratio of the emission cross-sections by this method is

$$\frac{(\sigma_{21})_{1.321}}{(\sigma_{21})_{1.313}} = 0.97 \pm 0.06 \tag{4.2.5}$$

A second measure of this ratio can be obtained from a Findlay-Clay analysis[13] of the two lasers. It is possible to perform a Findlay-Clay analysis, as described by equation (2.1.60), by plotting the pump threshold versus the negative logarithm of the output coupler reflectivity. This is valid for all values of the output coupling provided that the losses are kept low. This assumption holds true for all the systems considered in this work. The results are plotted in Figure 4.5 from which it can be seen that they have very similar slopes. In each case the slope is given by 2K' (see equation (2.1.60)), which is given by equation (2.1.54) or

$$K' = \frac{\eta\sigma_{21}\lambda_l\tau_f}{hcA\tau_p} \tag{4.2.6}$$

Equation (2.1.34) has been used to substitute for the saturation intensity I_S. This factor provides information about the gain as expressed by equation (2.1.53). By taking the ratio of the slope at each wavelength, the ratio of the cross-sections could be obtained,

$$\frac{K_1'}{K_2'} = \frac{\eta_1'\sigma_1 A_2}{\eta_2'\sigma_2 A_1} \tag{4.2.7}$$

Here $\eta_i' = \eta_i / \eta_S$ represents all of the efficiency terms, as defined by equation (2.1.52) and discussed in section (2.1.4), divided by the Stokes efficiency factor. The ratio is therefore independent of operational wavelength. The subscripts 1 and 2 refer to the different wavelengths of operation, 1.321μm and 1.313μm, respectively. The A_i are the respective beam areas and the σ_i are the respective stimulated emission cross-sections.

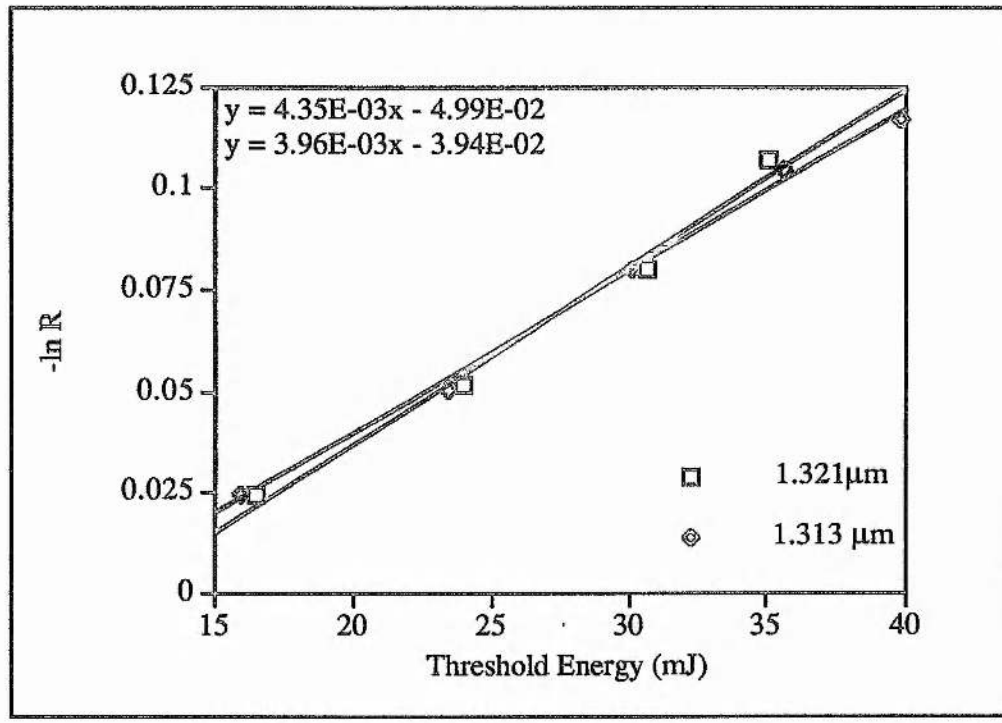

Figure 4.5 Results of the Findlay-Clay measurements of the 1.321μm and 1.313μm lines in Nd:YLF, illustrating the similarity in slope from which their respective emission cross-sections may be deduced to be almost equal.

The efficiency term may be assumed to be the same in each case, since only the polariser was reoriented to discriminate between the two transitions. Any differential loss accounted for by the insertion of the polariser to select for the two lines will not affect the slope, but instead will appear as a difference in the intercept. By scanning pinhole measurements it was found that the beam areas were much the same in each case for a given output coupler. As mentioned before, these beam measurements will be described in more detail in a subsequent section. Substitution of the slopes of the Findlay-Clay measurements reproduced in Figure 4.5, into equation (4.2.7) indicates that the cross-sections for the 1.321μm and 1.313μm

transitions are equal to within 10%. This is in agreement with the result of equation (4.2.5) which was determined by a method independent of the efficiency factors.

It is worth noting that a similar comparison could be carried out between the 1μm lines and the 1.3μm lines. If the rear surface of the Nd:YLF crystal could be coated to be highly reflecting at both 1μm and 1.3μm, then operation in either of these regions could be achieved with the appropriate output coupler. The specific line could once again be polarisation selected. In this way the conversion of the pump into a useful small signal gain (see equations (2.1.52 & 53)), will be the same in both cases. A Findlay-Clay measurement at any two lines will therefore differ in slope by the ratio of the cross-sections as indicated by equation (4.2.7). The first method described above for measuring this ratio is more difficult to apply in this case as it requires accurate knowledge of the output coupling.

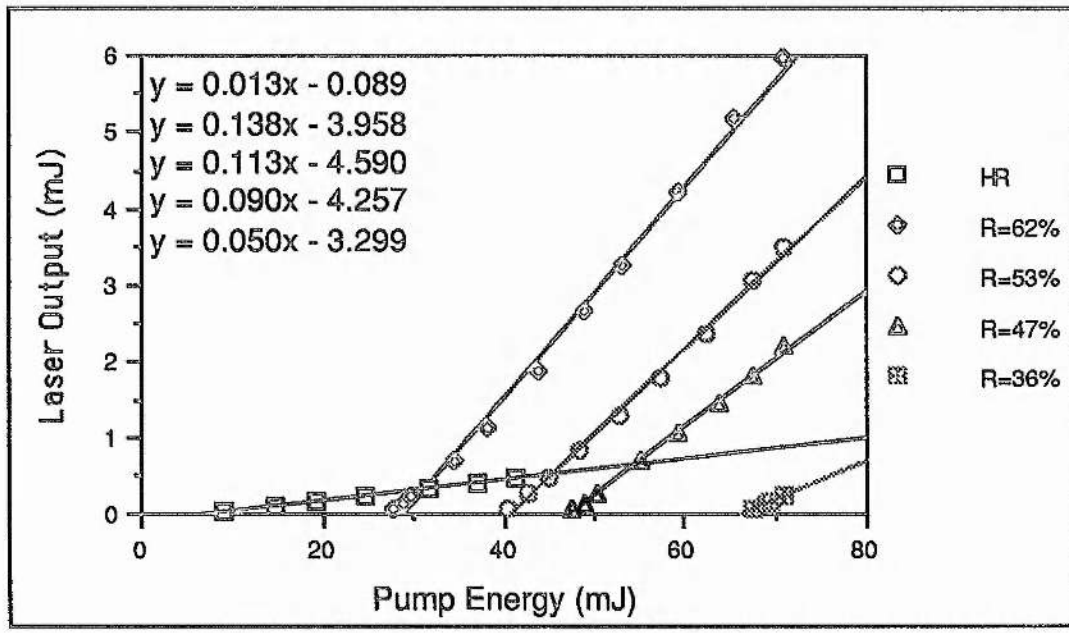

Figure 4.6 Long pulse operation slope efficiency measurements of the 1μm Nd:YLF laser. The laser cavity did not contain a Q-switch crystal.

A more crude comparison was carried out using results which were not intended for this purpose. The crudeness in the measure obtained, results from the fact that different Nd:YLF crystals were used for the two wavelengths. After the development of the 1.3μm laser, a 1μm version was constructed as a pump source for the Ti:sapphire laser. The same pump-diode and coupling optics were used, but the Nd:YLF crystal was different. Assuming that the

crystal was long enough to permit maximum absorption of the pump light, similar absorption efficiencies may be expected. With this assumption the overall efficiency in converting pump light to useful population inversion are expected to be similar for the two systems. The slope efficiency measurements for this laser operating on the 1.047μm line are reproduced graphically in Figure 4.6.

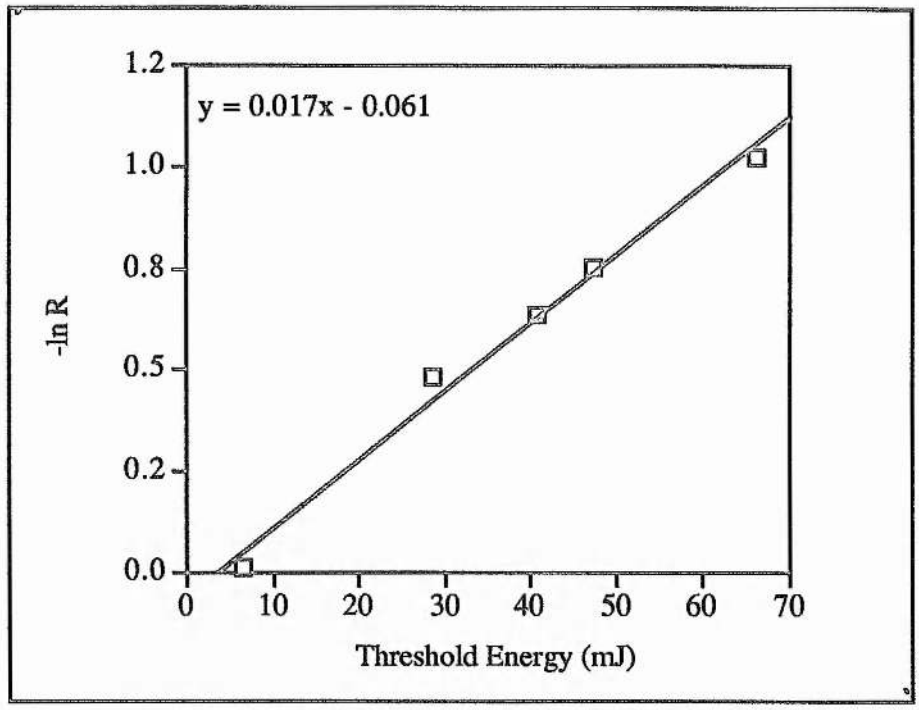

Figure 4.7 Results of the Findlay-Clay measurement of the 1.047μm line in Nd:YLF under long pulse operation.

A Findlay-Clay analysis of this laser was then performed using the above results. The relevant graph is plotted below in Figure 4.7. The slope of the Findlay-Clay plot can then be substituted, together with the slope in Figure 4.5 of the Findlay-Clay plot for either of the 1.3μm transitions, into equation (4.2.7). Although the efficiency factors are expected to be different due to the different crystals, they are assumed not to differ too severely, as mentioned earlier. The final assumption required before a ratio of the stimulated emission cross-sections is obtained, concerns the relative sizes of the laser mode area. Again the assumption is that they do not drastically differ. Since a plane/plane cavity was employed, the laser mode was assumed to be determined by the pump mode area which was the same for both lasers. In this manner a ratio of emission cross-sections of

$$\frac{\sigma_{1.047}}{\sigma_{1.321}} \approx 3.9 \qquad (4.2.8)$$

is obtained. This is in keeping with the earlier reported value of Grossman et al.[8], as mentioned in section 4.2.1.

Polarisation flipping behaviour

An interesting observation was made early on in the development of the 1.3μm laser. When there was no polarisation selective element in the laser cavity, it was found that either of the two laser transitions (π-polarised or σ-polarised) could still be selected. This behaviour was first reported in 1μm Nd:YLF lasers by Cerullo et al.[14] and subsequently by Frei and Balmer[15]. During construction of the Q-switched 1μm laser this observation was confirmed. In the plane/plane resonator of the 1.3μm laser, it was observed that by tilting the output coupler away from the optimum output energy location enabled the selection of either the π-polarised line at 1.321μm or the σ-polarised line at 1.313μm to be effected. When the cavity alignment was optimised for optimum output power, the laser was found to operate on both 1.3μm lines simultaneously. The explanation proffered by Frei and Balmer[15] is that the two transitions see different thermal lensing powers. So tilting the output coupler results in the cavity becoming unstable for one of the transitions while for the other it is still stable.

Free running laser performance

The free running or long-pulsed operating performance of this laser is summarised by the slope efficiency measurements reproduced in Figures 4.4 (b) and 4.8. Figure 4.4 (b) indicates the long pulse performance for a range of output couplers when there was no Q-switch crystal in the cavity, while Figure 4.8 contains the results when the Q-switch crystal was in the cavity. The increased threshold and decreased slope efficiency for a given output coupler is evidence of the extra parasitic loss due to the insertion of the lithium niobate Q-switch crystal. In both cases the pulse duration was about 350μs long.

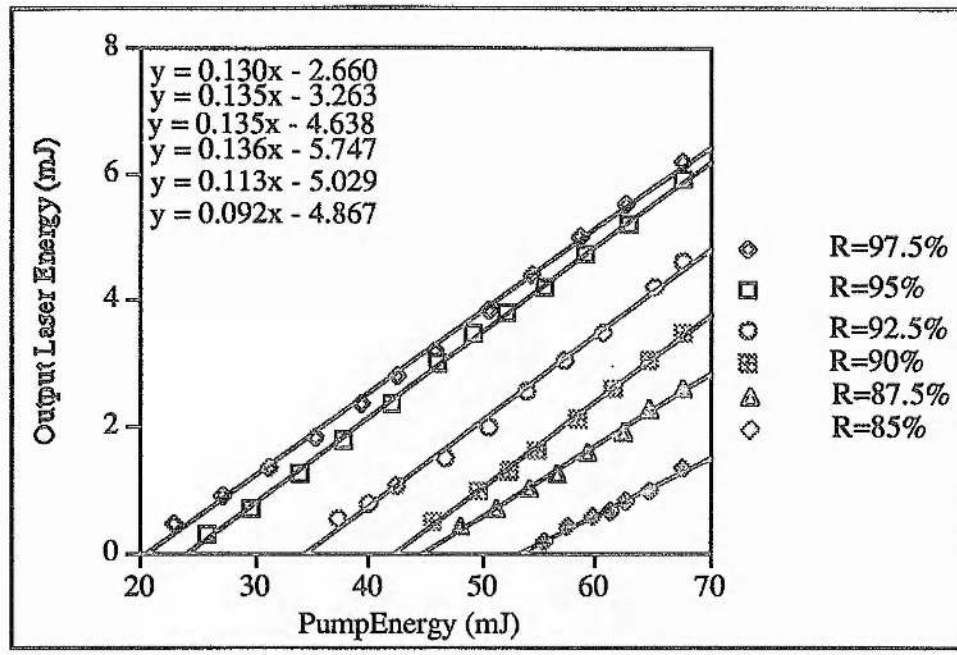

Figure 4.8 Long pulse operation slope efficiency measurements of the 1.321μm Nd:YLF laser with the Q-switch crystal in the laser cavity.

The results plotted in Figure 4.8 above, for the laser operating with the Q-switch crystal, were used to once again perform a Findlay-Clay analysis. The outcome is presented in Figure 4.9. Once again this can be compared with Figure 4.5 which contains the equivalent graph for the laser without the Q-switch crystal inserted. The slopes are seen to agree to within 10% and the losses for the cavity with the Q-switch crystal are higher, as expected.

Optimum performance for the two configurations yielded 9.5mJ output energy for the laser without the Q-switch crystal and 6.2mJ output energy for the laser with the Q-switch crystal inserted. In the first case this performance was obtained with a 2.5% output coupler as indicated in Figure 4.4 (b), while in the case with the Q-switch crystal inserted, similar performance was achieved with both the 2.5% and 5% output couplers as reproduced in Figure 4.8. In comparing these two curves the expected increase in threshold and reduction in slope efficiency for a given output coupling is evident when the electro-optic crystal is inserted. This behaviour is attributed to the extra parasitic loss introduced by the lithium niobate crystal.

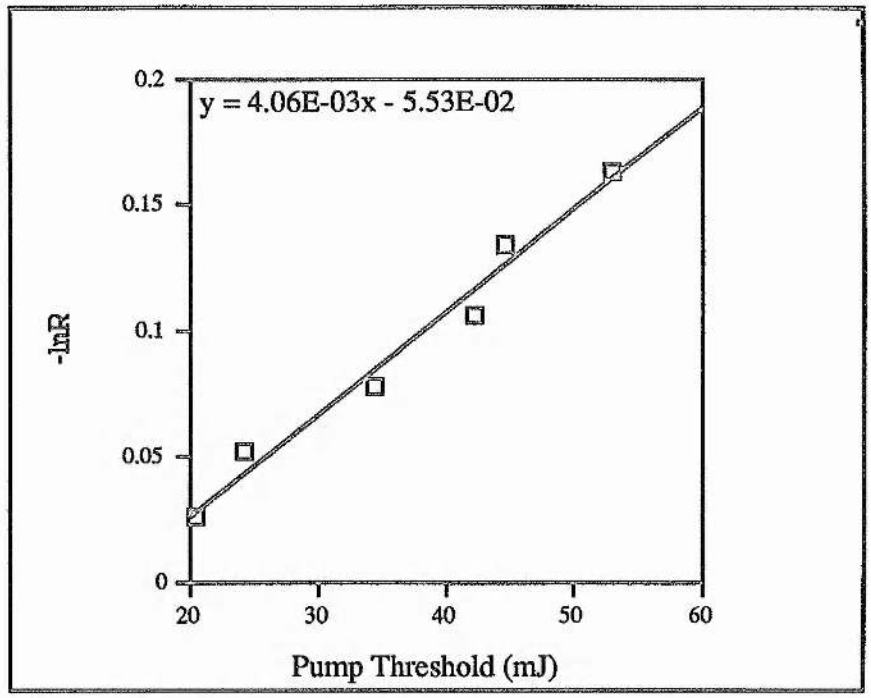

Figure 4.9 Result of the Findlay-Clay measurement on the 1.321μm Nd:YLF laser with the Q-switch crystal in the laser cavity.

As described in section 2.1.5 of the theoretical chapter, the utility of the Findlay-Clay analysis is that the slope and intercept, which quantify the double-pass gain and losses respectively, can be used to determine the optimum output coupling for the laser under either long-pulse operation using equation (2.1.59), or Q-switched operation using equation (2.3.20). Since ultimately Q-switched operation of this laser was desired, the relevant optimum output coupling was determined. The following section concerns the Q-switching performance of the 1.321μm Nd:YLF laser.

Q-switched laser performance

The results of the Findlay-Clay measurements were used to determine the optimum output coupling required for Q-switched operation of this laser. From the slope of Figures 4.5 and 4.9, the unsaturated gain could be determined using equations (2.1.60) and (2.1.53). Under Q-switched operation this will be reduced by the storage efficiency factor (equation (2.1.48)) according to equation (2.3.19). Using a slope of $2K' = 0.0044\text{mJ}^{-1}$, and a storage efficiency factor of $\eta_{st} = 0.7$ yielded an unsaturated double-pass gain of $2g_0 l = 0.22$ for 72mJ of pump

energy. Although the intercept of the Findlay-Clay results inferred parasitic losses of around 5%, a value of roughly 3% was used. This was estimated from the accumulated losses of the system components. This yielded an optimisation parameter of $z \approx 7.3$, using equation (2.3.19). Equation (2.3.20) was then used to estimate the required output coupling for optimised Q-switching performance of this laser. The optimum reflectivity of the output coupler was calculated to be $R_{opt} \approx 93.7\%$.

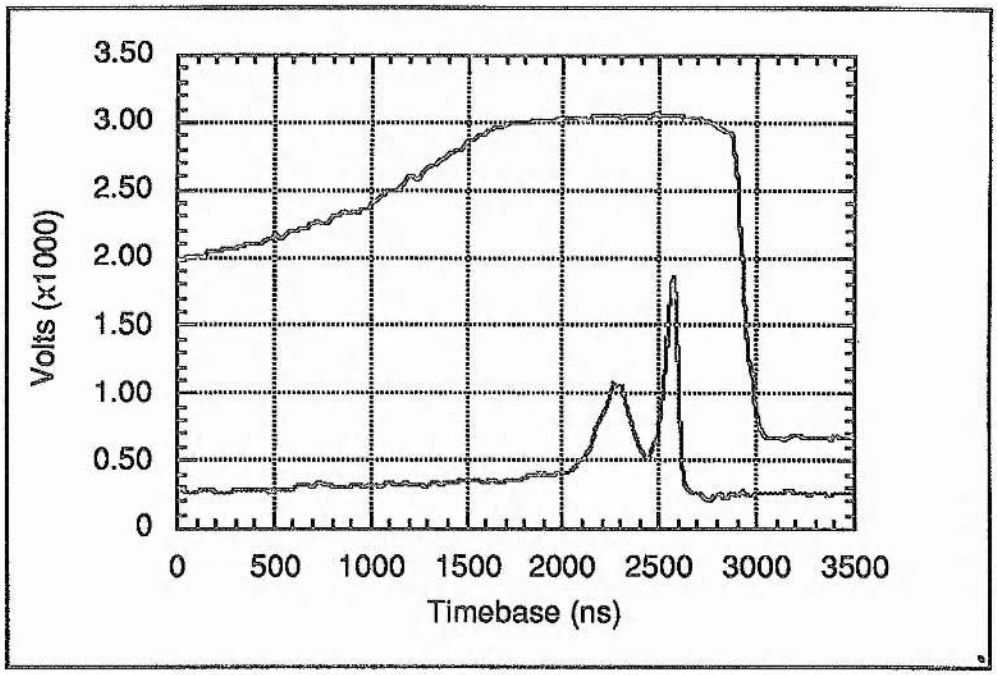

Figure 4.10 The top trace is the voltage pulse applied to the lithium niobate crystal to Q-switch the cavity. The bottom trace, in arbitrary units, is the Q-switched 1.321μm laser output exhibiting postlasing. Both traces are offset from zero for clarity.

A concave (ROC = 10m) 6% output coupler was acquired based on this analysis. The reasons for choosing a concave mirror are discussed in the following section. The actual output coupler used in the final configuration had a 93% reflectivity. The Q-switched performance of the laser with both this output coupler and the 95% reflective plane output coupler was comparable. In each case the laser delivered about 3.5mJ . Holdoff with both these arrangements was achieved with a dc reverse bias voltage of about 1.65kV. Q-switching with the 97.5% reflective output coupler was attempted, but it was not possible to achieve holdoff.

Evidently the combined losses of the polariser and the output coupler were insufficient to prevent lasing even when the quarter-wave voltage was applied to the Q-switch crystal.

It was soon discovered that the Q-switched output of this laser was extracted in a double pulse. A typical example is illustrated in Figure 4.10. This can be understood as a postlasing phenomenon caused by piezooptic effects in the $LiNbO_3$ Q-switch crystal.

Whilst in 1μm systems there is usually enough gain to extract the pulses in under 20ns, the lower gain in the 1.3μm system results in much slower pulse extraction. These longer pulses fall prey to the changing polarisation characteristics, and hence cavity Q, due to the piezooptic "ringing" inherent in $LiNbO_3$[1,16]. This means that the cavity is closed early while the population inversion is still above threshold for the highest Q-state of the cavity. When the cavity again returns to a high-Q state, a postlasing pulse is observed containing the remainder of the energy. The separation of the postlasing pulse from the main pulse could be varied by altering the switching voltage. A typical voltage pulse is reproduced in Figure 4.10, indicating that it is of sufficient duration not to affect the extraction of a pulse of up to 1μs. The voltage of this pulse is about 2.4kV. The postlasing was overcome by increasing the switching voltage applied to the crystal so that the cavity stayed open long enough for all the energy remaining after the first pulse to decay away before the cavity returned to the high-Q state by the piezooptic effect. This decay of energy can be seen as the tail of the Q-switched pulse depicted in Figure 4.11. This is an example of the single Q-switched pulse which was then frequency doubled and used to pump a gain-switched Cr:LiSAF laser. The voltage pulse used to obtain single pulse Q-switched output of this sort was about 2.5kV. The maximum energy which could be extracted in such a single Q-switched pulse was 2.2±0.1mJ (7% fluctuations) and the pulse duration was typically of the order of 75±3ns (4% fluctuations).

With the use of a 1m monochromator (Rank Hilger Monospec 1000), the laser was found to operate on 10 equally spaced longitudinal modes, separated by about 15GHz. However, adjacent cavity modes were spaced roughly 1GHz apart. This aspect of the laser operation is a result of reduced spatial hole burning effects achieved by locating the laser crystal at one of the ends of the cavity. This was discussed in section 2.2.2. The laser operated over a linewidth of 153GHz which is about half of the gain bandwidth of the 1.053μm line[17].

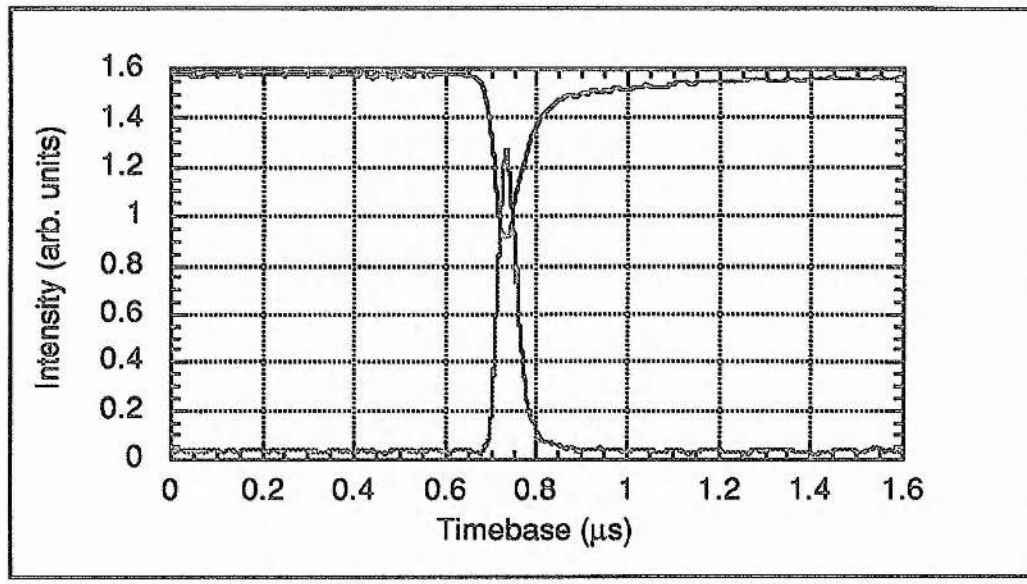

Figure 4.11 The top trace is the Q-switch pulse of 1.321μm laser, while the bottom trace is the resultant frequency-doubled pulse. The long decay tail is evident on the 1.321μm pulse.

Many problems were encountered with damage of the coatings of the lithium niobate Q-switch crystal, with damage occurring well below the specified damage threshold value (>250MW/cm^{-2}). This is further testimony that the coating technology at 1.3μm is not nearly as advanced as that at the more commonly used 1μm. An equivalent 1μm laser might have twice the energy in pulses at least half as long, yet exhibit no optical damage problems. Damage to the Q-switch crystal coatings was a delayed effect, occurring a few days to a few weeks after initial operation of Q-switching. A possible mechanism for this damage is dust. The dc bias applied on the crystal slowly charges the crystal up and the end faces are then able to pick up dust. When dust is located within the beam, it is burnt onto the crystal surface, damaging the coating. As discussed below, the Q-switch in the 1μm laser had no dc bias voltage and this problem was never encountered. In both cases the crystals were located in receded mounts to minimise dust landing on the surfaces. A second possible mechanism for damage to the 1.3μm Q-switch crystal coatings is due to the fact that some multi-layer dielectric coatings contain residual amounts of water which is absorbing at 1.3μm.

Beam profiling

A scanning pinhole set-up was used to measure the beam mode characteristics. A 25μm pinhole was used to scan across beams of the order of 3mm diameter. The pinhole could be scanned both horizontally and vertically. Both the near-field and far-field beam profiles were measured. The far field measurements were made in the image plane of a 20cm focal length lens. In this way the departure of the beam from its diffraction limit could be determined. This is equivalent to the method proposed by[14].

The spatial mode quality of the laser without a Q-switch crystal was measured for operation on both the 1.321μm and the 1.313μm lines. The near field results for a plane/plane cavity with a 2.5% output coupler are reproduced in Figure 4.12 for both the (a) horizontal and (b) vertical beam cross-sections.

The beam waist radii in the horizontal and vertical directions are 1.66 x 0.89mm for 1.313μm operation and 1.6 x 0.86mm for 1.321μm operation. This confirms that the beam areas for laser operation on the two 1.3μm lines are the same within the accuracy of this measurement technique. This assumption was used earlier when the stimulated emission cross-sections of the two 1.3μm lines were compared.

The poor quality of the mode in the horizontal direction is apparent in Figure 4.12 (a). This is attributed to the elliptical nature of the pump mode. The spatial mode of the laser in long pulse operation appears to be a combination of TEM_{00} and TEM_{01} modes.

The spatial mode of the laser was vastly improved when Q-switched operation was implemented and it seems to be much closer to TEM_{00} in nature. It does, however, have poor divergence qualities in the horizontal plane. Under Q-switched operation the laser mode was determined to have beam waist radii in the horizontal and vertical planes of 0.88 mm and 0.59mm with associated M^2 values of 2.7 and 1.3, respectively. The near field horizontal and vertical pinhole scans for a Q-switched pulse appear in Figure 4.13. The horizontal scan clearly illustrates a ridged structure which explains the large departure from diffraction limited divergence. Again this is ascribed to a poor horizontal mode in our pump laser diode. Similar results were obtained with a plane/plane cavity and with a 10m R.O.C. output

coupler. The curved output coupler was used in the final configuration to match the mode size of the plane/plane cavity and to provide added stability.

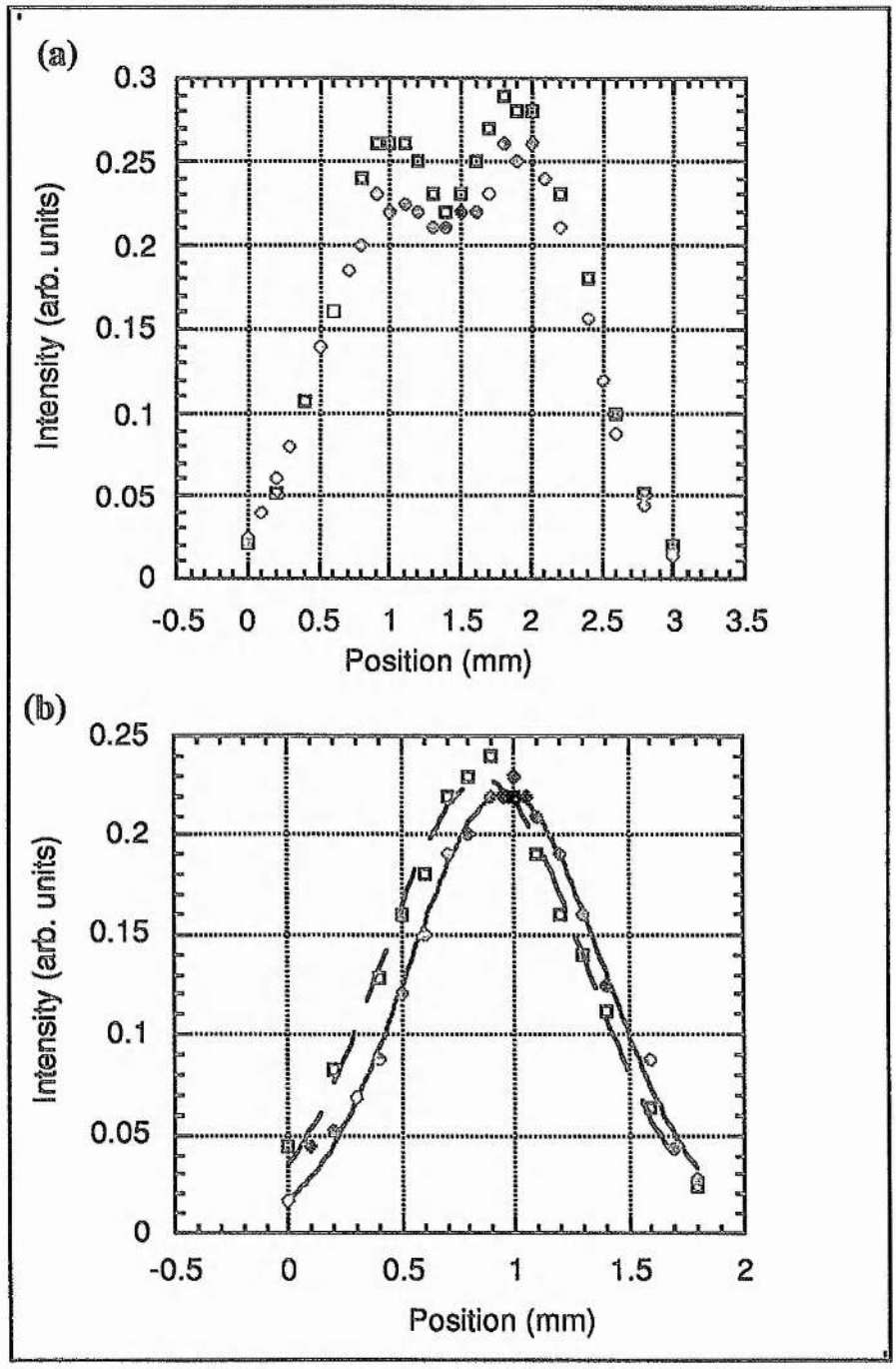

Figure 4.12 (a) Horizontal and (b) vertical intensity distributions of the two 1.3μm lines under long pulse operation. The open squares refer to 1.313μm operation and the filled diamonds refer to 1.321μm operation. The vertical traces are fitted to a Gaussian distribution.

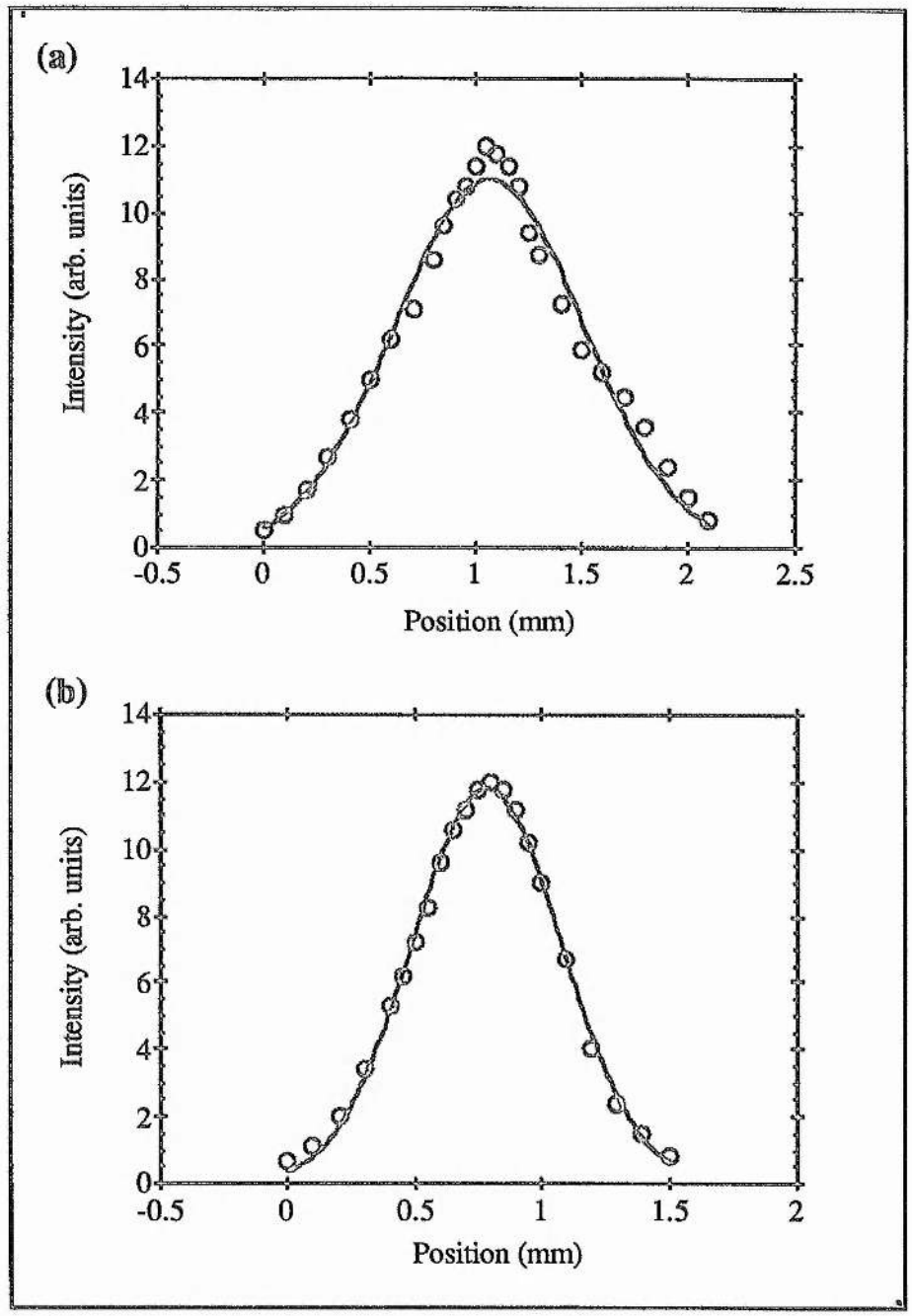

Figure 4.13 Near field (a) Horizontal and (b) vertical beam profiles of the Q-switched 1.321μm laser.

The implications of the different spatial profiles of the laser output for long pulsed and Q-switched operation are discussed in the context of modelling in the following section.

Comparison with theory

Good agreement between the experimental results and theoretical predictions using the results of Chapter 2 was not possible for a number of reasons. Specifically, the theoretical predictions did not compare well with the actual Q-switch performance. The two major reasons are the postlasing phenomenon and the change in laser mode sizes between long pulse and Q-switched operation. Both of these problems have been discussed in the relevant sections presented above.

On the positive side, the predictions did seem to deliver the correct output coupler for optimised operation. As mentioned before, the Q-switch performance with output couplers near the predicted optimum of 6-7% was verified. The 2.5% transmitting mirror had too much feedback and holdoff was not achieved. The 5% OC performed well, but a 93% reflective mirror which was specially ordered for optimum output coupling performed slightly better. The 7.5% OC was also tried, but exhibited poorer performance. Thus experimental evidence suggested that the calculated optimum output coupling was correct, so at least there is confidence in the z-factor used in this calculation, if not its two constituents.

Finally it should be mentioned that in the light of the postlasing problems it would seem to be advantageous to use as high an output coupler as possible, trading off energy extracted for quicker extraction to ameliorate the effects of the piezooptic ringing.

4.3 Frequency-doubling of the 1.321μm Nd:YLF laser

The two well established nonlinear optical (NLO) materials, KTP and LBO, are suitable for frequency doubling in the 1.3μm region. Although KTP had been identified as a possible doubling crystal for 1.3μm radiation as early as 1985[18], not many quantitative studies have appeared in the literature[19-22]. It soon became apparent that a type II phase matching geometry would be the most suitable due to the larger NLO coefficient and increased acceptance angle[20]. The major problem with using KTP was that it was found to have a rather large walkoff angle of about 2.5° for SHG at 1.3μm[22-24]. Nevertheless, a high brightness beam should be efficiently doubled.

The more recently discovered NLO material, LBO[25], has also been identified as an excellent candidate for SHG of 1.3μm radiation[26-28]. The interesting phase-matching retracing behaviour exhibited for SHG in LBO facilitates noncritical phase matched (NCPM) SHG over a broad region near 1.3μm under temperature tuning[28,29]. Although there have been a few reports of frequency doubled, 1.3μm laser systems using this material[26,27,30,31], they have all employed a type I phase matching geometry. To achieve NCPM SHG of 1.3μm radiation using this geometry necessitates elaborate schemes to prevent moisture condensation on the crystal surfaces as a result of the low temperatures required[26,27,30]. However, LBO also offers a type II NCPM geometry for SHG not yet utilised for 1.321μm radiation, with operating temperatures around 40-50°C[28,29]. This property together with its high temperature- and angular acceptance bandwidth makes this configuration ideal for our purposes. The NCPM capability of LBO compared with the large walkoff angles in KTP is highly advantageous in this case, given the divergence characteristics of our 1.321μm Nd:YLF laser.

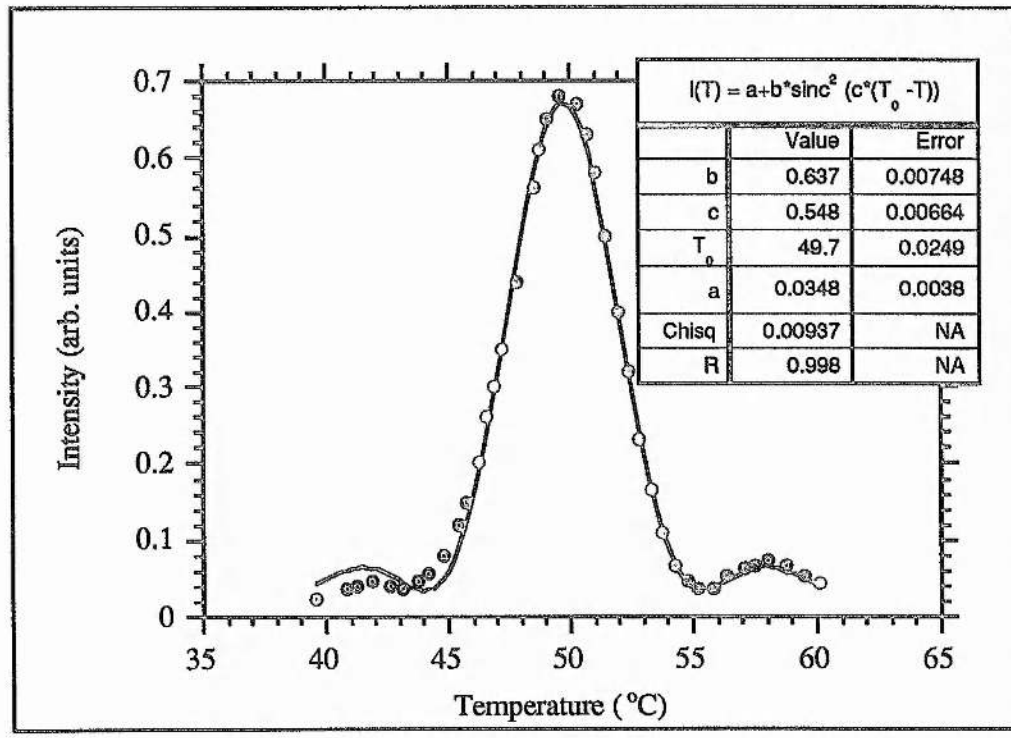

Figure 4.14 The experimentally determined phase matching curve with respect to temperature in LBO for type II NCPM frequency doubling of 1.321μm, as well as a fitted $sinc^2$ function.

The KTP crystal was 10mm long and cut normal to $\theta = 60°$, $\phi = 0°$ for type II critical phase matched (CPM) doubling of 1.3μm radiation. The high walkoff in the critical plane (⊥ Y-axis) together with the poor divergence in the horizontal plane of the 1.321μm laser beam, meant that optimum doubling performance was achieved with cylindrical focusing of the horizontal plane of the pump beam in the noncritical direction. This resulted in a maximum conversion efficiency of 20% into the red at 660nm. If the cylindrical focusing was effected on the vertical plane of the pump beam also in the noncritical plane, then a maximum conversion efficiency of 16% was achieved into the red.

A 16mm long LBO crystal, cut for type II NCPM ($\theta = 0°$, $\phi = 0°$,) was used. Optimum focusing yielded a beam waist of 40-55μm in the LBO crystal, close to predictions of a computer model [32] based on the theoretical work of Eimerl[33], the Sellmeier equations of Mao et al. [34] and the temperature dependence model of Velsko et al.[35] and Tang and co-workers[36]. Second harmonic conversion efficiencies of up to 40% were observed, delivering up to 0.85mJ of 660nm light in pulses of 60ns. This compares to a predicted SH conversion efficiency of around 56%. In the model, the spatial beam profiles were represented by top-hat distributions and hence resulted in a higher than observed doubling efficiency. Also the temporal tail of the Q-switch pulse is not efficiently doubled (see Figure 4.11), further lowering the observed conversion efficiency. The temperature was varied whilst the SH energy was observed in order that the optimum temperature for doubling the 1.321μm radiation could be ascertained. The results are depicted in Figure 4.14 from which the temperature acceptance bandwidth was found to be 8.3°Ccm. This compares favourably with the 8.8°Ccm predicted by the computer model, and it lies between the measured and predicted values of 6.7°Ccm and 9.9°Ccm respectively of Lin and co-workers[29].

The phase matching temperature for SHG of 1.321μm radiation was found to be about 50°C. It should be noted, however, that the crystal was very slightly tilted to avoid feedback into the Nd:YLF cavity. The output produced by the SHG process was of much improved spatial quality compared to the fundamental beam, with a near diffraction limited beam being obtained.

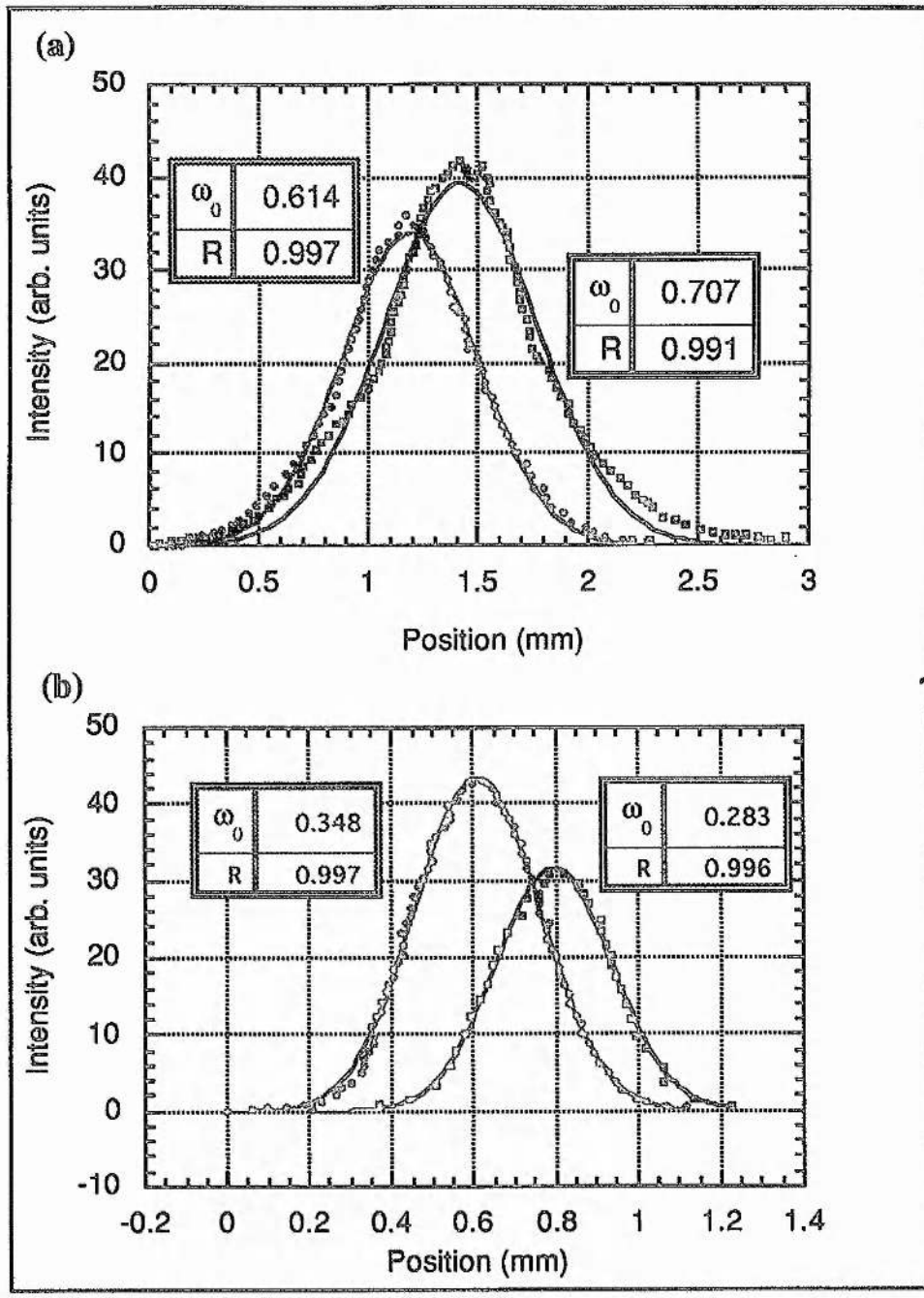

Figure 4.15 Contains the (a) near field and (b) far field spatial modes of the frequency-doubled (in LBO), 1.321μm output. The horizontal beam cross-section is represented by the open squares, while the vertical beam cross-section is represented otherwise. The far field results were obtained in the focal plane of a f=100mm lens.

The beam profiling measurements of the frequency-doubled output are reproduced in Figure 4.15. The far field results were obtained in the focal plane of an f=100mm lens. Using equation (2.2.13), the beam quality factor was calculated to be $M^2 \approx 1.1$ in both the vertical

and horizontal directions. The horizontal near field beam waist used is the measured waist of about 0.77mm and not the fitted value in Figure 4.15. The improved quality of the frequency doubled beam is attributed to the nonlinear nature of the gain in the SHG process.

This represented a 0.85mJ source of 76ns duration pulsed 660nm light in a near-diffraction-limited beam, albeit slightly elliptical. This was used to pump the vibronic material Cr:LiSAF, the development of which will be discussed in the next chapter.

4.4 The 1.047μm Nd:YLF laser

As mentioned in the introduction to this chapter, the 1.047μm Nd:YLF laser will not be discussed in detail here since its development has been previously effected by other workers within this department. The cavity layout is very similar to the final layout of the 1.3μm system and is depicted in the figure below.

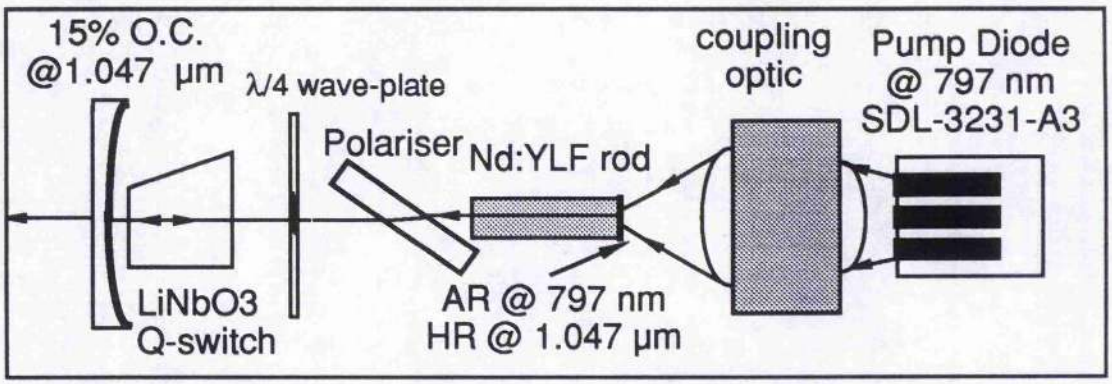

Figure 4.16 A schematic of the final configuration of the 1μm Nd:YLF laser. The higher gain than 1.3μm allowed a quarter-wave plate to be inserted instead of applying an equivalent dc voltage to achieve holdoff.

There are two major differences compared to the 1.3μm system. First, a high-quality polariser was used instead of an uncoated glass etalon at Brewster's angle. The much higher gain of the 1μm transitions meant that a polariser with a large extinction ratio was required in order to achieve holdoff of laser action in the high-Q state of the resonator. The second major difference was in how the low-Q state was achieved. In the 1μm system an intracavity quarter-wave plate was used, instead of a dc bias voltage, to provide the necessary rotation of the polarisation such that it was rejected by the polariser on the second pass. Again the higher

gain of the 1μm made this method feasible as the extra parasitic loss associated with the quarter-wave plate was easily overcome.

The same coupling optic arrangement saw an elliptical pump mode spot, of approximately 2.3x1.6mm in diameter, coupled into a 3x3x6mm Nd:YLF crystal. All intracavity components were anti-reflection coated at 1.047μm and the Q-switch crystal was again lithium niobate. With about 66mJ of pump energy, the system delivered, in Q-switched operation, up to 4.4mJ (with 5% fluctuations) in pulses of about 30ns (with 5% fluctuations), with a 20% output coupler. This output was frequency-doubled in KTP using a type II critically phase matched geometry. Finally output at 523nm was obtained in the form of 25ns pulses with up to 2.2mJ of energy per pulse. This was delivered in a symmetrical TEM_{00} beam of near diffraction limited divergence ($M^2 \approx 1.3$).

This source was used to pump a gain-switched Ti:sapphire laser which will be discussed in the chapter following that discussing the Cr:LiSAF laser which is presented next.

References

[1] C.F. Rae, J.A.C. Terry, B.D. Sinclair, M.H. Dunn and W.S. Sibbett, "Single-frequency, end-pumped Nd:YLF laser excited by a 12mJ diode-laser array" *Opt. Lett.*, 17, (1992), p1673

[2] C.P. Rahlff, B.D. Sinclair and W. Sibbett, M.H. Dunn, "High-power, end-pumped effects and applications in Nd:YLF at 1047 and 1321nm", Conference on Lasers and Electo-optics (CLEO 94), Anaheim USA, May 1994, Technical Digest Series 8 , p308

[3] G.R. Morrison, M. Ebrahimzadeh, C.F. Rae and M.H. Dunn, "Diode-pumped, Q-switched, 1.321μm Nd:YLF laser and its frequency doubling", *Opt. Comm.*, 118, (1995), p55

[4] G.R. Morrison, M. Ebrahimzadeh, C.F. Rae and M.H. Dunn, "All-solid-state gain-switched Cr:LiSAF laser", Conference on Lasers and Electo-optics (CLEO '95), Baltimore USA, May 1995, Technical Digest Series 15 , p15

[5] H.H. Zenzie, M. Thomas, C. Carey, E.P. Chicklis and M. Knights, "Non-linear Conversion of 1.3μm Nd:YLF Emission", in *Tunable Solid State Lasers II*, Vol. 52, Eds. Budgor, Esterowitz and De Shazer, Springer-Verlag (1986), p364

[6] N.P. Barnes, D.J. Getlemy, L. Esterowitz and R.E. Allen, "Comparison of Nd 1.06 and 1.33μm Operation in Various Hosts", *IEEE J. of Quant. Elec.*, QE-23, (1987), p1434

[7] T.M. Pollak, W.F. Wing, R.J. Grasso, E.P. Chicklis and H.P. Jenssen, "CW Laser Operation of Nd:YLF", *IEEE J. of Quant. Elec.*, QE-18, (1982), p159

[8] W. Grossman, M. Gifford and R.W. Wallace, "Short-pulse Q-switched 1.3- and 1-μm diode-pumped lasers", *Opt. Lett.*, 15, (1990), p622

[9] J.E. Murray, "Pulsed Gain and Thermal Lensing of Nd:$LiYF_4$", *IEEE J. of Quant. Elec.*, QE-19, (1983), p488

[10] H.R. Verdún and Ti Chuang, "Efficient TEM_{00}-mode operation of a Nd:YAG laser end pumped by a three-bar high-power diode-laser array", *Opt. Lett*, 17, (1992), p1000

[11] E. Hecht in OPTICS, Chap. 8, p299, 2nd Ed, Addison-Wesley Publishing Co., (1987)

[12] A.E. Siegman in *LASERS*, Ch.12, University Science Books (1986), p482

[13] D. Findlay and R.A. Clay, "The measurement of internal losses in 4-level lasers", *Phys. Lett.*, 20, (1966), p277

[14] G. Cerullo, S. De Silvestri and V. Magni, "High efficiency, 40W cw Nd:YLF laser with large TEM_{00} mode", *Opt. Commun.*, 93, (1992), p77

[15] B. Frei and J.E. Balmer, "1053-nm-wavelength selection in a diode-laser-pumped Nd:YLF laser", *Appl. Optics*, 33, (1994), p6942

[16] W. Koechner in *Solid-state Laser Engineering* 3rd Ed., Springer-Verlag (1992), Ch. 8

[17] A.L. Harmer, A. Linz and D.R. Gabbe, "Fluorescence of Nd3+ in Lithium Yttrium Fluoride", *J. Phys. Chem. Solids*, 30, (1969), p1483

[18] R.F. Belt, G. Gashurov and Y.S. Liu, "KTP as a harmonic generator for Nd:YAG lasers", *Laser Focus*, Oct., (1985), p110

[19] A.A. Ballman, H. Brown, D.H. Ohlson and C.E. Rice, "Growth of KTP from molten tungsten melts", *J. Crystal Growth*, 75, (1986), p390

[20] T. Nishikawa and N. Uesugi, "Angle tuning characteristics of second-harmonic generation in $KTiOPO_4$ ", *Appl. Phys. Lett.*, **55**, (1989), p1213

[21] H. Vanherzeele, J.D. Bielein and F.C. Zumsteg, "Index of refraction measurements and parametric generation in hydrothermally grown $KTiOPO_4$ ", *Appl. Opt.*, **27**, (1988), p3314

[22] J-J. Zondy, M. Abed and A. Clairon, "Type-II frequency doubling at λ=1.30μm and λ=2.53μm in flux-grown potassium titanyl phosphate", *JOSA*, **B11**, (1994), p2004

[23] J.Q. Yao and T.S. Fahlen, "Calculations of optimum phase match parameters for the biaxial crystal $KTiOPO_4$", *J. Appl. Phys.*, **55**, (1984), p65

[24] M.V. Ortiz, J.H. Fair and D.J. Kuizenga, "High-Average-Power Second Harmonic Generation with $KTiOPO_4$ ", *OSA proc. on adv. solid-state lasers*, **13**, (1992), p361

[25] C. Chen, Y. Wu, A. Jiang, B. Wu, G. You, R. Li and S. Lin, "New nonlinear-optical crystal: LiB_3O_5", *JOSA*, **B6**, (1989), p616

[26] T. Ukachi, R.J. Lane, W.R. Bosenberg and C.L. Tang, "Measurements of noncritically phase-matched second-harmonic generation in a LiB_3O_5 crystal", *Appl. Phys. Lett.*, **57**, (1990), p980

[27] J.T. Lin, J.R. DeSalvo and J.L. Montgomery, "Generation of visible lasers (532, 548, 566, 589, 660nm) using noncritically phase matched LiB_3O_5 ", *CLEO '90*, **CWF40**, p280

[28] S. Lin, B. Wu, F. Xie and C. Chen, "Phase-matching retracing behaviour: New features in LiB_3O_5", *Appl. Phys. Lett.*, **59**, (1991), p1541

[29] S. Lin, B. Wu, F. Xie and C. Chen, "Phase matching retracing behaviour for second harmonic generation in LiB_3O_5 crystal", *J. Appl. Phys.*, **73**, (1993), p1029

[30] G. Hall and A.I. Ferguson, "Generation of single-frequency radiation at 1062, 1319, and 659.5nm with an all-solid-state, out-of-plane Nd:YAG ring laser", *Opt. Lett.*, **19**, (1994), p557

[31] J.R. Lincoln and A.I. Ferguson, "All-solid-state intracavity-doubled Nd:YLF laser producing 300mW of 659-nm light", *Opt. Lett.*, **19**, (1994), p1213

[32] Y. Tang, University of St. Andrews, private communication

[33] D. Eimerl, "High Average Power Harmonic Generation", *IEEE J. of Quant. Elec*, QE-23, (1987), p575

[34] H. Mao, B. Wu, C. Chen, D. Zhang and P. Wang, "Broadband optical parametric amplification in LiB_3O_5", *Appl. Phys. Lett.*, 62, (1993), p1866

[35] S.P. Velsko, M. Webb, L. Davis and C. Huang, "Phase-matched harmonic generation in lithium triborate (LBO)", *IEEE J. of Quant. Elec.*, QE-27, (1991), p2182

[36] Y. Tang, Y. Cui and M.H. Dunn, "Thermal dependence of the principal refractive indices of lithium triborate", *JOSA*, B12, (1995), p638

CHAPTER 5

THE Cr:LiSrAlF$_6$ LASER

5.1 Introduction

The initial aim of this investigation was to achieve tuneable operation of a Cr:LiSAF laser with output in the form of nanosecond duration pulses. Ultimately single-frequency operation of this laser was sought.

The frequency doubled, Q-switched, 1.321μm Nd:YLF pump laser described in the preceding chapter resulted in gain-switched operation of the Cr:LiSAF laser, thus ensuring pulsed output with high peak power. The advantage of this design was threefold as described in Chapter 3. To reiterate, the benefits are gained firstly from the efficiency of the frequency doubling of Q-switched, as opposed to long-pulse, output from the 1.3μm Nd:YLF laser and secondly from the fact that none of the resulting pump light is lost through inefficient storage in the vibronic medium. The third advantage is that no intracavity Q-switching elements are required in the vibronic laser resonator. Such devices are intrinsically lossy even when only a single frequency output is sought. In the case of a vibronic laser when broadly tuneable output is desired it becomes more difficult to obtain components with low loss over an extended frequency range.

Once tuneable output from the Cr:LiSAF laser was obtained, the next goal was to achieve line-narrowed output by using intracavity etalons[1]. To achieve the goal of a single-frequency, tuneable laser, the idea was to eliminate the broadening effects of spatial hole burning by converting the cavity into the equivalent ring configuration (as discussed in section 2.2.2), and implement uni-directional operation by way of a Faraday rotator. In the following section, the first tuneable version of this laser, using an intracavity prism will be described. The tuning performance with a birefringent filter will then be described and finally the attempted line-narrowing of the standing-wave oscillator will be presented.

Cr:LiSAF was abandoned at this point without attempting to achieve single-frequency operation. The reason for this decision was that the parasitic losses of the standing-wave laser

were high, which Cr:LiSAF, with its relatively small emission cross-section (see table 3.1) was unable to efficiently overcome. Attention was therefore focused on Ti:sapphire which with its higher emission cross-section is a more promising alternative. The Ti:sapphire laser was initially built in exactly the same configuration as the Cr:LiSAF laser described in this chapter. This was done to facilitate comparison with the Cr:LiSAF laser thus enabling an interesting evaluation of Cr:LiSAF in this configuration. This comparison appears in section (6.2). The further development of the Ti:sapphire laser could then be used to discuss the limitations of Cr:LiSAF in a diode-pumped, Q-switched configuration. These considerations are deferred until the next chapter after the Cr:LiSAF laser has been properly discussed here.

5.2 Initial cavity design and development

5.2.1 Cavity design considerations

Two factors need to be considered in the design of the initial system. Firstly, the minimum pump spot size for the given pump power must be ascertained such that efficient absorption is attained whilst simultaneously ensuring that no crystal damage is incurred. Secondly, a resonator must be designed which exhibits the requisite mode matching and is also able to accept the bulky intracavity elements necessary for single frequency operation.

A 1.5% at. wt. doped, Brewster/Brewster Cr:LiSAF crystal, 15mm long from tip to tip, was acquired[2] for this laser. Low doping was deemed necessary in the light of the thermal problems associated with Cr:LiSAF; as discussed in chapter 3. The length of the crystal was chosen for 90% absorption in the absence of saturation. As discussed in section (2.1.4) the absorption of pump light can become saturated in the same way that the gain of a laser medium can become saturated above threshold. The average saturation fluence of the pump absorption is given by

$$E_{sat}^{p-flu} = h\nu_p / \sigma_a \qquad 5.1$$

For 660nm pumping of Cr:LiSAF this is found to be roughly 6.7J.cm^{-2}. However bulk damage has been found to occur at peak fluences in the region of 15J.cm^{-2} for 50-ns pulses[3]. Using this latter value as an upper limit for the desired peak pump fluence, enabled the minimum pump beam waist radius to be calculated for the given maximum pump energy of

the pump laser. With a maximum pump energy of about 0.85mJ in 76ns pulses, the minimum pump waist radius that can be used without fear of crystal damage is approximately 100μm. Based on this calculation, a cavity was designed having a mode size in the crystal of 100μm for a pump mode of similar proportions. However, it was soon found that the pump fluence was too high and bulk damage was incurred in the Cr:LiSAF crystal. This corresponds to bulk damage for peak pump energy fluences of greater than 10J.cm^{-2}, which is somewhat less than that reported above[3]. The cavity was therefore redesigned with a mode waist radius of 130μm in the crystal. This resulted in a mode matching factor of $\eta_B \approx 0.86$, using equation (2.1.44) with a 150μm pump spot radius.

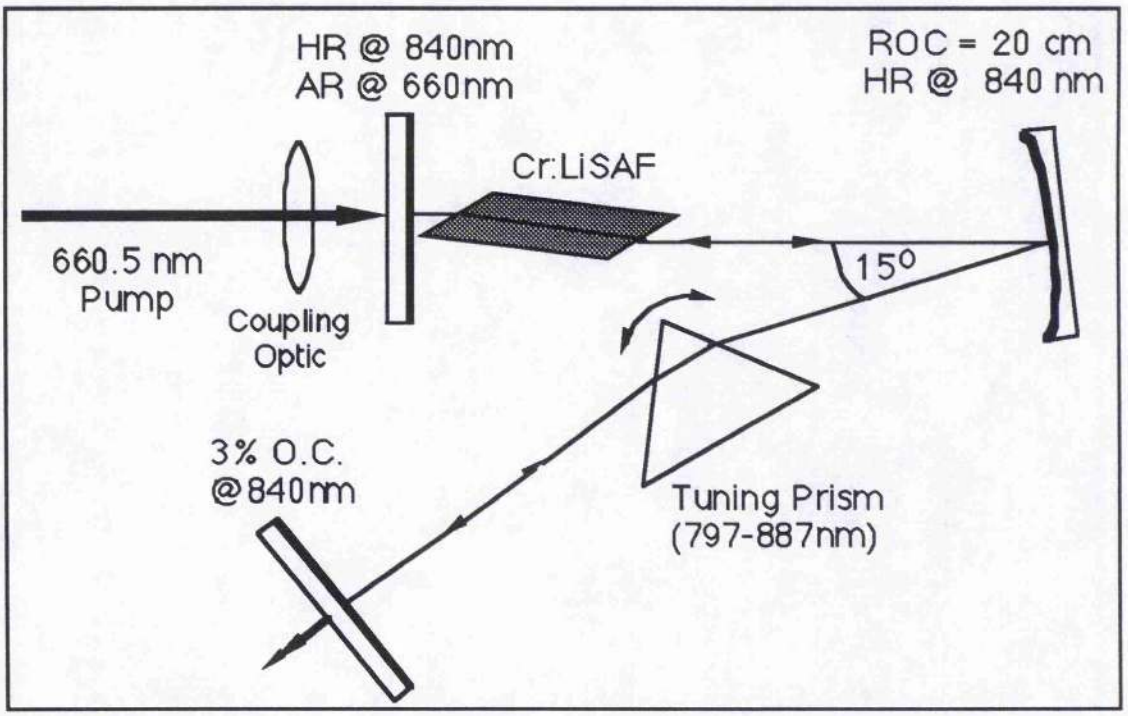

Figure 5.1 Illustrating schematically the layout of the first tuneable Cr:LiSAF laser resonator. The arm containing the crystal was 16cm long and the arm containing the tuning prism was 18cm. The fold mirror was of 20cm ROC and angled to 15° to provide astigmatic compensation for the Brewster cut crystal. The crystal was doped with 1.5% at. wt. of Chromium and was 15mm tip to tip. The HR mirrors were T<0.5% for 780-870nm and the output coupler was T=3% over the same range.

The actual cavity design considerations for this laser were considered in section (2.2.2) and specifically in Figure 2.6. It was shown that the simplest cavity which is equivalent to an X-cavity which can be easily converted into a ring configuration is a simple folded three mirror

standing-wave resonator. With reference to Figure 2.6 and equation (2.2.30), a resonator with dimensions L_1=16cm, L_2=18cm and a folding mirror of ROC=20cm has a maximum spot size radius in each arm of ω_{10max}≈130μm This was confirmed by beam profile measurements which are reproduced in Figure 5.6. The laser is schematically illustrated in Figure 5.1. The Cr:LiSAF crystal was mounted on a water-cooled brass heat sink, positioned as close to the input mirror as possible. The input mirror was AR coated at 660nm and HR at 780-870nm. The folding mirror was also HR coated at 780-870nm for normal incidence. This mirror is expected to be slightly more lossy due to the 15° tilt required for astigmatic compensation and also to allow the insertion of intracavity components in the long arm of the resonator. The output coupler was 3% transmitting in a similar range. A 2% output coupler was also available. Once operation of this laser was achieved, a glass prism was inserted to facilitate tuning.

5.2.2 Performance of the basic laser

The pump efficiency was measured in this system. Approximately 95% of the pump light was transmitted through the coupling optics and back mirror into the cavity and up to 90% of this was absorbed by the laser rod. These measurements enabled the gain factor to be estimated for this system. For gain-switched systems this gain factor is given by

$$K' = \eta \frac{\sigma_{21}}{h\nu_l A} \qquad (5.2)$$

as defined by equation (2.1.53). Recall that A is the area of the pumped mode in the crystal and $\eta \approx 0.6$ is the overall efficiency factor as defined by equations (2.1.52) and (2.1.53) and using the values discussed above. This was estimated for our Cr:LiSAF laser at the peak lasing wavelength of 840nm. The stimulated emission cross-section for Cr:LiSAF at the peak of its operational bandwidth is $\sigma_{21} \approx 5\times10^{-20} cm^{-2}$; see table 3.1. With these substitutions the efficiency factor and the peak gain parameter for this laser were estimated to be $\eta \approx 0.6$ and $K' \approx 0.23$, respectively. This are used in section (5.3.2) where the experimental results are compared with theory.

With no intracavity tuning elements the spectral output was found to peak at about 840nm and had a spectral bandwidth of about 32nm as measured by a 0.25m monochromator (Chromex 250IS/SM). A glass prism was inserted into the long arm of the cavity as depicted in Figure 5.1 and the tuning curve was obtained. This is reproduced below in Figure 5.2 and was obtained with an input pump energy of about 0.7mJ per pulse. The prism introduced additional parasitic loss which increased the threshold from around 250μJ to above 300μJ. Near the peak of the tuning range a maximum output energy of about 95μJ was obtained in pulses of 70-100ns duration. The line-narrowing effect of the prism was not appreciable; the lasing bandwidth being reduced to 10-15nm about the maximum. For this reason the prism was abandoned in favour of a three-plate birefringent tuner. Operation of the Cr:LiSAF laser with this birefringent tuner will be discussed in the following section.

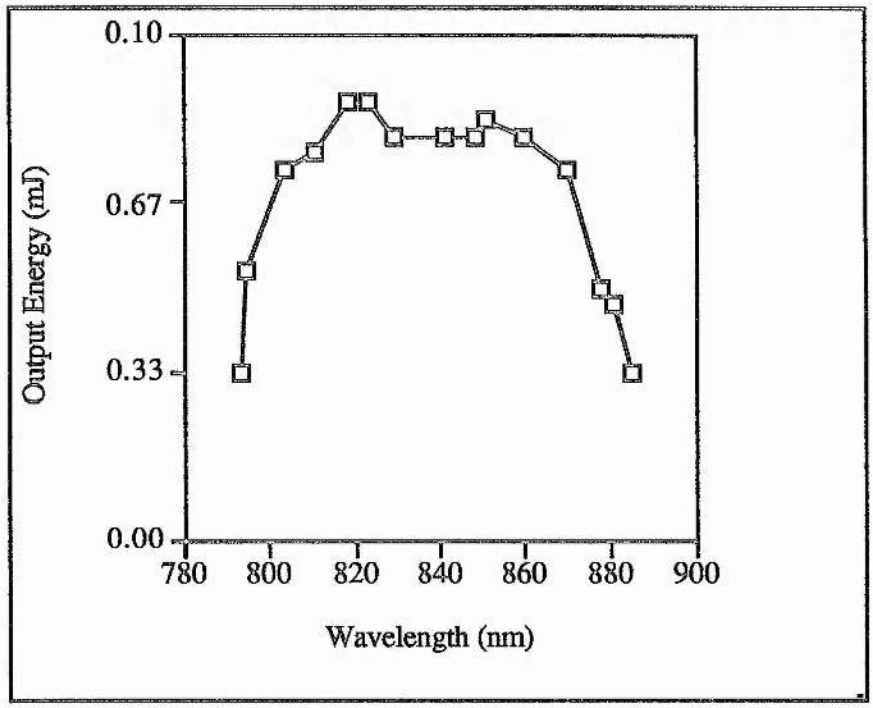

Figure 5.2 Contains the tuning range of the Cr:LiSAF laser tuned with glass prism. The tuning range was limited by the mirror coatings as specified in Figure 5.1.

5.3 Final cavity layout and performance

5.3.1 Tuneable Cr:LiSAF laser performance

The final cavity layout is depicted in Figure 5.3 and is identical to that depicted in Figure 5.1 with the exception that a three plate birefringent filter has replaced the glass prism. The birefringent filter used was obtained from a commercial cw Ti:sapphire laser[4]. Various uncoated glass etalons (20, 100 and 200GHz), were inserted into the cavity to effect further line-narrowing. The cavity dimensions were L_1=16cm for the arm containing the Cr:LiSAF crystal and L_2=18cm for the arm containing the line-narrowing and tuning elements. This resulted in a laser mode waist radius of $\omega_{0max}\approx$130μm at each of the flat mirrors, as depicted in Figure 5.6. The pump mode was unchanged at 150μm.

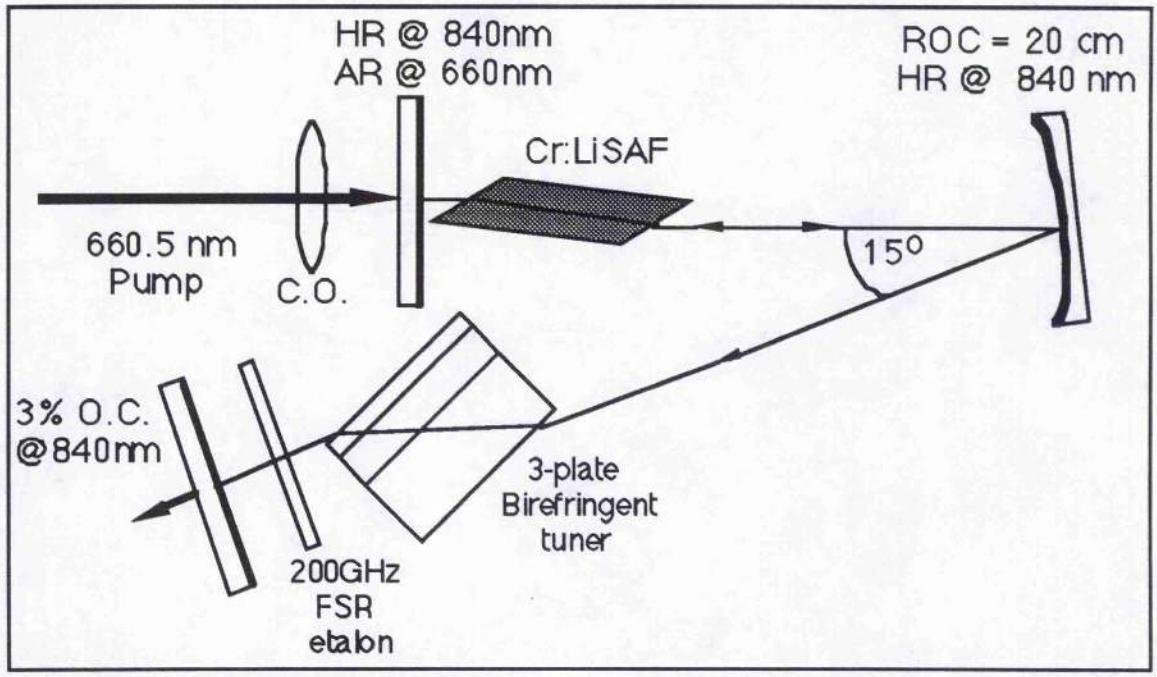

Figure 5.3 Illustrating schematically the layout of the final tuneable Cr:LiSAF laser resonator. All cavity dimensions and components are identical to those in Figure 5.1. The 3-plate birefringent filter was used for line-narrowing and to facilitate tuning. Uncoated glass etalons were used for further line-narrowing.

The Cr:LiSAF laser tuned with the birefringent filter was found to tune over the range 800-880nm. This is slightly restricted compared to the tuning range obtained with the prism as indicated in Figure 5.2. The difference is attributed to the higher insertion loss of the birefringent filter and the superior discrimination against nearby frequencies. The cavity

mirrors are also a factor which limited the observed tuning range which is somewhat reduced compared to the full Cr:LiSAF tuning range of 760-1010nm (see Table 3.1). With the birefringent filter the laser typically operated over a 170GHz bandwidth. This was measured with a 1m monochromator (Rank Hilger: Monospek 1000), and confirmed with Fabry-Perot interferometer. These measurements will be discussed in more detail in section (5.3.3).

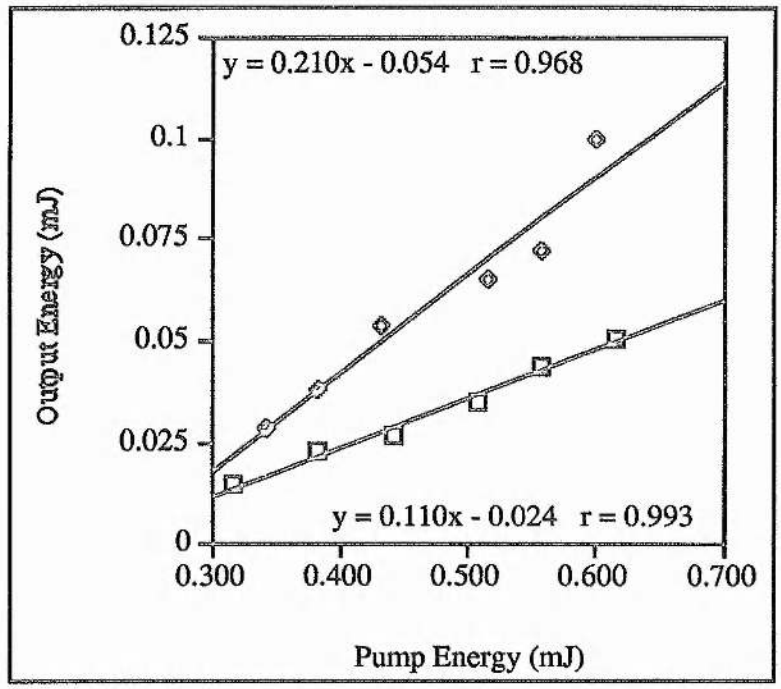

Figure 5.4 Contains the slope efficiency measurements for the Cr:LiSAF laser with birefringent tuner. The open squares are for a 2% output coupler while the open diamonds are for a 3% output coupler.

It should be noted that the laser output contained two distinct spectral components when the birefringent filter was tuned to the edges of the tuning range. In this case a second frequency component to the output was observed. This second frequency component was measured to be of reduced output near the peak of the tuning range. This occurs because of the unwanted transmission spikes which are characteristic of multiple-plate birefringent tuners[5]. Thus when the birefringent tuner is rotated such that the frequencies at the extremes of the tuning range experience no losses, there seems to be a secondary transmission peak which falls somewhere near the peak of the gain curve. Although this secondary transmission peak is much reduced, the gain at the centre of the gain curve is sufficient to overcome the extra losses, which gives rise to a second spectral component to the output.

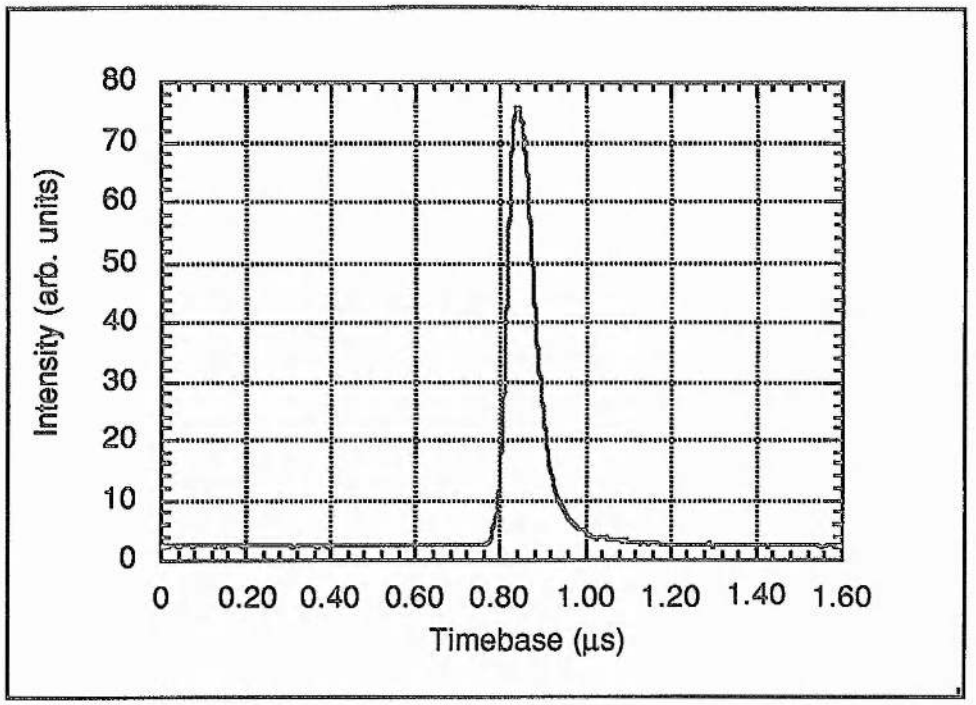

Figure 5.5 Is a reproduction of a typical gain-switched output pulse from the Cr:LiSAF laser. The pulse shown here is of 75ns duration, FWHM, and was obtained at the peak of the tuning curve, i.e. near 840nm.

Slope efficiency measurements of this system were obtained at the peak of the tuning curve. The birefringent filter was tuned so that the laser was operating near 840nm and the output energy per pulse was measured as a function of pump pulse energy. The results for the 2% and 3% output couplers are reproduced in Figure 5.4.

The observed thresholds were approximately 270μJ and 300μJ for the 2% and 3% output couplers respectively. A maximum output of about 100μJ was obtained with the 3% output coupler for a pump energy of 620μJ. The output energy exhibited fluctuations of 13.5% about the mean values. The slope measurements will be discussed in more detail in the following section which deals with a theoretical comparison of the results.

Typically there was a delay of 200-300ns between the end of the pump pulse and the start of the Cr:LiSAF pulse indicating gain-switched operation. At the peak of the tuning curve the output pulses were generally of 75ns duration as depicted in Figure 5.5. The pulse duration increased to nearer 150ns at the extremes of the tuning range. The pulse durations were found to be stable to within 7% of their mean values.

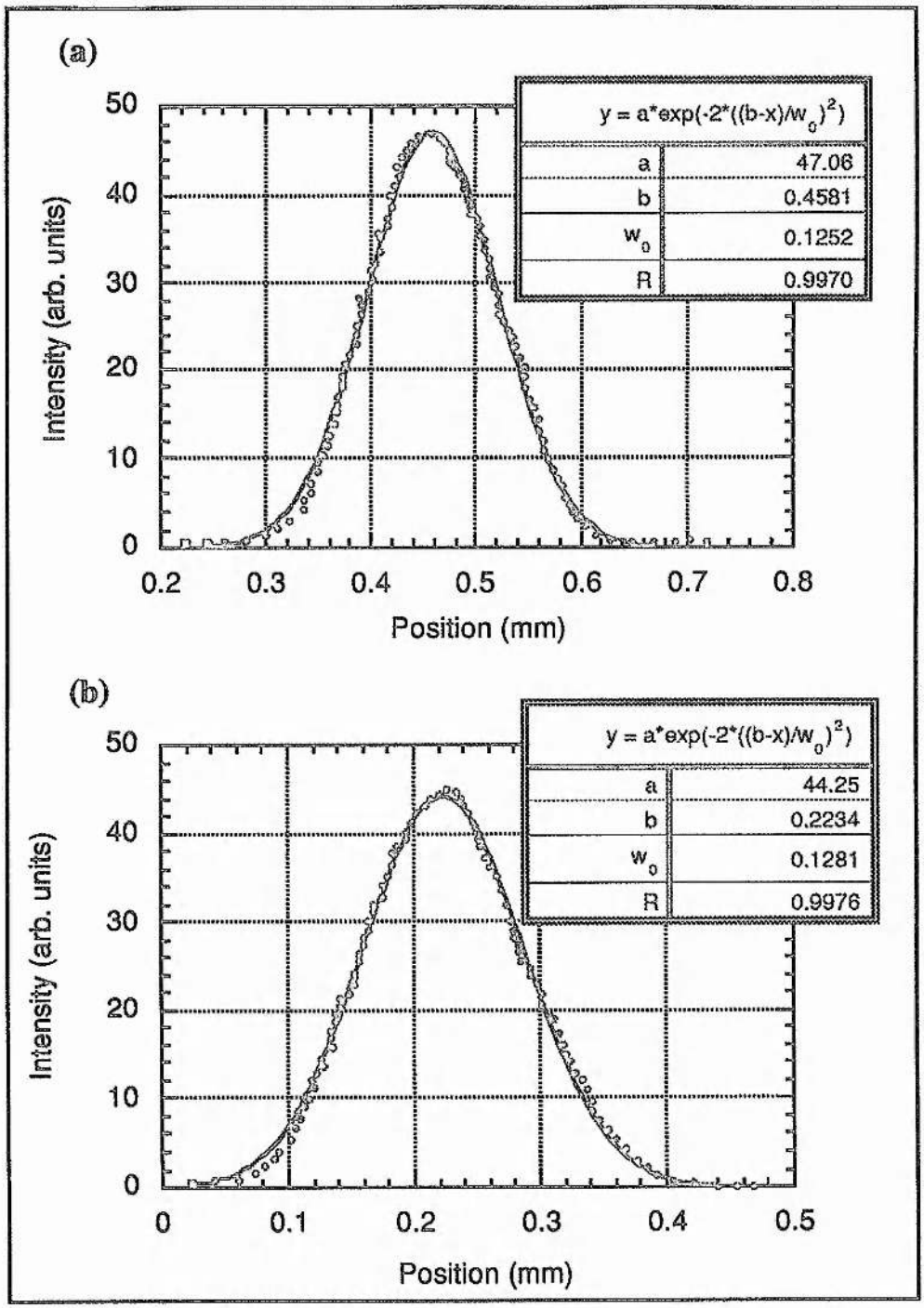

Figure 5.6 Contains the near field (a) horizontal and (b) vertical spatial beam cross-sections of the Cr:LiSAF laser in its final configuration. The output was found to be of symmetrical TEM_{00} nature with diffraction limited divergence properties.

The beam quality of the Cr:LiSAF laser was measured. The horizontal and vertical spatial cross-sections of the near field output of the laser with the 3% output coupler are presented in

Figure 5.6. The output is seen to be of TEM_{00} nature and shows no astigmatism. The divergence quality in both planes was found to be diffraction limited.

Since the internal waist radii in both arms are more or less the same in this configuration, the above measurement shows that the actual waist radius in the crystal is close to the calculated cold cavity waist of 130μm.

5.3.2 Comparison with theory

The pump efficiency and the other efficiency factors are unchanged from those of the first incarnation of this laser as described in section (5.2). Hence the gain factor $K' \approx 0.23$, as estimated in section (5.2.2), is valid for this laser operating at 840nm, the peak of its gain curve.

By measuring the beat frequency of adjacent cavity modes with a spectrum analyser, the round trip optical length of the cavity was found to be 67cm. This is close to the round trip length of 68cm according to the calculated cavity dimensions. The losses were not known and were left as a variable parameter in the Q-switch equations of section (2.3.1). comparing the experimental performance with the theoretical model using equation (2.3.10) for the output energy and equation (2.3.13) for the pulse duration, the round trip parasitic losses were determined to be about L=9%. This seems quite high even with the intracavity birefringent filter. The explanation for this is that it was discovered after the investigation was completed that the Cr:LiSAF was not correctly inserted at Brewster's angle. The crystal was inserted in such a way that the angle of incidence was equal to the internal Brewster angle instead of the external angle. For Cr:LiSAF, with a refractive index of about 1.4 (see Table 3.1), the internal Brewster angle is approximately 35.5°. Using this in Figure 3.6 yields a reflection coefficient of 1.3%. In fact the output off the Brewster surfaces was measured and corresponded to an output coupling of about 1.8% per surface. This is in reasonable agreement with the above hypothesis.

If the laser was remodelled as having an effective output coupling of 6.5% and about 5% parasitic loss instead of 3% output coupling and 9% parasitic loss, then total output energies

of 250μJ for 750μJ of pump energy are predicted. This is in agreement with the results taken when all the output including that off the two Brewster surfaces was combined.

With 750μJ of pump energy per pulse, the optimised output couplings can be calculated, using equation (2.3.20), for the actual laser with 9% loss and the remodelled laser with only 5% loss. The respective optimum output couplings are found to be 10% and 9%, respectively. These optimally coupled lasers are predicted to yield maximum output energies of 190μJ and 300μJ with corresponding slope efficiencies of 27% and 37%. As expected these more closely approach the limit of $\eta \approx 0.6$ set by the various efficiency factors described at the beginning of this chapter. While it cannot be assumed that the correct orientation of the laser crystal will result in the recovery of all the unnecessary loss, a substantial improvement in performance is to be expected. Other sources of parasitic loss which account for the 5.5% remaining loss are the birefringent filter and the curved folding mirror which was specified to be highly reflecting at normal incidence; the actual angle of incidence being between 5 and 10° for astigmatic compensation (see equation (2.2.33)).

The usual theoretical threshold as determined by equation (2.1.58) was found not to differ much from the experimental threshold. A better agreement was obtained if the upper state lifetime of Cr:LiSAF was taken into account, as discussed in section (2.3.4), since this is a gain-switched laser. If equation (2.3.26) was solved, the actual threshold of this gain-switched Cr:LiSAF laser was found to be 10% higher than the traditional value predicted by equation (2.1.58). Strictly speaking, this difference means that the simple linear relationship between energy threshold and losses as expressed in equation (2.1.60) is no longer valid. It is therefore no longer possible to determine the gain factor and the parasitic losses by means of a Findlay-Clay analysis[6] as discussed in section (2.1.5). Instead numerical methods are required[7].

5.3.3 Line-narrowed operation of the Cr:LiSAF laser

The use of a three-plate birefringent filter instead of a tuning prism substantially reduced the operational linewidth of the Cr:LiSAF laser across its tuning range. As was mentioned in the preceding sections, the linewidth about the selected frequency of operation was reduced from 15nm in the case of tuning by prism to approximately 170GHz in the case of the birefringent filter. In the resonator used, there are about 240 allowed cavity modes within this bandwidth.

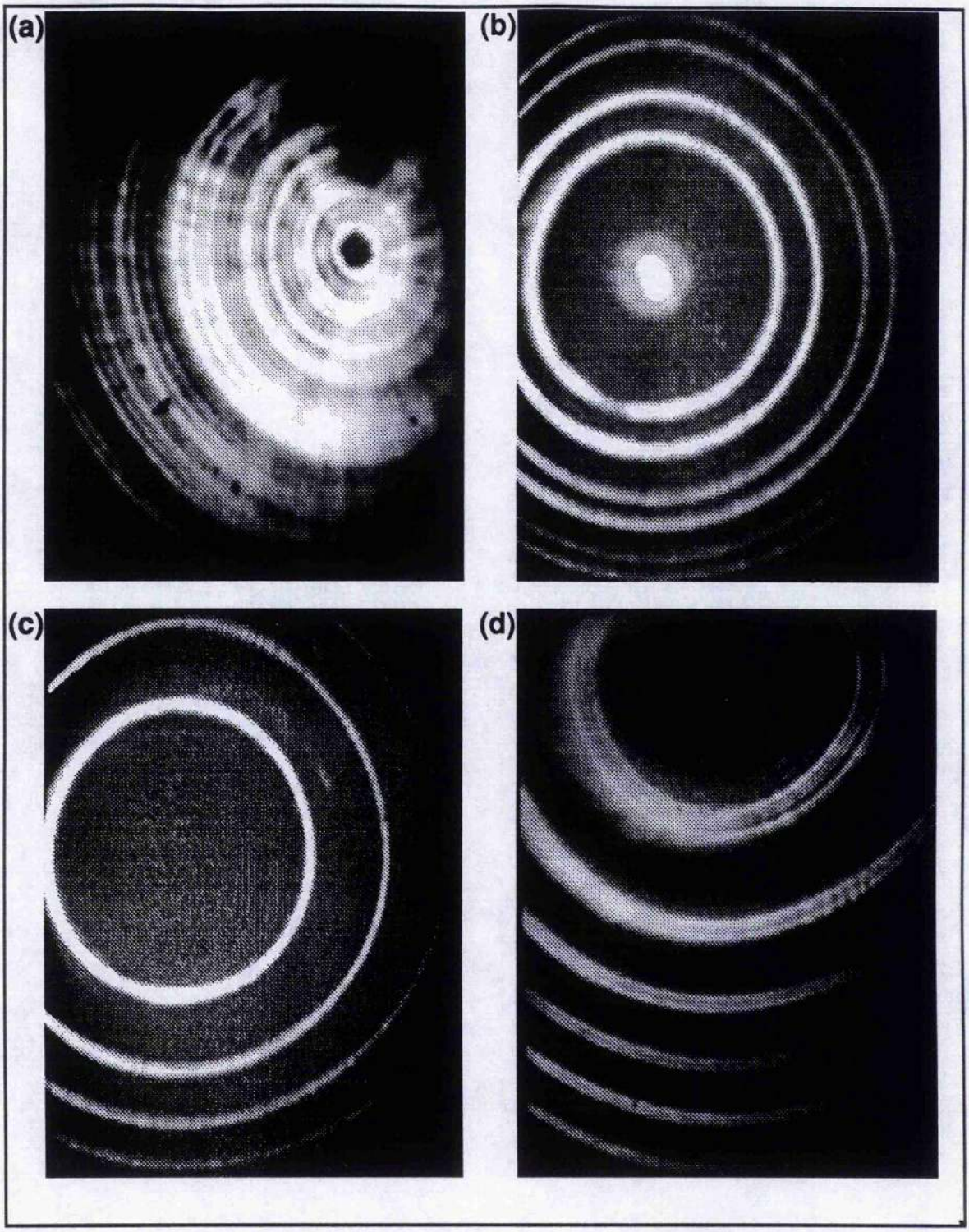

Figure 5.7 Contains CCD camera images of various Fabry-Perot fringe patterns of the output from the Cr:LiSAF laser. In (a) the laser linewidth was restricted with a birefringent filter only. A 200GHz uncoated glass etalon was inserted to further restrict the linewidth of operation. (b) Illustrates operation of the laser on two adjacent etalon modes while in (c) the laser was operating on only a single etalon mode. In (d) the FSR of the interferometer was reduced so that the linewidth could be more accurately determined.

Simultaneous lasing on all these modes does not occur due to reduced spatial hole burning effects resulting from locating the laser crystal at one end of the cavity, as described in section (2.2.2). The frequency bandwidth of the laser tuned by a glass prism was measured with a 1/4m monochromator (Chromex 250IS/SM). This was not accurate enough to measure the linewidth of the laser tuned by the birefringent filter which was instead measured with a 1m monochromator (Rank Hilger: Monospek 1000). With this monochromator the linewidth of the laser tuned with the birefringent filter was measured to be about 170GHz.

Further line-narrowing of this laser was implemented by inserting uncoated glass etalons into the resonator as depicted in Figure 5.3. A 0.5mm glass etalon with a free spectral range of 200GHz was inserted to select a single etalon mode from within the 170GHz passband of the birefringent filter.

The 1m monochromator was found to be inaccurate for the narrower linewidths obtained from this laser with the insertion of the intracavity etalons. Instead, measurement of the spectral output of this Cr:LiSAF laser under these line-narrowing conditions was made with a Fabry-Perot etalon. The etalon was built in-house with highly reflecting plane mirrors (R>99%) whose separation was variable.

A selection of ring patterns obtained with this etalon, captured with a CCD camera, is reproduced in Figure 5.7. In Figure 5.7 (a), the output of the laser containing only the birefringent filter is shown after having passed through the etalon with a free spectral range of approximately 50GHz. When the 0.5mm (200GHz) thick etalon was inserted either one or two spectral components were obtained. These are depicted in (c) and (b) respectively of Figure 5.7. The fact that two frequency modes were obtained with the 200GHz etalon in the laser cavity confirmed that the linewidth with only the birefringent filter was in the region of 200GHz. The exact spacing of the mirrors was calculated to be 3.2mm. The intracavity etalon was adjusted so that only a single frequency band was selected. The fringe pattern is reproduced in Figure 5.7 (c). In order that the linewidth of this output could be determined, the Fabry-Perot etalon spacing was increased to about 12.5mm which translates into a free spectral range of approximately 12GHz. Figure 5.7 (d) contains a fringe pattern obtained through such an etalon. This figure indicates a linewidth of about 4GHz. In this manner it was

found that the laser operated with a frequency spread of up to 10GHz. This corresponds to a maximum of about 20 cavity modes.

An attempt was made to further line-narrow this output by inserting a 5mm thick glass etalon which had a free spectral range of 20GHz. The laser was unable to overcome the extra losses introduced with the insertion of this etalon and so operation with a 10GHz linewidth described above represents the best performance of this laser.

5.4 Wing-pumped Cr:LiSAF

Out of interest it is worth mentioning that wing-pumped operation of the Cr:LiSAF laser has also been observed. The cavity layout is depicted in Figure 5.8. During the development of the 1.3μm laser, a highly-doped piece of Cr:LiSAF became available.

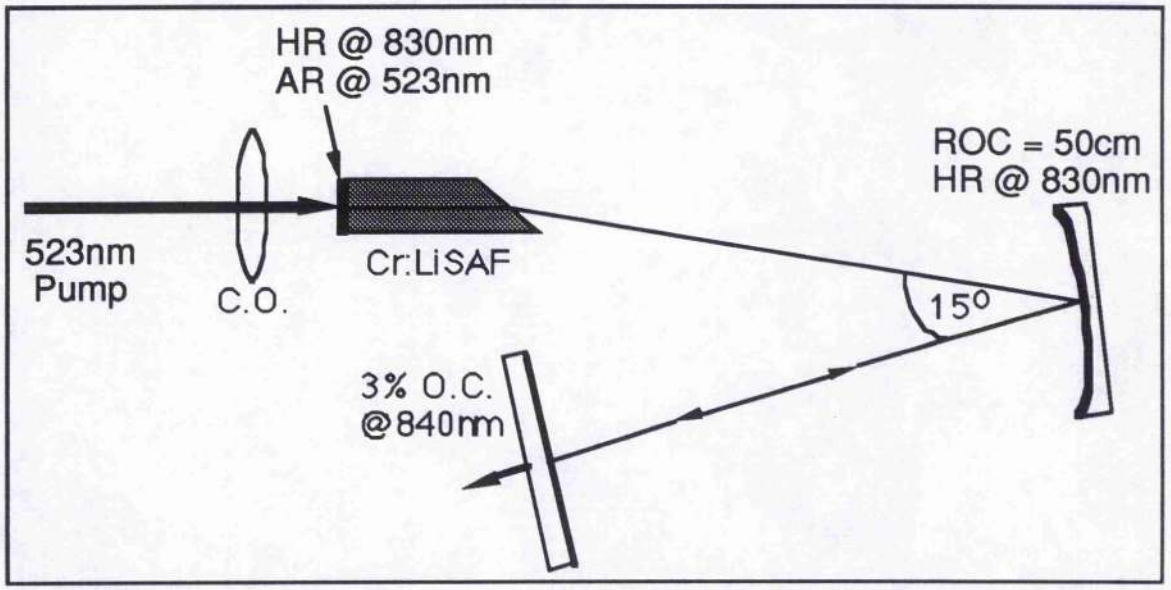

Figure 5.8 Schematic layout of the wing-pumped Cr:LiSAF laser resonator. The Cr:LiSAF crystal is nominally doped with 7% at. wt. chromium. Its rear surface has an AR @ 523nm and a HR @ 830nm coating while its other surface is Brewster angled. The crystal is 9mm long to the tip of the Brewster surface. The cavity arm containing the crystal is about 19cm long and the other arm is about 10cm long, giving a laser mode of approximately 200μm in the crystal for a 50cm ROC folding mirror.

This piece of Cr:LiSAF was doped with 7% at. wt. of Chromium. As mentioned in Chapter 3, the fact that Cr:LiSAF and Cr:LiCAF can be highly doped without adversely affecting their spectroscopic and thermo-mechanical properties means that they can be efficiently pumped in the tails of their absorption bands. This is referred to as wing-pumping[8]. A 523nm pump

source in the form of a frequency-doubled 1μm Nd:YLF laser was used to wing-pump the highly-doped Cr:LiSAF.

As depicted in Figure 5.8 the crystal had a flat rear surface which was AR coated at 523nm and broadband HR coated about 830nm. The other crystal surface was cut at Brewster's angle. This crystal formed part of a cavity which had a 200μm waist radius at the rear surface of the crystal. The 523nm pump beam was mode matched into the crystal.

A 523nm, wing-pumped Cr:LiSAF laser was successfully demonstrated. About 65% of the pump light was absorbed by the 9mm long (to the tip) crystal. Because of the threat of damage to the rear surface coatings, operation was restricted to slightly above threshold. The threshold was found to be in the region of 1mJ of green pump light. The pulse duration was measured to be about 600ns near threshold and about 380ns with 1.2mJ of pump light. Using a monochromator (Chromex 1/4m), the laser was found to operate over a linewidth of 17nm about 840nm at the higher pumping level.

5.5 Conclusions

At this point the Cr:LiSAF option was abandoned in favour of a Ti:sapphire equivalent. As mentioned in chapter 3, the far superior emission cross-section of Ti:sapphire implies that it should be able to cope more easily with the lossy intracavity components required for effective interferometric line-narrowing. This was expected to become even more critical if the resonator was to be converted into a ring with the intention of implementing uni-directional operation.

An additional consideration was the temperamental behaviour of the 1.3μm pump laser. These problems were described in chapter 4. The result was degraded pump performance which made it difficult to further investigate the Cr:LiSAF system. The Cr:LiSAF crystal itself contained much bulk damage which also made it difficult to achieve continued efficient operation.

On the positive side, a narrowband, tuneable, gain-switched Cr:LiSAF laser has been demonstrated. There does, however, appear to be room for improvement. Specifically, the output coupling has yet to be optimised. Secondly, the parasitic losses were found to be

unexpectedly large. As mentioned above, this is largely due to the crystal being incorrectly inserted at Brewster's angle. The theoretical model seems to indicate that output coupling in the 10% region would be optimum for this system with reduced losses of about 5% and a reliable 0.75mJ pump source. Projected output from such a system is 300μJ of energy in 65ns pulses. In this case the laser will more closely approach the upper limit of its operational efficiency which is set by the Stokes efficiency factor (82.5% at 800nm for 660nm pump).

In the next chapter the equivalent Ti:sapphire laser is constructed which facilitates a comparison with this Cr:LiSAF laser. The Ti:sapphire laser is developed further; to the point that the equivalent ring resonator was built. Single-frequency operation was achieved by the method of injection seeding as described in section (2.4). This would seem to be the way forward with a Cr:LiSAF system. With this method the intracavity losses would be minimised as no intracavity elements are required. This option will be discussed further in the concluding chapter.

References

[1] G.R. Morrison, M. Ebrahimzadeh, C.F. Rae and M.H. Dunn, "All-solid-state gain-switched Cr:LiSAF laser", Conference on Lasers and Electo-optics (CLEO '95), Baltimore USA, May 1995, Technical Digest Series 15 , p15

[2] Lightning Optical Corp., Tarpon Springs, Florida, USA

[3] D.J. Harter, J. Squier and G. Mourou, "Alexandrite-laser-pumped Cr^{3+}:$LiSrAlF_6$, *Opt. Lett.*, 17, (1992), p1512

[4] Schwarz Electro OpticInc., Research Division, 45 Winthrop Street, Concord MA 01742, U.S.A, "TITAN cw Ti:sapphire laser".

[5] W. Koechner in *Solid-State Laser Engineering 3rd Ed.*, Springer-Verlag, (1992), Ch. 5, p274

[6] D. Findlay and R.A. Clay, "The measurement of internal losses in 4-level lasers", *Phys. Lett.*, 20, (1966), p277

[7] J.M. Egglestone, L.G. DeShazer and K.W. Kangas, "Characteristics and kinetics of laser-pumped Ti:sapphire oscillators", *IEEE . of Quant. Elec.*, QE-24, (1988), p1009

[8] S.A. Payne, W.F. Krupke, L.K. Smith, W.L. Kway, L.D. DeLoach, and J.B. Tassano, "752nm Wing-Pumped Cr:LiSAF Laser", *IEEE J. of Quant. Elect.*, QE-28, (1992), p1188

CHAPTER 6

THE Ti:SAPPHIRE LASER

6.1 Introduction

The advent of the vibronic gain medium Ti:sapphire[1] has made a tuneable, all-solid-state replacement for cumbersome dye laser systems a possibility. The advantageous properties of solid-state media over dyes makes Ti:sapphire an attractive alternative. As discussed in chapter 3, the large stimulated emission cross-section (3.5×10^{-19} cm^{-2}) of Ti:sapphire is hampered by its energy storage capacity which is limited by its short fluorescence lifetime (3.2μs). This renders flashlamp pumping and Q-switching of Ti:sapphire both difficult and highly inefficient. Ti:sapphire is, therefore, predominantly a laser-pumped material operating either in cw mode or gain-switched mode. Recent development has led to vibronic materials such as Cr:LiCAF and Cr:LiSAF[2,3] which offer a better balance between stimulated emission cross-section and upperstate lifetime. Although this makes them more amenable to efficient Q-switching, they have severe limitations with regard to high average power operation as discussed in chapter 3. There it was also shown that under gain-switched operation Ti:sapphire is no longer limited by its short upperstate lifetime and thus its large emission cross-section gives it a significant advantage. The low emission cross-section of Cr:LiCAF[3] and the thermal problems associated with Cr:LiSAF when pumped with red laser diodes[4] mean that gain-switched Ti:sapphire is the best option for a high peak power, tuneable source in the near infrared.

For these reasons it was decided that an investigation into gain-switched Cr:LiSAF, as presented in the preceding chapter, would best be followed by a comparative investigation into Ti:sapphire. It was envisaged that the development of the Ti:sapphire laser would progress to a more mature state befitting of its perceived superior characteristics for gain-switched operation. The next section will deal with the comparative performance of the Cr:LiSAF laser discussed in the previous chapter and the equivalent Ti:sapphire. This will be successively followed by sections dealing with the conversion to an equivalent X-cavity

resonator, a ring laser with interferometric spectral control, an injection seeded ring laser and finally a high repetition rate injection seeded ring laser.

6.2 Ti:sapphire - Cr:LiSAF comparison

6.2.1 Cavity design considerations

The system was pumped by an electro-optically Q-switched Nd:YLF laser operating at 1.047μm which was frequency doubled in KTP (Type II CPM), as described briefly in chapter 4. It could deliver up to 2.2mJ in pulses of around 20ns duration in a high quality TEM_{00} beam..

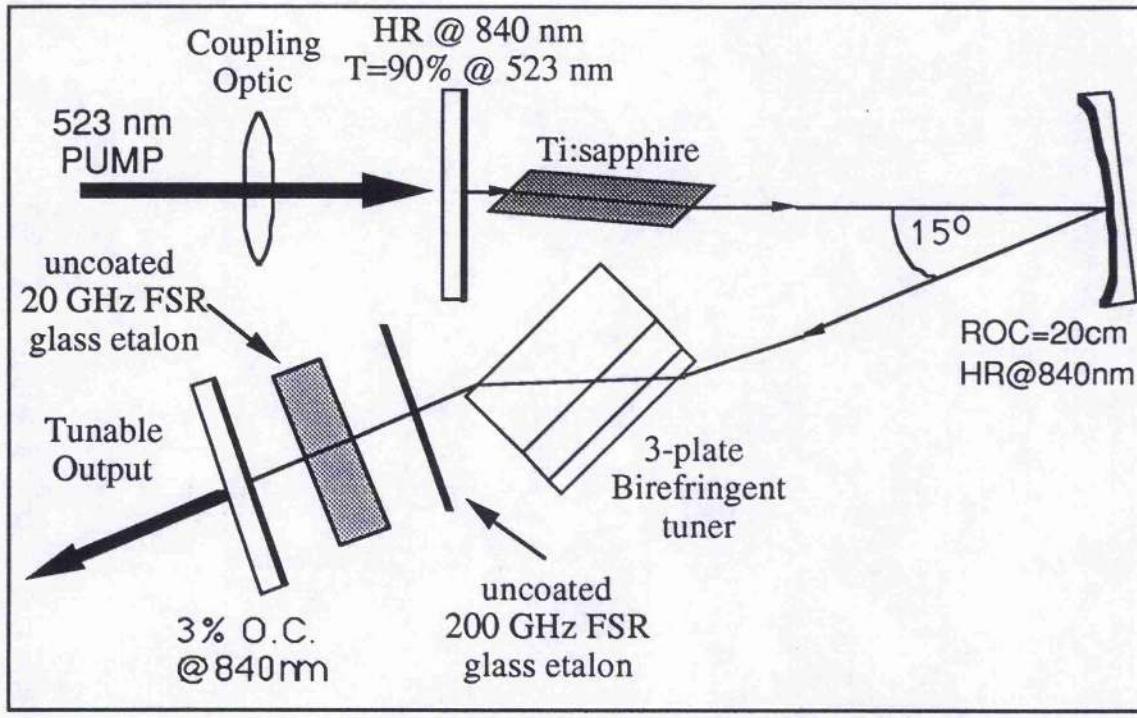

Figure 6.1 Illustrating schematically the layout of the equivalent Ti:sapphire laser resonator used in the comparison with Cr:LiSAF (see Figure 5.3). The arm containing the crystal was 16cm long and the arm containing the frequency selective elements was 18cm long. The fold mirror was of 20cm ROC and angled to 15° to provide astigmatic compensation for the Brewster cut crystal. The crystal was doped with 1.5% at. wt. of Titanium and was 5mm long. The mirrors were the same as those used in the Cr:LiSAF laser.

In order to achieve a valid comparison of the relative performance of these two materials under gain-switched operation, identical cavities were used. The cavity used is illustrated in

Figure 6.1. The only difference compared to the Cr:LiSAF cavity depicted in Figure 5.3 is that the input mirror is AR coated for 660nm and was found to be only 90% transmitting at 523nm, thus affecting the overall efficiency. The design considerations which led to the implementation of this resonator were described in section (5.2.1). A 0.15% at. wt. doped, 5mm long Brewster/Brewster cut Ti:sapphire crystal was used in this laser. This crystal was found to absorb 65% of the pump light focused down to a 150μm spot radius inside the crystal. The pump spot was maintained at this size as determined by damage considerations in Cr:LiSAF. From the considerations of equation (5.1) it is clear that the pump absorption saturation fluence of Ti:sapphire will be much higher than that of Cr:LiSAF. This together with the fact that Ti:sapphire is a much more robust medium [5] (as discussed in chapter 3), means that in practice tighter pump focusing into Ti:sapphire can be implemented with the same energy without fear of crystal damage. The result of keeping these conditions the same for both lasers, was that a similar mode matching factor of about $\eta_B \approx 0.86$ was obtained in Ti:sapphire.

The same three-plate birefringent filter[6] was used for line-narrowing and tuning. Further line-narrowing of the Ti:sapphire laser was effected with the insertion of a 200GHz and a 20GHz uncoated glass etalon. Once again the cavity dimensions were L_1=16cm for the arm containing the Ti:sapphire crystal and L_2=18cm for the arm containing the line-narrowing and tuning elements. As before this resulted in a laser mode waist radius of ω_{0max}≈130μm at each of the flat mirrors.

6.2.2 Performance

Threshold of this laser with the intracavity birefringent filter was in the region of 250μJ, which compares to a 300μJ threshold for the equivalent Cr:LiSAF laser discussed in the previous chapter. The gain factor, as given by equation (5.2), is found to be about $K' \approx 0.7$ for the Ti:sapphire laser. From cross-sections alone, this is expected to be about six-seven times larger than that for the equivalent Cr:LiSAF laser. However, the reduced coupling efficiency due to a short Ti:sapphire crystal and the wrong AR coatings on the input mirror and coupling optic, means that the efficiency factor for this Ti:sapphire laser is $\eta \approx 0.3$,

which is about one half that of the Cr:LiSAF laser. With this the respective gain factors are in agreement. The intracavity losses are expected to be roughly the same for both lasers, which means that the Ti:sapphire threshold is expected to be about one third that of the equivalent Cr:LiSAF laser, if equation (2.1.58) is used. Obviously this is not the case. This is explained by the fact that there is more parasitic loss in the Ti:sapphire laser. Also the short upper state lifetime of Ti:sapphire plays a critical role in increasing the observed threshold[7] as discussed in section (2.3.4). Solving equation (2.3.26) for this gain-switched Ti:sapphire laser indicates that the measured threshold is expected to be almost one and a half times that predicted by the usual threshold condition (i.e. equation (2.1.29)). This was discussed in detail in section (2.3.4) and also in section (5.3.2).

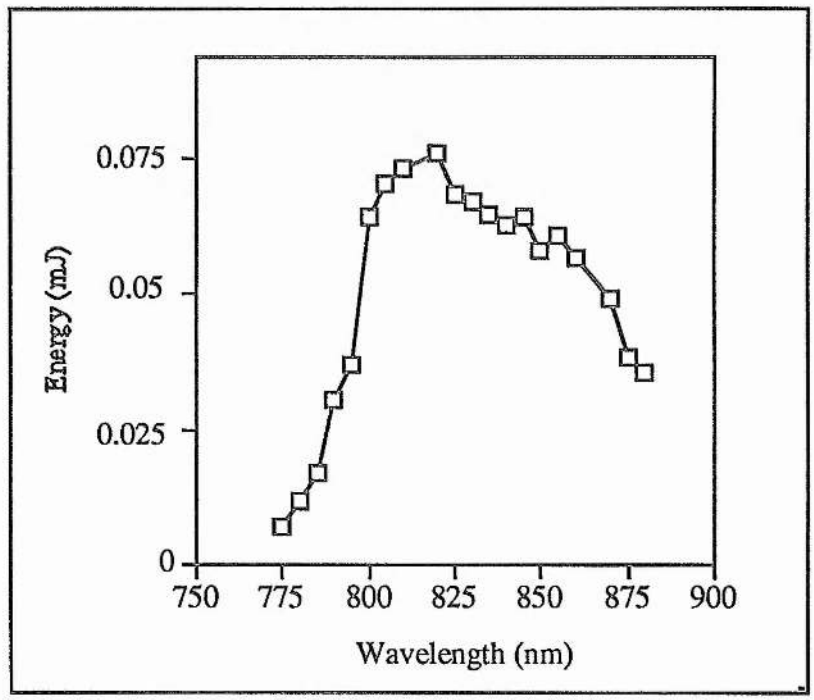

Figure 6.2 Contains the tuning range of the folded three mirror Ti:sapphire laser tuned with a 3-plate birefringent filter. The tuning range is extended compared to the equivalent Cr:LiSAF laser as depicted in Figure 5.2.

The tuning curve for the Ti:sapphire laser is presented in Figure 6.2. As with the equivalent Cr:LiSAF laser (tuning curve in Figure 5.2), the tuning range seems to be limited by the mirrors used. The Ti:sapphire tuning range is seen to extend further into the short wavelength region. This is probably due to the fact that the fluorescence peak of Ti:sapphire occurs at a shorter wavelength as recorded in table 3.1. It should be noted that, just as in the case of the

Cr:LiSAF laser, output from the Ti:sapphire laser tuned with the birefringent filter contained two frequency components at the edge of the tuning range. As discussed by Rapoport and Khattak[8] it is difficult to achieve the large number of round trips required to obtain narrow linewidth with birefringent filters in a high gain pulsed Ti:sapphire laser. Thus when the laser is tuned to the edge of its tuning range lasing can occur on the tuner sidebands.

At the peak of the tuning curve, output of up to 75μJ was obtained in pulses of 20ns duration for pump pulse energies of about 1.2mJ. There was a 10% variation in the power output of the Ti:sapphire laser. As was found in section (5.3.2) for the Cr:LiSAF laser, agreement between experiment and the theoretical model of section (2.3.1) is achieved when the losses in the Ti:sapphire laser are unexpectedly high (L≤15%). Again this is largely attributed to the fact that the Ti:sapphire crystal was incorrectly inserted at Brewster's angle. In the case of Ti:sapphire which has a refractive index of 1.76 (see table 3.1), the angle of incidence was 29.6°. Using these values in Figure 3.6 yields a value of about 5.2% reflectivity off each angled crystal surface. This compares well with a measured value of 5.4% output coupling off each surface. If the laser is remodelled with 13% output coupling and reduced parasitic losses of about 5%, then for a 1mJ pump source, output energies in excess of 250μJ are expected in pulses of less than 20ns duration.

The problem of the crystal being inserted at the wrong angle was definitely eliminated in the later investigation when the X-cavity resonator and subsequent configurations were implemented. In the X-cavity configuration, which is discussed in section (6.3), round trip parasitic losses in the absence of the birefringent filter were reduced to about 8% which corroborates the above hypothesis. The performance of the Cr:LiSAF and Ti:sapphire folded three mirror lasers is compared in table 6.1 which appears in section (6.2.4) below.

6.2.3 Line-narrowing

Line-narrowing was effected with the insertion of the 0.5mm (200GHz) and 5mm (20GHz) uncoated glass etalons available. By inserting only the 200GHz FSR and observing that a maximum of 2 etalon modes oscillated at any time, enabled a lower limit of >200GHz and an upper limit of <400GHz to be placed on the bandwidth of the laser with the birefringent tuner

as the only line-narrowing device. This is substantially reduced from the free running operational bandwidth which is of the order of 40nm, peak at 800nm. The tuning curve with the birefringent filter appears in Figure 6.2 and was discussed in the above section.

The 200GHz FSR etalon was oriented so a single etalon mode was selected. In this situation the oscillation bandwidth of the laser was reduced to 60GHz. This was further narrowed by inserting a 20GHz. This etalon was not of very high quality, i.e. the surfaces were quite scratched. It therefore introduced substantial losses into the resonator and subsequently the laser only operated at on a single etalon mode which was measured to be no greater than 15GHz in extent. These line-narrowing results are presented for comparison with the Cr:LiSAF equivalents in table 6.1, which appears in the next section.

All these measurements were made by analysing the stored CCD images of the Fabry-Perot fringe patterns along the horizontal diagonal. The images were obtained by passing the output of the laser through a Fabry-Perot interferometer of variable length as described in section (5.3.3). From table 6.1 it is seen that it was more difficult to achieve appreciable line-narrowing in Ti:sapphire. This is as a result of the much higher gain obtained in Ti:sapphire with the higher pump energies available. This results in fewer round trips per photon which reduces the efficacy of the line-narrowing elements.

6.2.4 Comparison

The performance of Ti:sapphire and Cr:LiSAF in identical three mirror folded resonators is summarised in table 6.1[9]. From the table it is evident that under gain-switched operation Ti:sapphire is the vibronic medium of choice in the presence of large intracavity losses. With its short upperstate lifetime no longer a detrimental factor, its large emission cross-section gives rise to much higher gain. This is most evident in the respective pulse durations of the two lasers. It is also apparent from the fact that it is more difficult to achieve comparable line-narrowing in Ti:sapphire.

The parasitic losses in the two systems was detrimentally high. In both cases this was caused by having the crystal inserted at the incorrect angle and as such this is avoidable. For Ti:sapphire, the losses were found to be in the region of 5% per surface. In the case of

Cr:LiSAF the smaller refractive index reduces this loss to about 1.5% per surface. Theoretical models, described in sections (5.3.2) and (6.2.2), predict superior operation for both lasers if this problem is eliminated. The residual parasitic loss in each case is then reduced to about 5% in the Ti:sapphire laser and 5.5% in the Cr:LiSAF laser. This remaining loss is expected to be similar for both systems and is attributed to the fact that the 20cm ROC fold mirror is specified to be highly reflecting for normal incidence.

	Cr:LiSAF Laser	Ti:sapphire Laser
Peak Emission X-section ($\times 10^{-20}$ cm^2)	4.8 at 840nm	35 at 780nm
Upperstate Lifetime (μs)	67	3.2
Threshold with BRF (μJ)	300	250
System Efficiency factor η (equation (2.1.53))	0.6	0.3
Calculated Gain factor K' (equation 5.2)	0.23	0.7
Estimated round trip parasitic losses	≤10%	≤15%
Output Energy (μJ)	100	75
Pulse Duration (ns)	75-100	20
Tuning Range (nm)	800-880	775-885
BRF Linewidth (GHz)	170	<400
Linewidth, BRF+ 1/2mm Etalon	10	60
Linewidth, BRF + 1/2mm + 5mm Etalons	---	15

Table 6.1: Contains a comparison of identical Cr:LiSAF and Ti:sapphire lasers under gain-switched conditions. Included are calculated values for the system efficiency factor, the gain factor and the parasitic losses which were used to model the lasers.

6.2.5 Conclusion

From the above table it is clear that the higher gain available from Ti:sapphire is important for overcoming the large intracavity losses associated with interferometric line-narrowing. For this reason it was decided that the goal of a line-narrowed, tunable, all-solid-state, pulsed laser would best be achieved with Ti:sapphire. Although Cr:LiSAF should ultimately have

better maximum efficiency due to its superior Stokes efficiency factor; 82.5% at 800nm as opposed to 65.4% at 800nm for Ti:sapphire, its higher threshold and lower gain were deemed critical in this context. It was also realised early on in this work that the low threshold of the Ti:sapphire laser was compatible with a cw-pumped high repetition rate 523nm pump laser developed in this department[10]. With this realisation, a high repetition rate, tunable, line-narrowed, pulsed laser system became the focus of attention.

6.3 Ti:sapphire X-cavity laser

6.3.1 Cavity design considerations

As the next logical step on the way to a ring laser, the resonator was converted into an x-cavity configuration. In order to have a cavity with enough space to accept the bulky intracavity birefringent filter and Faraday rotator it was necessary to redesign the resonator to be slightly longer than that obtained by merely doubling the previous cavity length. The X-cavity configuration is depicted schematically in Figure 6.3. The cavity consisted of two concave mirrors of 10cm focal length, separated by 27cm. These were placed around the 5mm long, Brewster/Brewster cut Ti:sapphire crystal. Two plane mirrors were arranged to support a standing-wave laser mode. These cavity dimensions resulted in a 100μm waist radius in the Ti:sapphire crystal. The fact that the pump beam now passed through a curved mirror which acted as a defocusing lens meant that the coupling optic had to be changed. The pump mode in the Ti:sapphire crystal was well matched by focusing the pump light with an uncoated f=75mm lens through one of the curved mirrors. This resulted in 83% transmission of the 523nm pump into the resonator, only 65% of which was absorbed by the Ti:sapphire crystal. At pumping levels of 1.3mJ, the average fluence incident on the crystal was about 3J.cm^{-2} which was insufficient to cause damage. Output coupling was obtained through one of the plane mirrors which was specified over the range 780-870nm. Three output couplers were available, namely T=2%, 3% and 5%.

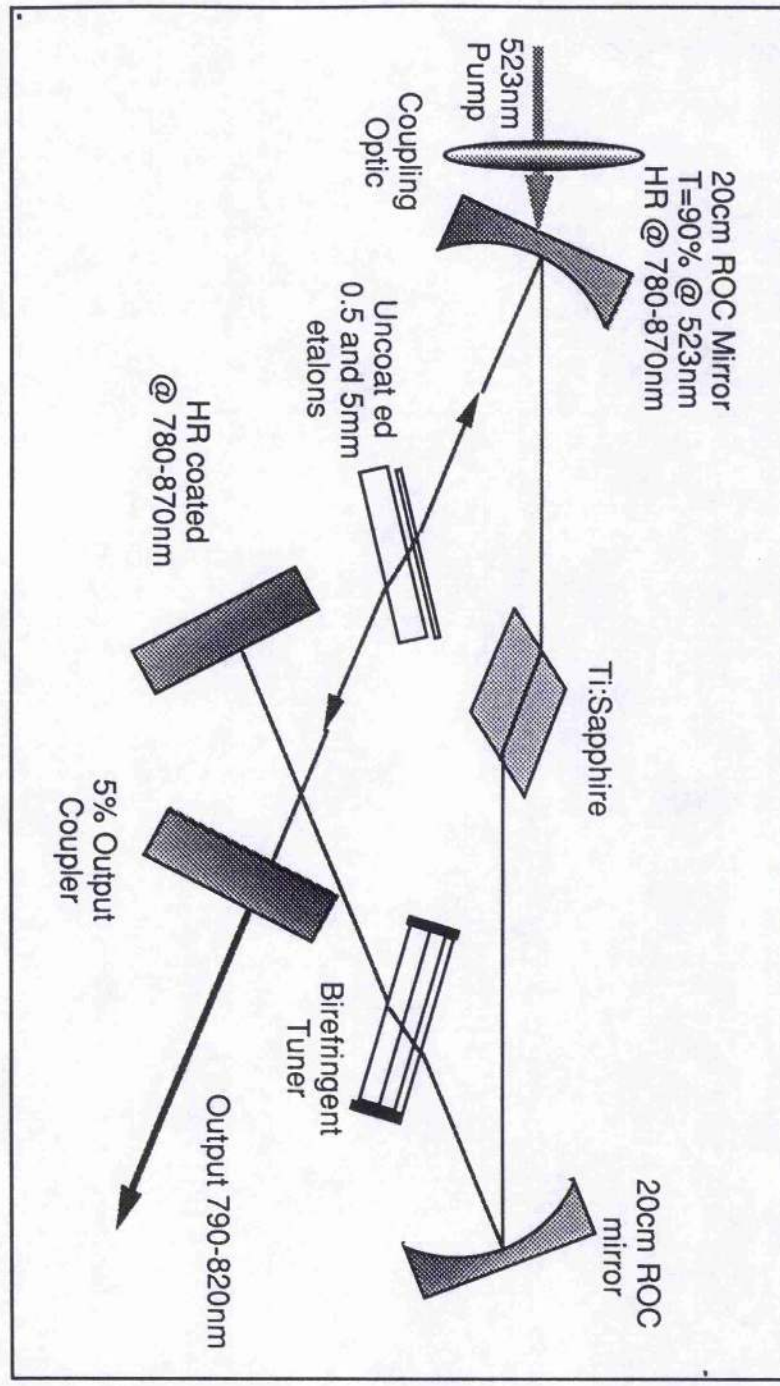

Figure 6.3 Schematic illustration of the Ti:sapphire laser in X-cavity configuration. The cavity was a slightly longer equivalent X-cavity version of the simple three mirror folded resonator used earlier. Three different output couplers (T=2%, 3% and 5%), were used.

6.3.2 Performance

The performance of this laser was measured only as far as the slope efficiencies for the various output couplers were concerned. The earlier problem of an incorrectly oriented

Ti:sapphire crystal was overcome in this investigation and so the parasitic losses were drastically reduced. This was confirmed by a substantial drop in threshold over the previously discussed 3 mirror standing-wave laser.

The pump energy thresholds were found to be 0.12mJ with the 2% output coupler, 0.14mJ with the 3% output coupler and 0.16mJ with the 5% output coupler. These compare to a threshold of the 3-mirror cavity with the 3% output coupler of 0.25mJ. This corresponds to a decrease in the intracavity losses of about 8% which suggests that the high thresholds observed in the earlier laser was in fact due to the Ti:sapphire crystal not being properly inserted at Brewster angle.

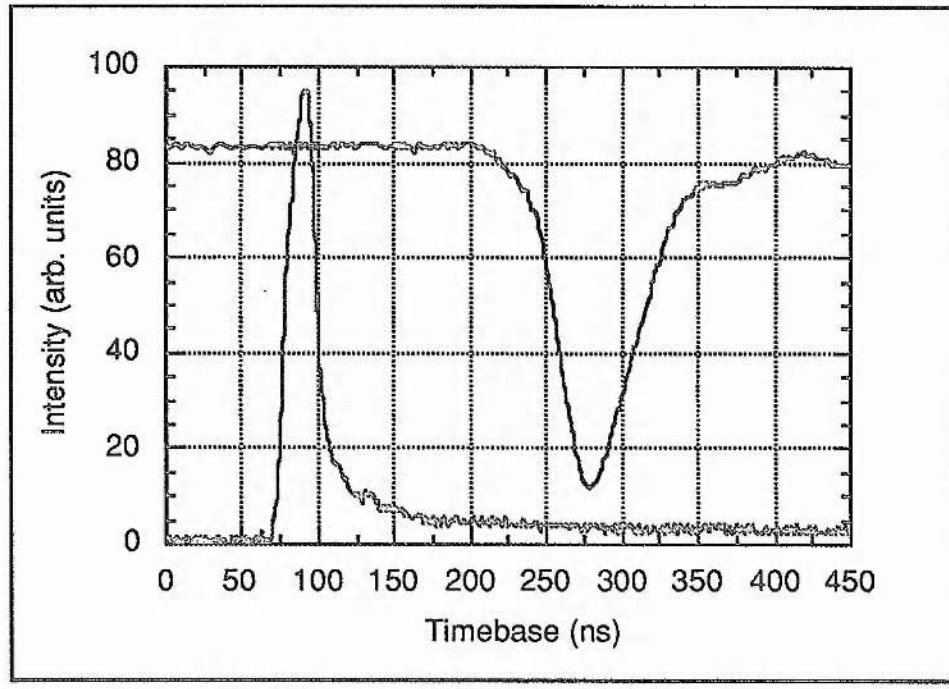

Figure 6.4 The 20ns, 523nm pump pulse (lower) is shown together with the resulting 60ns, gain-switched Ti:sapphire pulse. A pulse build-up time of approximately 150ns is apparent which is indicative of gain-switched operation.

Gain-switched operation in all these systems was confirmed by monitoring the Q-switched pumping pulse and the output from the Ti:sapphire laser simultaneously. One such observation for the X-configured laser being discussed here, is reproduced in Figure 6.4. The bottom trace is the 20ns duration pump pulse containing 0.5mJ. A build-up time of about 150ns (peak of pump pulse to 5% point of Ti:sapphire pulse), is evident before the

Ti:sapphire pulse of approximately 60ns duration appears. This confirms gain-switched operation of the laser.

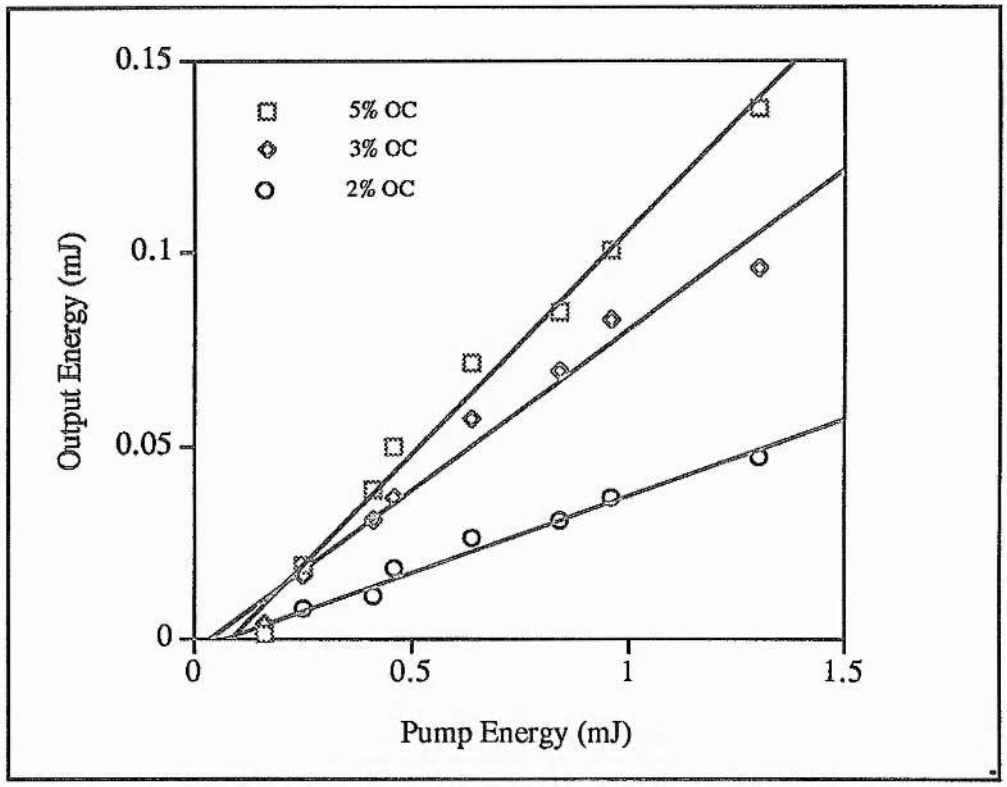

Figure 6.5 Output energy versus input energy measurements of the Ti:sapphire laser in X-cavity configuration for different output couplers. The slope efficiencies are 12%, 8.5% and 4% for the 5%, 3% and 2% output couplers respectively

Slope efficiency measurements were taken with the three available output couplers. The results are presented in Figure 6.5. From these results, the behaviour observed by Egglestone et al. [7] and described in section (2.3.4), is apparent. There is a distinct curvature of the input versus output curve near threshold. This arises from the fact that near threshold the laser takes a substantial time to build-up. In this time, because of the short upper state lifetime, the inverted population decreases appreciably by spontaneous emission. This results in a threshold increased from the usual gain equals loss criterion of equation (2.1.58). It is clear that the relationship between the output and input energies can no longer be regarded as linear and that numerical methods are required to model the process more accurately. As mentioned in the previous chapter, this precludes estimation of the parasitic losses from a simple threshold versus output coupling analysis. In all the gain-switched lasers investigated in this

work, losses were estimated by allowing the loss parameter to be a variable in both the threshold relation given by equation (2.3.26) and the energy output far from threshold as given by equation (2.3.10). The total round trip parasitic losses, determined in this fashion, were estimated to be approximately 8% for the X-cavity Ti:sapphire laser. As before, this loss was mainly attributed to the loss through the curved mirrors which were tilted away from their optimum working angle of normal incidence.

6.4 Ti:sapphire ring laser

The X-cavity configuration described above was converted into a ring resonator by rotating the two plane mirrors towards each other as depicted in Figure 6.6. The intention was to obtain unidirectional operation of this laser by inserting a Faraday rotator. This would eliminate spatial hole burning (as discussed in section 2.2.2), and in conjunction with intracavity interferometric elements enable further line-narrowing.

As indicated in Figure 6.6, it was not possible to obtain unidirectional operation of this laser with the available components. The Faraday rotator, which was designed for a cw laser[6], did not have sufficient discrimination for a system with such high gain. The backward direction experienced a net rotation of between 5° and 7° over the tuning range of this laser. This corresponds to a maximum differential loss of between 8% and 12% in the backward direction. As was seen in section (6.2.2), the Ti:sapphire is easily able to overcome parasitic losses of 15%. It therefore comes as no surprise that the laser operated in both directions as with a contrast ratio of 3:1. This was true even near threshold.

Rather than exploring this approach further, involving extensive redesign of optical elements, it was decided to pursue injection seeding of the Ti:sapphire ring laser as a much more reliable and efficient way of achieving single-frequency operation. The details of this investigation are discussed in the following section.

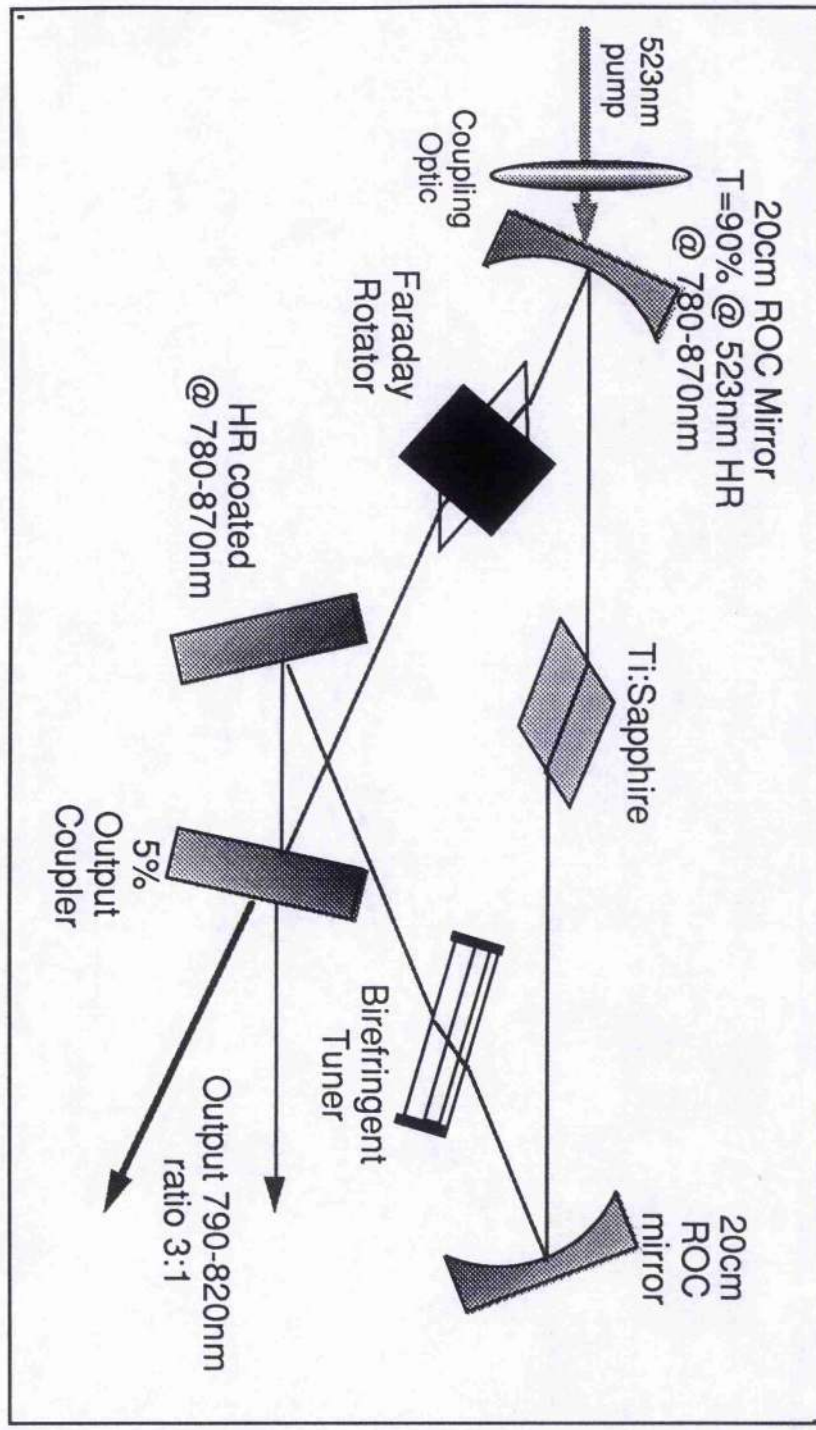

Figure 6.6 Schematic of the Ti:sapphire ring laser resonator. The 3-plate birefringent filter and the unidirectional device were inserted in an attempt to obtain single-frequency, tunable operation.

6.5 Injection seeded Ti:sapphire ring laser

6.5.1 Introduction

Successful line-narrowed, gain-switched systems are generally injection seeded to achieve single-frequency operation[11-15]. The reduced efficacy of interferometric line-narrowing techniques in the few cavity round trips available under pulsed operation[8], means that injection seeding is the method of choice for achieving line-narrowed output. The seed source has not always been all-solid-state, varying from dye laser[11] to Alexandrite lasers[8] and even line-narrowed cw Ti:sapphire lasers[12]. For compactness and reduced complexity, it is advantageous to replace such seed sources by narrow linewidth (SLM) laser diodes which are now readily available[16a]. Although alternative line-narrowing schemes like those incorporating grazing incidence gratings have been successful[17], these methods are susceptible to damage and further require high pump powers to overcome the high insertion losses of these elements, thus obviating the advantages of compact design.

Injection seeding is a well understood technique where the slave oscillator is forced to lase on the longitudinal mode closest to the injected frequency[18]. The mechanism of this technique was described in section 2.4. The presence of even very little coherent seed radiation favours those cavity modes nearest the seed frequency over any other modes which must build up from the spontaneous emission noise alone. Stable single frequency operation requires that the cavity length is continuously monitored and adjusted to keep it on resonance with the seed wavelength.

6.5.2 System layout

The basic set-up for the injection-seeded Ti:sapphire laser is illustrated in Figure 6.7. The cavity was redesigned compared to the first ring laser described in sections 6.3 and 6.4. Since bulky intracavity line-narrowing devices were no longer required, it was decided that the cavity should be reduced in length as far as possible.

The cavity dimensions of the folded three mirror resonator, namely L_1=16cm and L_2=18cm were used as the basis. At the centre of its stability range this gave a maximum beam waist in the crystal of 130μm. Using Figure 2.5 it is seen that a reduction in L_1, which implies a

reduction in the separation of the curved mirrors, will result in a reduction in the waist radius in the crystal. A mode waist radius in the crystal of 100μm required a reduction in the curved mirror separation corresponding to L_1=12cm, according to equations (2.2.29) and (2.2.24).

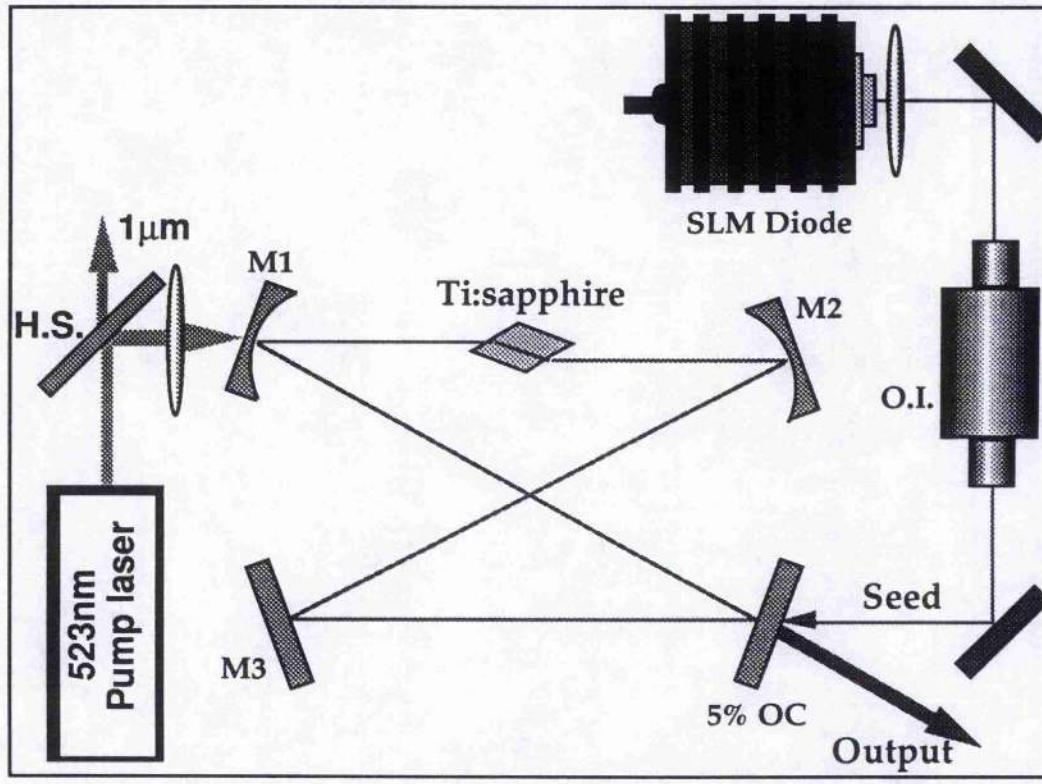

Figure 6.7: A schematic of the injection seeded Ti:sapphire ring oscillator. H.S. is a harmonic separator, M1 and M2 are 20cm ROC mirrors HR @ 780-870nm, T>90% @ 523nm. M3 is a plane mirror HR @ 780-870nm and O.I. is the optical isolator.

The resonator consisted of two concave mirrors of 10cm focal length, separated by 24cm. These were placed around the 5mm long, Brewster/Brewster cut Ti:sapphire crystal. The two plane mirrors were initially placed 16cm from the curved mirrors and arranged to support a standing-wave laser mode. When the two plane mirrors were rotated round so that the ring resonator was formed the extra path length corresponded to an additional 2cm per arm such that a 100μm laser mode radius was located in the Ti:sapphire crystal, according to the calculation described above. As was the case in the X-cavity configuration, the pump mode in the Ti:sapphire crystal was well matched by focusing the pump light with an uncoated f =75mm lens through one of the curved mirrors. Once again this resulted in about 83% transmission of the 523nm pump into the resonator, 65% of which was absorbed by the

Ti:sapphire crystal. Output coupling was obtained through one of the plane mirrors which was specified over the range 780-870nm. Three output couplers were available, namely T=2%, 3% and 5%. When the laser was not seeded, bi-directional operation resulted.

6.5.3 Unseeded performance

This redesigned ring resonator with no intracavity elements was first characterised without an injected seed. As such it exhibited bi-directional operation and therefore the effective output coupling was doubled. Slope efficiency results for this laser appear in Figure 6.8 for various output couplers. The slopes with the 2%, 3%, the 5% and both the 3% and 5% output couplers together are 6%, 12%, 17% and 18%, respectively. Care must be taken when quoting slope efficiencies as these become falsely high near threshold. The slope efficiencies quoted here are indicated in Figure 6.8. The experimental thresholds occur at higher values than indicated by the extrapolated slope line. As described in section (6.3.2), this effect is caused by the short upperstate lifetime of Ti:sapphire which appreciably reduces the population inversion, and hence the gain, during the pulse build-up time near threshold operation. With both the 5% and 3% output couplers inserted, about 200μJ was extracted in pulses of 26ns duration for a pump energy of 1.3mJ. This amounts to a conversion efficiency of over 15%. The experimental threshold was found to be roughly 0.25mJ, 0.20mJ, 0.17mJ and 0.15mJ for the laser with output coupling in descending order of transmission. The energy was extracted in pulses, typically of 25-50ns duration at the higher pumping levels.

This kind of performance was predicted to within 15% by equations (2.3.10) , (2.3.13) and (2.3.26), using the system parameters determined from the original laser described in section (6.2.2). The total parasitic losses were assumed to about 8% as in the case of the X-cavity laser (see section (6.3.2)), and the gain in each direction was assumed to add up to the double pass gain. The only significant change was the output coupling which is effectively doubled in the bi-directional ring.

This method also works for describing unidirectional operation of the seeded Ti:sapphire laser. In this case the losses, the round trip time and the gain factor are all halved compared to the X-resonator laser. Discussion of the output energy performance of the injection seeded

laser will be deferred until section 6.5 which deals with a high repetition rate version of this laser.

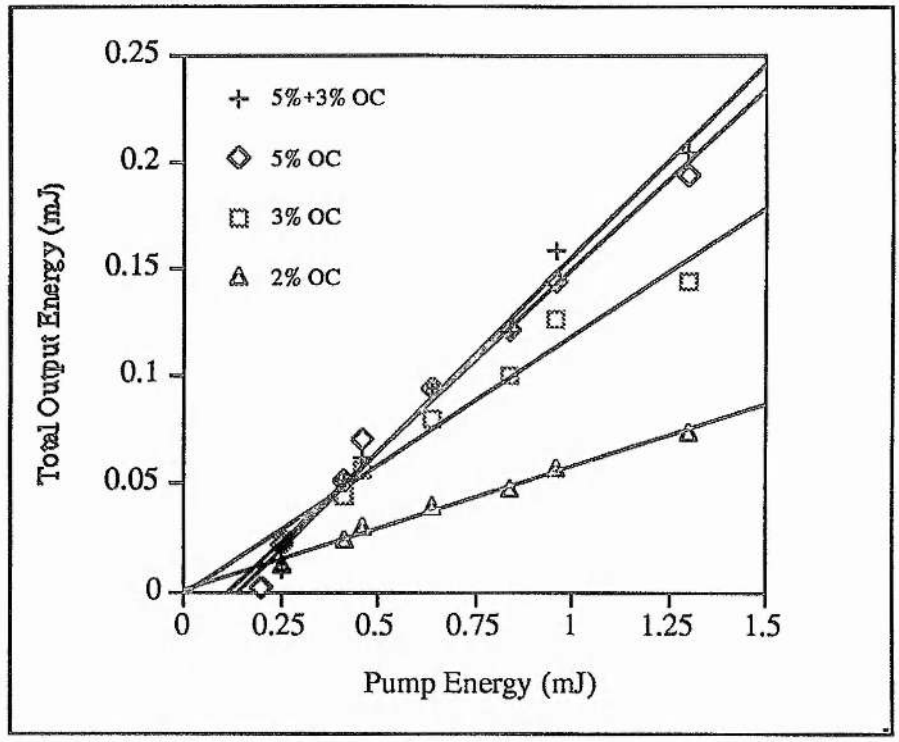

Figure 6.8 Slope efficiency measurements for bi-directional operation of the Ti:sapphire laser in ring configuration for different output couplers. The slopes are 18%, 17%, 12% and 6% for output coupling in descending order of transmission.

6.5.4 Injection-seeded operation

Frequency control of the ring laser was achieved by coupling the output from a single-mode laser diode into the basic ring resonator through the output coupler, as depicted in Figure 6.7. Feedback into the diode is eliminated by passing it through a -27dB optical isolator. The injection seed source was a SDL-5402 laser diode. This was able to deliver up to 50mW of single frequency (<15MHz) output.

The results of the injection seeding are in keeping with previous observation that a seed not resonant with a cavity mode of the laser will not force the laser to operate on only a single mode, but oscillation will build up on a few of the nearest cavity modes. Without cavity stabilisation, the passive instability associated with the various mechanical components will

result in a rapid fluctuation in and out of single-mode operation[12]. Figure 6.9 shows three traces of ring patterns obtained with a Fabry-Perot interferometer monitoring the output of the seeded ring oscillator. The free spectral range of the interferometer is 3GHz. The first trace shows the output of the single-mode diode. The second shows the case where a cavity mode is on exact resonance with the seed frequency, and single-mode oscillation is achieved. The third trace shows the seeded Ti:sapphire laser oscillating on three longitudinal modes. This behaviour was also evident in the pulse build-up time and energy of the seeded pulse. When single-mode seeding was attained, the pulse build-up time was observed to sharply decrease from 150ns to 100ns and there was a noticeable increase (10%) in the pulse energy compared to the case where a number of modes were seeded. This behaviour is depicted in Figure 6.11.

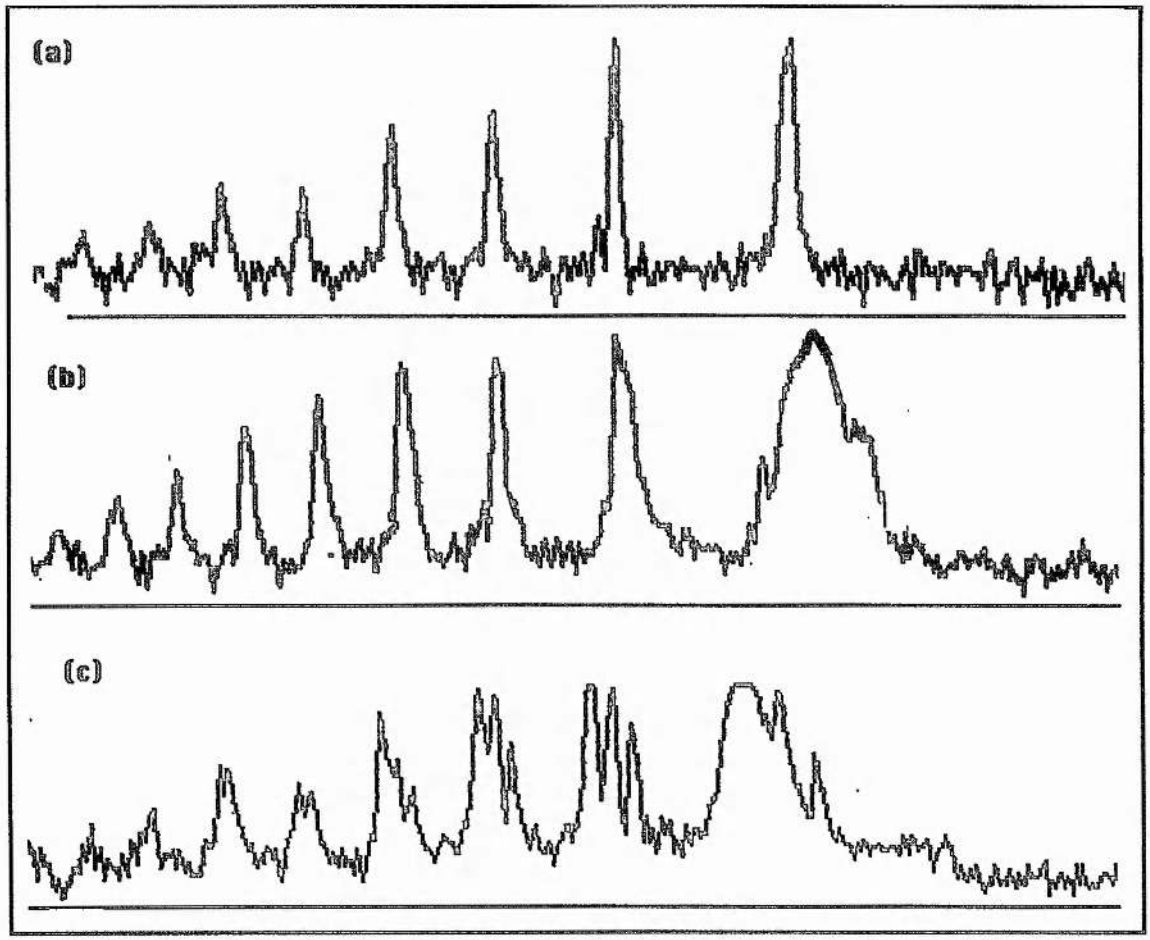

Figure 6.9: Scans through Fabry-Perot ring patterns from a 3GHz FSR interferometer. (a) is of the SLM seed diode, (b) is the SLM output of the well seeded Ti:sapphire laser and (c) is of the case when a Ti:sapphire mode was not in resonance with the seed frequency, indicating oscillation at three cavity modes.

It should be noted that all of these scans are of single shots. Without cavity stabilisation, the passive instability associated with the various mounts result in a rapid fluctuation in and out of SLM operation[12]. Other than collimating the seed diode output, no real effort was expended on minimising the seed power necessary to effectively control the output of the laser.

6.6 High repetition rate injection seeded Ti:sapphire laser

6.6.1 Introduction

Gain-switched Ti:sapphire lasers[1,7] with narrow-linewidth output[8,11-15] have been around since the introduction of Ti:sapphire in 1983[19]. Frequency-doubling of these systems into the blue has also been demonstrated[20]. However, these have all been pumped by low repetition rate flashlamp pumped systems. In the cases where flashlamp pumped systems have been replaced by diode pumped equivalents, line-narrowing has not yet been successfully effected[21]. The combination of a gain-switched, line-narrowed Ti:sapphire laser with a truly all-solid-state pump source, operating at high repetition rates (≤10kHz) is a novel tuneable laser source. As a source of narrowband, high average and peak power light it is of interest for atmospheric sensing applications such as (DIAL) lidar[22]. Knowles et al.[16] described a CVL pump Ti:sapphire (i.e. high repetition rate) which they also injection seeded. However, they encountered feedback problems and couldn't narrow the output further than about 5GHz.

With the low threshold of the laser discussed in the preceding sections (<200μJ), it was decided to construct a high repetition rate version. This was achieved by pumping the Ti:sapphire in the above ring cavity with a high repetition Q-switched, frequency-doubled Nd:YLF laser recently developed in our laboratories[10]. This laser could deliver up to 2.5W of average power at 523nm. At a minimum repetition rate of 6kHz this corresponded to pulse energies of 420μJ per pulse. At repetition rates of 6kHz the seeded Ti:sapphire laser delivered up to 70μJ in 100ns pulses when running on a single-mode, thus providing a single-frequency source of 420mW mean power. The set-up used was exactly as depicted in Figure 6.7 with the high repetition rate pump laser replacing the low repetition-rate pump laser.

6.6.2 Injection-seeded performance

Output coupling optimisation

An attempt was made to determine the optimum output coupling required for the high repetition rate Ti:sapphire laser. The usual Finlay-Clay analysis (see section 2.2.1.5) of the losses is not applicable here, since the thresholds are not simply those obtained from the intercept of the slope measurements. This has been discussed in sections (2.3.4) and (6.3.2). However, the simple model as described in section (6.5.3) could be used to estimate the optimum output coupling required by this laser. The gain factor $K' \approx 0.7$, as determined in section (6.2.2), and the losses $L \approx 8\%$, as determined for the bi-directional ring resonator in section (6.5.3), were used in this estimation. In the case of a ring laser, however, there is only single pass gain and so the gain factor is reduced by one half. The losses are assumed to be roughly one half of those in the bi-directional ring laser. Using these values and the fact that the pump laser is limited to approximately 400μJ of energy, equation (2.3.20) was used to estimate the optimised output coupling. For a range of intracavity losses, this was estimated to fall in the T=3-5% region. Based on this estimate a 5% output coupler was acquired. Figure 6.8 justifies this choice of output coupler. Although Figure 6.8 is for the bi-directional ring, the injection seeded ring operated with similar performance. The fact that the fitted slopes for the different output couplers seem to be confluent at around the 400μJ pump level suggests that a 5% output coupling is a good choice. So other than roughly knowing the losses, a critical analysis of the cavity losses is not necessary.

Seeded performance

The threshold of the injection seeded Ti:sapphire ring laser with a 5% output coupler was between 180 and 200μJ. The slope efficiency measurements for this system at different pump powers are illustrated in Figure 6.10. The results are labelled according the diode power used to pump the Nd:YLF laser. The increased efficiency with 20W of diode pump power, even though the energy per pulse is unchanged, reflects improved mode-matching of the pump and Ti:sapphire modes. The maximum slope efficiency approaches 30% with 20W of diode pump

power. This corresponds to an overall optical efficiency (i.e. diode pump power in to tuneable power out) of 2%. The slope efficiency is expected to approach the previously reported values of near 50%[14,15] by improving the system efficiency. This can be directly improved in this system with correctly AR-coated coupling optics and by changing to a longer Ti:sapphire crystal for increased absorption.

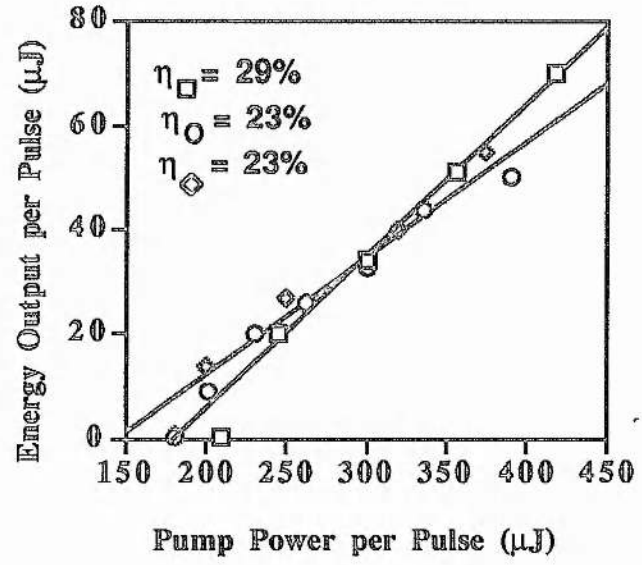

Figure 6.10: Slope efficiency measurements of the seeded high repetition-rate Ti:sapphire laser. The open square is for the 20W system. The open circle is for the 10W system and the open diamond is for the 15W system.

This performance corresponds to the production of up to 420mW of single-frequency output. The output takes the form of 70μJ of energy in 100ns pulses at a repetition rates of 6kHz. Higher repetition rates are possible but there is a trade-off between repetition rate and pulse energy of the pump laser[10]. In both the low repetition rate and high repetition rate Ti:sapphire lasers the output was observed to be of near diffraction limited TEM_{00} spatial quality, although it was slightly elliptical.

The restrictions on achieving single-mode Ti:sapphire operation are the same as before; requiring the cavity to be actively stabilised so that SLM operation can be reliably achieved. Again the minimum required amount of diode light needed for effective seeding was not determined. Maintenance of single-frequency operation required continual (manual)

adjustment of the Ti:sapphire laser cavity to hold the resonance condition. Active stabilisation of the Ti:sapphire cavity using servo-feedback electronics would overcome this limitation.

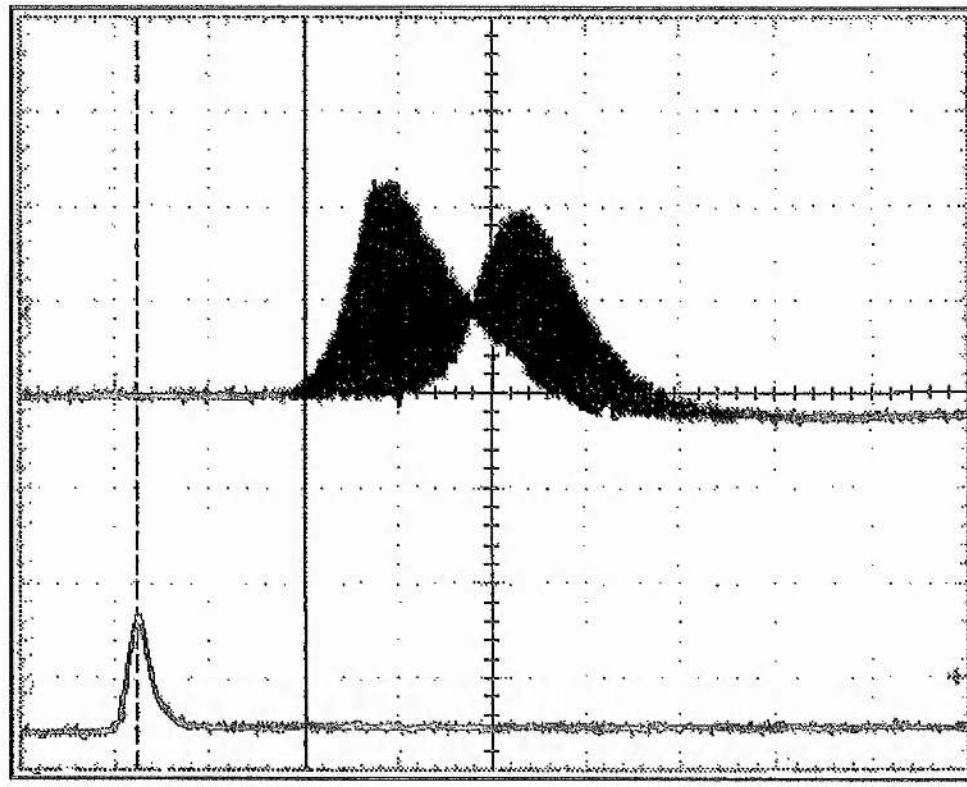

Figure 6.11: Oscilloscope traces of the pump pulse (bottom) and the resulting seeded Ti:sapphire pulses (top). When the Ti:sapphire is well seeded single-frequency operation occurs and the pulse build-up time is greatly reduced (top left-hand). The right-hand lobe is obtained when the laser is not well seeded, resulting in multimode operation which takes longer to build-up. The oscilloscope was triggered on repetitive mode and so many pulses are displayed simultaneously.

This behaviour is evident in the pulse build-up time and energy of the seeded output and is depicted in Figure 6.11. When single-mode seeding was attained, as depicted in Figure 6.8(b), the pulse build-up time was observed to sharply decrease from 150ns to 100ns (see Figure 6.11 above) and there was a noticeable increase in the pulse energy (>10%) compared to the case where a number of modes were seeded, as depicted in Figure 6.8(c).

6.7 Conclusions

The comparison of the two vibronic media Cr:LiSAF and Ti:sapphire in a folded, three mirror resonator was not ideal given the problem of having inserted the crystal at the wrong angle.

This resulted in differentially increased losses for the two lasers, which made a true comparison problematic. Useful conclusions can, however, still be derived from the results. For example through modelling the performance, the gain parameter for both these lasers has been estimated. The gain parameter is independent of the parasitic losses of a given laser. The limiting factors in these gains can be identified and optimised. The limiting factor was found to be bulk damage in Cr:LiSAF (>10Jcm^{-2}), and surface damage in Ti:sapphire (>25Jcm^{-2}). The ultimate limiting factor for any gain-switched laser is the Stokes efficiency which benefits Cr:LiSAF with its longer pump wavelength. As was mentioned in chapter 3, Cr:LiSAF experiences deleterious effects under high thermal loads which therefore limit its application to low repetition rate systems. This will be considered further in the concluding chapter.

More realistic losses, were estimated by considering the cavities employed later in the Ti:sapphire investigation when the crystal angle problem was rectified. This enabled the optimised performance to be projected. The fact that this type of analysis enabled prediction of the performance of the seeded Ti:sapphire laser to within 15% of the observed values, engenders confidence in this solution.

It is believed that the all-solid-state, high-repetition gain-switched, single-frequency Ti:sapphire laser by injection seeding which has been developed, represents a novel source. The injection seeded laser has been shown to deliver up to 420mW of single-mode laser output at repetition rates of 6kHz. The beauty of this line-narrowing system compared to conventional lossy techniques is that no intracavity elements are required and so higher efficiencies care observed.

The cavity length has recently been reduced, by as much as a half of that reported here, by optimising it for pumping with the 400μJ available from the high repetition rate pump laser. This results in increased peak power. Although this source has not yet demonstrated reliable single-mode operation, this should be achievable by active stabilisation of the Ti:sapphire cavity. There are plans to pursue this feature in the future. A reliable single-frequency source with high peak and average powers, would be of great interest for remote sensing and spectroscopic applications. Although seeding by diodes reduces the tuneability of the system,

this should not restrict its suitability for sensing applications since SLM diodes are now available which cover most of the Ti:sapphire tuning range.

References

[1] P.F. Moulton, "Spectroscopic and laser characteristics of Ti:Al_2O_3", *J. of Opt. Soc. Am. B*, B3, (1986), p125

[2] S.A. Payne, L.L. Chase, H.W. Newkirk, L.K. Smith and W.F. Krupke, "$LiCAF_6:Cr^{3+}$: A Promising New Solid-State Laser Material", *IEEE J. of Quant. Elect.*, QE-24, (1988), p2243

[3] S.A. Payne, L.L. Chase, L.K. Smith, W.L. Kway and H.W. Newkirk, "Laser performance of $LiSrAlF_6:Cr^{3+}$, *J. Appl. Phys.*, 66, (1989), p1051

[4] M. Stadler, M. Bass and B.H.T. Chai, "Thermal quenching of fluorescence in chromium-doped fluoride laser crystals", *J. Opt. Soc. Am.*, B9, (1992), p2271

[5] B.W. Woods, S.A. Payne, J.E. Marion, R.S. Hughes and L.E. Davis, "Thermomechanical and thermo-optical properties of the $LiCAF_6:Cr^{3+}$ laser material", *J. Opt. Soc. Am.*, B8, (1991), p970

[6] Schwarz Electro Optic Inc., Research Division, 45 Winthrop Street, Concord MA 01742, U.S.A, "TITAN cw Ti:sapphire laser".

[7] J.M. Egglestone, L.G. DeShazer and K.W. Kangas, "Characteristics and kinetics of laser-pumped Ti:sapphire oscillators", *IEEE . of Quant. Elec.*, QE-24, (1988), p1009

[8] W.R. Rapoport and C.P. Khattak, "Titanium sapphire laser characteristics", *Appl. Opt.*, 27, (1988), p2677

[9] G.R. Morrison, C.F. Rae, M. Ebrahimzadeh and M.H. Dunn, "Comparison of all-solid-state gain-switched Cr:LiSAF and Ti:sapphire lasers", Quantum Electronics Conference (QE-12), Southampton UK, September 1995, Technical Digest, P3-1

[10] C.P. Rahlff, B.D. Sinclair and W. Sibbett, M.H. Dunn, Conference on Lasers and Electo-optics (CLEO 94), Anaheim USA, May 1994, Technical Digest Series 8 , p308

[11] P. Brockman, C.H. Bair, J.C. Barnes, R.V. Hess and E.V. Browell, "Pulsed injection control of a titanium-doped sapphire laser", *Opt. Lett.*, 11, (1986), p712

[12] G.A. Rines and P.F. Moulton, "Performance of gain-switched Ti:Al_2O_3 unstable-resonator lasers", *Opt. Lett.*, **15**, (1990), p434

[13] T.D. Raymond and A.V. Smith, "Injection-seeded titanium-doped-sapphire laser", *Opt. Lett.*, **16**, (1991), p33

[14] C.E. Hamilton, "Single-frequency, injection-seeded Ti:sapphire ring laser with high temporal precision", *Opt. Lett.*, **17**, (1992), p728

[15] J.C. Barnes, N.P. Barnes, L.G. Wang and W. Edwards, "Injection Seeding II: Ti:Al_2O_3 Experiments", *IEEE J. of Quant. Elec.*, **QE-29**, (1993), p2685

[16a] Environmental Optical Sensors, Inc., Boulder CO 80301-3376, U.S.A., *Laser Focus World*, **March**, (1996), p21

[16] M.R.H. Knowles and C.E. Webb, "Cavity configurations for copper vapour laser pumped titanium sapphire lasers", *Opt. Comm.*, **89**, (1992), p493

[17] K.W. Kangas, D.D. Lowethal and C.H. Miller, "Single-longitudinal-mode, tunable, pulsed Ti:sapphire oscillator", *Opt. Lett.*, **14**, (1989), p21

[18] Y.K. Park, G. Giulina and R.L. Byer, "Single axial mode operation of a Q-switched Nd:YAG oscillator by injection seeding", *IEEE J. of Quant. Elec.*, **QE-20**, (1984), p117

[19] P.F. Moulton "New developments in solid state lasers", *Laser Focus* , **May**, (1983), p83

[20] A.J.W. Brown, C.H. Fisher and K.W. Kangas, "Efficient, high-energy, narrow-band, blue-light source", *Opt. Lett.*, **18**, (1993), p1177

[21] T.R. Steele, D.C. Gerstenberger, A. Drobshoff and R.W. Wallace, "Broadly tunable high-power operation of an all-solid-state titanium-doped sapphire laser system", *Opt. Lett.*, **16**, (1991), p399

[22] S. Ismail and E.V. Browell, "Airborne and spaceborne lidar measurements of water vapor profiles: a sensitivity analysis", *Appl. Opt.*, **28**, (1989), p3603

CHAPTER 7

DISCUSSION AND CONCLUSIONS

A promising all-solid-state, high repetition rate, single-frequency, gain-switched Ti:sapphire laser has been developed. While reliable single-frequency operation has not yet been demonstrated, this does not seem unattainable. A simple electronic feedback loop would enable the laser resonator to be locked onto the seed diode frequency which would thus result in reliable single-frequency operation. This is the future aim of this work.

To that end, a monolithic block has been designed which incorporates the ring laser and the injection seeding apparatus onto a single base. The laser resonator was redesigned to be optimised for pumping with the high repetition rate frequency doubled 1μm Nd:YLF laser. Smaller mode sizes meant that the cavity round trip length could be reduced by as much as one half the length of the resonator presented here. This is expected to result in more energetic pulses of roughly one half the duration reported in this work. Improved coupling optics and more efficient pump absorption (new crystal) have been implemented. Improved energy extraction is expected and a 600mW single frequency laser source, at 6kHz repetition rates, is now envisaged.

The monolithic base should provide the mechanical rigidity to minimise vibration and thus help to achieve an actively stabilised laser by servo-locking the resonator to the injected signal. Further optimisation of the design could be achieved by minimising the amount of seed signal required to achieve reliable single-frequency operation. This could be achieved by taking more care to mode match the seed diode beam to the laser resonator mode in the Ti:sapphire crystal.

The one restrictive aspect of this system is the apparent lack of tuneability. This is not, however, imagined to be a serious problem. There is a range of single frequency diodes available which cover the tuning range of Ti:sapphire. These are also tuneable over a few tens of degrees. More useful, perhaps, are the recently commercialised widely tuneable single-

frequency diode lasers. These offer extended tuneability over the Ti:sapphire range. They do not compete with the Ti:sapphire laser as it offers much higher peak and average powers.

The initial aim to produce an all-solid-state nano-second pulse duration, tunable, line-narrowed laser has therefore been achieved, albeit in a form different from that initially envisaged. At the outset a diode pumped Cr:LiSAF version was envisaged. However, practical constraints and continual evaluation of alternative options led to the diode-pumped solid-state laser, pumped Ti:sapphire substitute.

However, a tuneable, gain-switched Cr:LiSAF was developed and its performance was compared with that of an equivalent Ti:sapphire laser. While this Cr:LiSAF, Ti:sapphire gain-switched comparison is interesting it is not the main focus of this work. At first, the extent of Ti:sapphire's overwhelming superiority under gain-switching was not really apparent. The idea was merely for an equivalent Ti:sapphire laser to be built which would enable the Cr:LiSAF laser performance to be compared with this much more well-established vibronic laser medium. It is true to say that the comparison of these two materials in near identical configurations was not rigorously completed. The promise of superior Ti:sapphire performance meant that development of the initial system was rapidly pursued. Each of the subsequent steps in the development of the final Ti:sapphire laser was well characterised.

The superiority of Ti:sapphire as a laser medium, in this configuration, was again apparent when uni-directional operation of the ring laser was attempted. The stimulated emission cross-section is so high (for vibronic media) that it was not possible to enforce uni-directional operation with a Faraday rotator even when such lossy intracavity elements as a birefringent tuner and uncoated glass etalons were inserted. It is of course understood that the Faraday rotator used in this work was designed for a cw laser and not for a high-gain, pulsed laser. There is no reason that a suitable Faraday rotator could not be constructed which would impart sufficient discrimination so as to enforce uni-directional in the gain-switched Ti:sapphire laser.

This option was not pursued because the much more efficient method of achieving single-frequency operation, namely injection seeding, had become a much more practical and

appealing option. The appeal of this method is the lack of lossy intracavity elements which result in increased system efficiency.

Despite abandoning the Cr:LiSAF option, a positive conclusion can been reached regarding the feasibility of a diode-pumped, Q-switched vibronic laser offering tuneable, narrow linewidth laser output. Red laser diode technology, together with fibre-coupling technology is now sufficiently far advanced that a diode-pumped, Q-switched, injection seeded Cr:LiSAF is a distinct possibility. An injection seeded Cr:LiSAF would be ideal if the associated thermal problems could be overcome. The more recently developed material Cr:LiSGAF appears to be a suitable solution. While it has similar spectroscopic and thermo-mechanical properties to those of Cr:LiSAF, it appears not to suffer from the thermal effects which plague Cr:LiSAF at high pump powers.

Such a laser will still require intracavity Q-switching, which would result in reduced efficiency compared to a gain-switched system. This is crucial in the light of the small stimulated emission cross-section of these materials. The resonator modes are, however, small enough to enable efficient implementation of acousto-optic Q-switching. This offers a promising option for a compact line-narrowed device tuneable over a wide range. Tuneability would again be restricted by seed diodes.

Finally, it is worth mentioning the novel, frequency-doubled, Q-switched 1.321μm Nd:YLF laser which was developed as a pump source for the Cr:LiSAF laser. This represents an interesting source because it has not been widely developed. This was apparent in the inferior performance of the intracavity optical coatings compared to those for the equivalent 1μm lasers. The source is also of interested since the 1.3μm output falls in the fibre optics communications window. The frequency-doubling represented the first time that a type II phase-matching geometry in LBO was used in a laser system at this wavelength.